

ABSTRACT

Title of Document: MAGNETOELASTIC COUPLING IN NiMnGa
 FERROMAGNETIC SHAPE MEMORY ALLOY

Peng Zhao, Doctor of Philosophy, 2006

Directed By: Professor, Manfred Wuttig, Department of Materials
 Science and Engineering

NiMnGa alloys have attracted extensive attention because their ferromagnetic characteristic provides an additional degree of freedom to control both the shape memory effect and the multi-stage phase transformations in this Heusler system. Technically, along with the large magnetic-field-induced strains, NiMnGa alloys exhibit giant magnetocaloric effect due to their magnetic entropy changes associated with the coupled magnetostructural transitions. Fundamentally, a sequence of phase transformations, manifesting itself by a rich variety of physical anomalies on cooling to the martensitic transformation (MT) temperature T_M , has been established. However, in comparison to the intensive studies of structural transformations, the magnetic properties of NiMnGa premartensite were hardly touched. The purpose of this research is to i) investigate the temperature dependence of the magnetic driving force of martensitic NiMnGa, which is a critical factor to determine the actuation temperature window of this material; and ii) understand the magnetoelastic coupling

enhanced precursor effects, especially the unique magnetic behavior of NiMnGa premartensite.

The singular point detection technique has been applied to determine the magnetic anisotropy constant K_1 of a martensitic $\text{Ni}_{49.0}\text{Mn}_{23.5}\text{Ga}_{27.5}$ (wt%) crystal. As expected, K_1 increases with decreasing temperatures below T_M of 276 K, following a magnetization power law $K_1(T)/K_1(0)=(M_s(T)/M_s(0))^3$. However, the force required to initiate twin boundary motion increases exponentially with decreasing temperature. The combination of both temperature dependences leads to a very restricted temperature window for magnetic actuation using this alloy.

The premartensitic transformation has been established by means of neutron powder diffraction and measurements of elastic constants of C_{44} and C' . The premartensitic phase has been verified by the stiffening of C_{44} prior to the MT. The slope change of C' at T_C positively confirms that the precursor phenomena are enhanced by the magnetoelastic coupling. Magnetic $\text{Ni}_{49.0}\text{Mn}_{23.5}\text{Ga}_{27.5}$ premartensite is characterized by the coexistence of a finite dc magnetic susceptibility and a vanishing magnetocrystalline anisotropy, distinguishing bcc NiMnGa from the typical magnetic soft materials. This property arises from the competition between the exchange forces of the host lattice and the strong local crystal fields stemming from the tweed.

MAGNETOELASTIC COUPLING IN NiMnGa FERROMAGNETIC SHAPE
MEMORY ALLOY

By

Peng Zhao

Dissertation submitted to the Faculty of the Graduate School of the
University of Maryland, College Park, in partial fulfillment
of the requirements for the degree of
Doctor of Philosophy
2006

Advisory Committee:
Professor M. Wuttig, Advisor and Chair
Professor A. Flatau
Professor A. L. Roytburd
Associate Professor I. Takeuchi
Adjunct Professor J. Cullen

© Copyright by
Peng Zhao
2006

Acknowledgements

“Thank the flame for its light, but do not forget the lampholder standing in the shade with constancy of patience.” Tagore.

I wish to express my appreciation and respect to all those who have helped me in various ways and made my journey unique to this point. It is no doubt that good company on the road is the shortest cut.

First, I am deeply indebted to my supervisor, Dr. Manfred Wuttig, for offering not only the enlightening guidance and unreserved support during the course of this journey, but the understanding of the essence of “a good science” as well. To me, Manfred is more than an academic advisor, but a mentor of my life. Feeling his great strength in mind, I never found age a factor in making us difficult to understand. And Manfred always finds ways to be outgoing and kind. I still remember the smile on his face when he stated that “I want to be a nice boss.”

I am thankful to Dr. James Cullen, who shared with me the riches of his knowledge on magnetism and magnetic materials. I have been fortunate to have invaluable discussions with a person of his caliber.

I sincerely thank Dr. Ichiro Takeuchi for mentoring me when Manfred was away. Thank you for the opportunity to interact with many people in your research group and to gain access to the facilities in Center for Superconductivity Research.

I want to thank the other two dissertation committee members of mine, Dr. Alison Flatau and Dr. Alexander L. Roytburd, for teaching me how to think in a global way through your lectures in different classes, conferences and workshops.

Thanks for all the committee members for your invaluable time to serve on my defense and constructive comments on my thesis.

My special thanks to Dr. Oscar Moze from Universita di Modena e Reggio Emilia and Mr. Qingzhen Huang, Dr. Hye Jung Kang, Dr. Jeffrey W. Lynn from the NIST Center for Neutron Research for introducing me to the field of neutron research and assisting me the crystallographic data analysis and lattice dynamic analysis.

I have furthermore to thank Dr. Scott Mathews and Dr. John A. Judge from the Catholic University of America for helping us renovate the magneto-sputtering system and teaching me the lab discipline.

I would also like to thank all my group members for providing a stimulating and fun place where to learn and grow. These include Dr. Corneliu Craciunescu, Dr. Yoichi Kishi, Dr. Jun Cui, Dr. Kiyotaka Mori, Dr. Liyang Dai, Dr. Minghui Yu, Dr. Makoto Murakami, Dr. Olugbenga Olawale Famodu, together with Manas Dash, Nobuko Coda, Sadia Rafique, Shigehiro Fujino, Lei Zheng, Shenqiang Ren and Jason Hattrick-Simpers.

Finally I would like to thank my extended family. Thanks my lovely wife, Xin Jing, for arm and arm walking with me throughout the journey. Although in her eyes, the only one of her children who never grows up and moves away will be her husband. Thank you for being understanding and caring. Thanks my parents and my in-laws in China for their love, support and sacrifice. Without their encouragement and trust, I will never reach this point. Especially, I want to give my deepest gratitude to my grandparents in heaven. I always had the feeling that they were staying by my side,

watching over me and guiding me whenever it was difficult. Now I wish they look down on me with pride.

Table of Contents

Acknowledgements.....	ii
Table of Contents.....	v
List of Figures.....	viii
List of Tables.....	xii
1 The Martensitic Transformation.....	1
1.1 Introduction.....	1
1.2 Diffusional Transformations.....	1
1.3 Diffusionless Transformations.....	3
1.4 Martensitic Transformations.....	6
1.4.1 Diffusionless Characteristics.....	6
1.4.2 Martensite Crystallography.....	8
1.5 Shape Memory Alloys.....	16
1.5.1 Shape Memory Effects.....	16
1.5.2 Thermoelastic Shape Memory Alloys.....	21
1.5.3 Ferromagnetic Shape Memory Alloys.....	23
1.6 Premartensitic Transformations.....	25
1.6.1 Charge Density Waves.....	27
1.6.2 Martensite Nucleation.....	30
1.6.3 Precursor Effects.....	32
2 Phase Transformations in NiMnGa FSMAs.....	35

2.1 Martensitic NiMnGa	35
2.1.1 Introduction.....	35
2.1.2 Crystal Structures of Martensitic NiMnGa	36
2.1.3 Magnetic-field-induced Strains in NiMnGa	40
2.2 Premartensitic NiMnGa	45
2.2.1 Multi-stage Transformations in NiMnGa	45
2.2.2 Precursor Phenomena in NiMnGa	50
2.3 Research Motivations.....	58
3 Actuation Field in Martensitic $\text{Ni}_{49,0}\text{Mn}_{23,5}\text{Ga}_{27,5}$ Alloy	62
3.1 Introduction.....	62
3.2 Experimental Procedures	63
3.2.1 Sample Information	63
3.2.2 Experimental Methods	63
3.2.3 SPD technique.....	65
3.3 Results and Discussions.....	66
4 Elastic and Magnetic Properties of $\text{Ni}_{49,0}\text{Mn}_{23,5}\text{Ga}_{27,5}$ Premartensite	83
4.1 Introduction.....	83
4.2 Experimental Procedures	84
4.2.1 Sample Information	84
4.2.2 High Resolution Neutron Powder Diffraction	84
4.2.3 Elastic Measurement.....	84
4.2.4 Magnetic Measurement.....	86
4.3 Results and Discussions.....	90

4.3.1 Crystal Structures.....	90
4.3.2 Elastic Anomalies	93
4.3.3 Landau Models.....	101
4.3.4 Magnetic Properties	105
4.4 Summary	113
5 Conclusions.....	115
Bibliography	118

List of Figures

1.1 (a) The relevant part of the Fe-C phase diagram. (b) Schematic representation of formation of pearlite from austenite.	4
1.2 Classification scheme for displacive/diffusionless phase transformations.	7
1.3 (a) and (b) illustrate how a martensite plate remains (macroscopically) coherent with the surrounding austenite and even the surface it intersects; (c) Schematic representation of the invariant-plane strain shape deformation characteristic of a MT.	10
1.4 Bain correspondence for the $\alpha \rightarrow \alpha'$ transformation.	12
1.5 (a) The effect of the Bain strain on austenite, which when undeformed is represented as a sphere of diameter $wx=yz$ in 3D. The strain transforms it to an ellipsoid of revolution. (b) The invariant-line strain obtained by combining the Bain strain with a rigid body rotation through an angle θ	13
1.6 (a) As shown for twinning (left) and slip (right), the same magnitude of the homogeneous shear, as given by the angle γ , can be accomplished by either. (b) Twins in martensite may be self-accommodating and reduce energy by having alternate regions of the austenite undergo the Bain strain along different axes.	15
1.7 Typical martensitic microstructures of low (left) and high (right) carbon steels. ...	17
1.8 Coil-spring example illustrating the differences between the one-way and two-way shape memories.	19

1.9 Electrical resistance changes during cooling and heating Fe-Ni and Au-Cd alloys, illustrating the hysteresis of the martensitic transformation on cooling, and the reverse transformation on heating	20
1.10 (a) mechanism of SME, (b) Optical micrograph of self-accomodation of the R-phase (Ti-48.2Ni-1.5Fe (at%) alloy).....	22
1.11 Magnetic-field-induced twin boundary motion.	26
1.12 Peierls instability.....	29
2.1 L ₂₁ austenite structure.....	37
2.2 Projection on (001) of the ideal L ₂₁ Heusler alloy structure	39
2.3 The structure of 10M martensite and the lattice parameters obtained from the electron diffraction patterns for Ni ₅₀ Al ₁₉ Mn ₃₁ alloy.....	41
2.4 (a) Scheme of the L ₁₀ cell. (b) Lattice correspondence between the “cubic” axes and those for the L ₁₀ cell.	42
2.5 (a) Characteristic phase transformation temperatures as a function of the electron concentration for NiMnGa alloys, (b) Paradigm of the multistage displacive structural transformations with modulated precursor phases of NiMnGa alloys with e/a < 7.6.....	47
2.6 (a) A symmetric (001) zone-axis electron diffraction patterns of the high-temperature parent L ₂₁ structure obtained at 293 K. (b) The CTEM microstructural image produced under two-beam bright-field condition; (c) The HRTEM microstructural image showing local atomic displacements and domain structure.....	49

2.7 Elastic modulus vs. temperature curves recorded during cooling for NiMnGa alloys of group I, II, and III, respectively.	52
2.8 Measured acoustic-phonon dispersion curves for the parent L2 ₁ phase of Ni ₂ MnGa.	54
2.9 (a) Temperature dependence of the phonon anomaly in the ($\zeta, \zeta, 0$) TA ₂ branch in the parent and the premartensitic phases of Ni ₂ MnGa. (b) $(h\omega)^2$ vs T/T _M for the ($\zeta, \zeta, 0$) TA ₂ mode for Ni ₂ MnGa and Ni _{62.5} Al _{37.5} in the point where the dispersion curve is a minimum.	56
3.1 Illustrating the SPD method to estimate the anisotropy field in materials.	67
3.2 Temperature dependence of magnetization of single crystal Ni _{49.0} Mn _{23.5} Ga _{27.5} by field cooling and heating under 1 kOe.	68
3.3 Magnetization curves measured close to T _M . It demonstrates the occurrence of FSM effects with the large hysteresis observed at corresponding temperatures.	70
3.4 Magnetization curves measured at 250 K, 150 K and 5K, characterized by the multiple slope changes with changing field.	72
3.5 First derivative of magnetization as a function of H at corresponding temperatures. Inset fig. shows the field dependence of second derivative of magnetization at corresponding temperatures.	76
3.6 Temperature dependence of saturation magnetization and magnetic anisotropy constant K ₁ of martensitic Ni _{49.0} Mn _{23.5} Ga _{27.5}	78
3.7 Dependence of normalized K ₁ /M _s ⁿ for n=2, 3 and 4.	79
3.8 Mechanism of martensitic variant redistribution under magnetic field.	81
4.1 Lay-out of BT-1 high-resolution neutron powder diffractometer.	85

4.2 Experimental setup of the ultrasonic continuous-wave method.	88
4.3 Experimental setup of the cantilever oscillation method.	89
4.4 Neutron powder diffraction patterns of $\text{Ni}_{49.0}\text{Mn}_{23.5}\text{Ga}_{27.5}$ at 413 K (parent phase), 313 K (premartensitic phase) and 227 K (martensitic phase), respectively.	91
4.5 (200) neutron peak broadening measured at 301 K for NiMnGa cubic structure. ..	94
4.6 (422) neutron peak broadening measured at 301 K for NiMnGa cubic structure. ..	95
4.7 temperature dependence of C_{44}	97
4.8 Calculated ε_{me}/σ as a function of temperature.	98
4.9 Evolution of the low frequency C' and internal friction (IF) as a function of temperature (with cooling and subsequent heating).	100
4.10 Temperature dependence of magnetization of $\text{Ni}_{49.0}\text{Mn}_{23.5}\text{Ga}_{27.5}$ under 100 Oe magnetic field.	106
4.11 Temperature dependence of the magnetization of $\text{Ni}_{49.0}\text{Mn}_{23.5}\text{Ga}_{27.5}$ under various fields.	107
4.12 Initial magnetization curves at various temperatures. Magnetic field direction parallel to the cubic [001] direction.	109
4.13 Magnetization curves along [001], [110] and [111] directions in $\text{Ni}_{49.0}\text{Mn}_{23.5}\text{Ga}_{27.5}$ at 300 K.	110
4.14 Temperature dependence of magnetic anisotropy constant K_1 and K_2 in bcc solids of $\text{Ni}_{49.0}\text{Mn}_{23.5}\text{Ga}_{27.5}$	112
4.15 Model of compensated zero magnetic anisotropy.	114

List of Tables

1.1 Difference between the diffusional and diffusionless transformations.....	5
2.1 Single-crystal samples of martensitic NiMnGa with different crystal structures at RT.....	44
2.2 Comparison of precursor effects observed in ferromagnetic NiMnGa alloys and non-magnetic NiAl alloys.....	59
3.1 sample information.	64
3.2 Difference of magnetic-field-induced strains between FSMA and magnetostrictive materials	82
4.1 Elastic wave modes for C^* and C'	87

Chapter 1

The Martensitic Transformation

1.1 Introduction

The word, martensite, named after a gifted German microscopist Adolf Martens, was originally used to describe the differently oriented banded regions in hard steels in 1890.¹ Since then, the realization that the microstructure is as important as composition in determining a material's properties has expanded the studies of martensitic transformations (MTs) from the formation of the mysterious hardening constituent in quenched iron to a broad class of solid-state phase transformations occurring in metals, ceramics,^{2,3} polymers^{4,5} and semiconductors.^{6,7} The great technological importance of the MT is not restricted to bulk materials but also to thin-film heterostructures of electronic devices^{8,9} as well.

The objective of this chapter is to discuss the MT and its characteristics, the shape memory effect, the premartensitic phenomena, and finally, the role of magnetic fields in driving the MTs in ferromagnetic shape memory alloys (FSMAs).

Simply speaking, the study of phase transformations concerns those mechanisms by which a system attempts to reach an equilibrium state and how long it takes. The diffusion of atoms is obviously one of the most fundamental processes to control the kinetics of most transformations. Therefore, the diffusional transformations in solids are worth to be mentioned briefly in the beginning.

1.2 Diffusional Transformations

Diffusional transformations take place by thermally activated atomic movements leading to atomic diffusion in solids either via vacancies or migrating interstitially. The underlying reason why diffusion occurs is always to produce a decrease of the Gibbs free energy of the transforming solids. Well-known examples of diffusion transformations include precipitation and eutectoid transformations, which involve the formation of phases with a different composition from the matrix. Therefore long-range diffusion is required. It would take us too far afield to discuss all the details of diffusion-controlled transformations. Rather, in this section, we will illustrate diffusional transformations by reference to the eutectoid transformations of Fe-C-austenite into ferrite.¹⁰

As shown in Fig. 1.1(a), when austenite containing about 0.8 wt% C is cooled slowly below the A_1 temperature, it becomes simultaneously supersaturated with respect to ferrite and cementite and a eutectoid transformation results, i.e. γ (0.77% C) \rightarrow α (0.22% C) + Fe_3C (6.20% C), where carbon diffuses from ferrite to cementite. Assuming that the first stage of this phase transformation is the nucleation of cementite on an austenite grain boundary, the austenite surrounding this nucleus will become depleted of carbon. This effect will increase the driving force for the precipitation of ferrite, resulting in the formation of a ferrite nucleus adjacent to the cementite nucleus. This process can be repeated causing the colony to spread sideways along the grain boundary. After nucleation of both phases, pearlite grows into the austenite grain without having an orientation relationship. The carbon rejected from the growing ferrite diffuses through the austenite to in front of the cementite, effectively giving rise to two interpenetrating single crystals. The resultant

microstructure comprises lamellae, or sheets, of cementite embedded in ferrite as shown in Fig 1.1(b).

1.3 Diffusionless Transformations

In contrast to transformations which involve the diffusion of atoms, i.e. reconstructive transformations, diffusionless transformations occur by a coordinated motion of atoms. In diffusionless transformations, bonds between neighbors are not broken and re-formed; there is no diffusion and atoms maintain their relationships with their neighbors. They are also called displacive transformations because there is some homogeneous strain that transforms one lattice into the other, with atoms moving in a cooperative fashion. A simple example is a transformation of a square lattice into a rectangular lattice by means of compression along one axis and expansion along the other. Diffusionless transformations show their “military” character by a large scale coordinated motion of an entire lattice, proceeding in lock-step from one configuration to another. On the contrary, in the diffusional transformation, the atoms wander in search of a locally favorable environment, which renders the transformation random. The differences between the diffusional and diffusionless transformations are listed in table 1.1.

Based on the nature of the coordinated atomic displacements, displacive transformations can be subdivided into two different groups: lattice-distortive transformations and shuffle transformations and a general displacive transformation can involve a combination of displacement of both above types. The lattice-distortive transformations can be further subdivided according to the relative magnitudes of the dilatational and deviatoric (shear) strain components of the lattice deformation. A

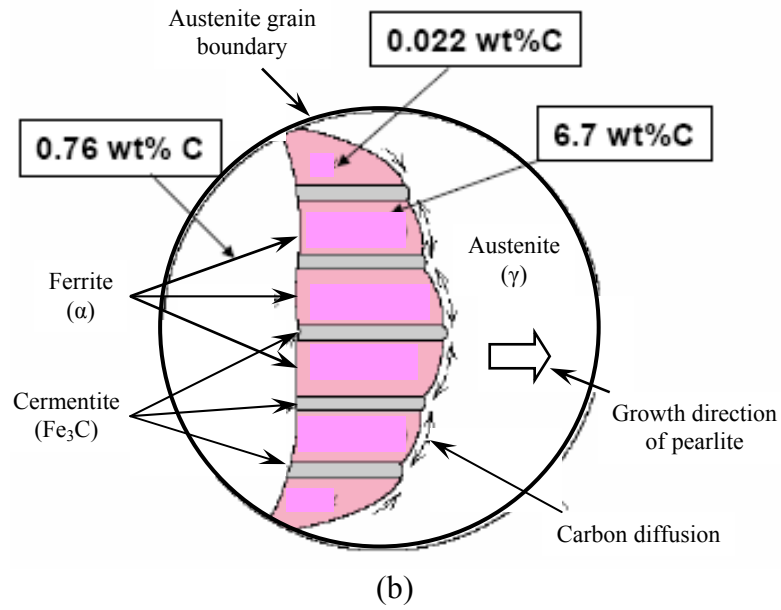
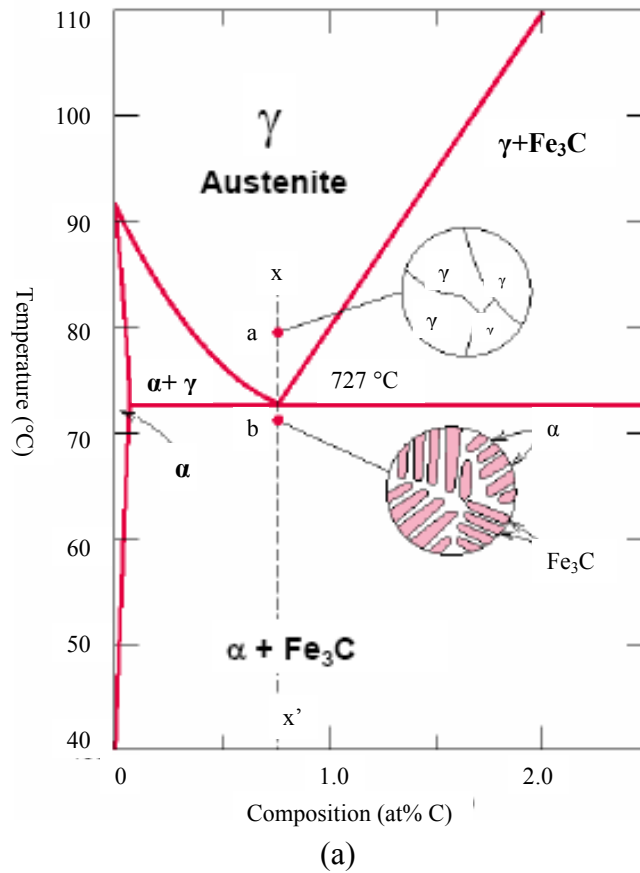


Fig. 1.1 (a) The relevant part of the Fe-C phase diagram. (b) Schematic representation of formation of pearlite from austenite.

Diffusional transformation	Diffusionless transformation
Uncoordinated movement of individual atoms (civilian transformation)	Controlled coordinated movement of individual atoms (military transformation)
Atoms change nearest neighbors as diffusion occurs	Atoms do not change nearest neighbors
Reconstructive transformation	Displacive transformation
Interface not necessarily coherent	Coherence at interface preserved
Relatively slow	Fast
Little strain energy	Large strain energy

Table 1.1 Difference between the diffusional and diffusionless transformations.

classification scheme for diffusionless displacive transformations is depicted in Fig. 1.2.¹¹ The lattice-distortive deformation results in a homogeneous strain converting one Bravais lattice to another, thus primarily contributes to the elastic strain energy. The shuffle deformation produces no net strain within the unit cell, manifesting itself mainly in the form of interfacial energy. This essential difference, in turn, leads to different kinetics and morphological changes in displacive transformations.

1.4 Martensitic Transformations

1.4.1 Diffusionless Characteristics

Martensitic transformation (MT) is a subset of the displacive transformations. Precisely, it is defined as shear-dominant, lattice-distortive, diffusionless transformation.¹² It is this class of solid-state transformation and its characteristics that constitute the focus of this thesis.

Nowadays, MT is a term extensively used in metal physics to describe any diffusionless transformation in which from start to completion of the transformation, each individual atomic movement is less than one interatomic spacing. Its technological importance was first realized through the determination of the microstructure of hardened steel in the late 19th century. A general introduction of the history of martensite can be found in reference [1]. It was a great period of change in civilization when steel replaced bronze, yet, it was entirely unknown what gave steel its valuable properties. Empirically, a myriad of minor additions to pure iron, together with more mysterious treatments, evolved to strengthen the “new” metal, and a consistent method was slowly achieved to produce a harder variety by carburizing and quenching iron. If the steel is quenched rapidly enough from the austenite phase,

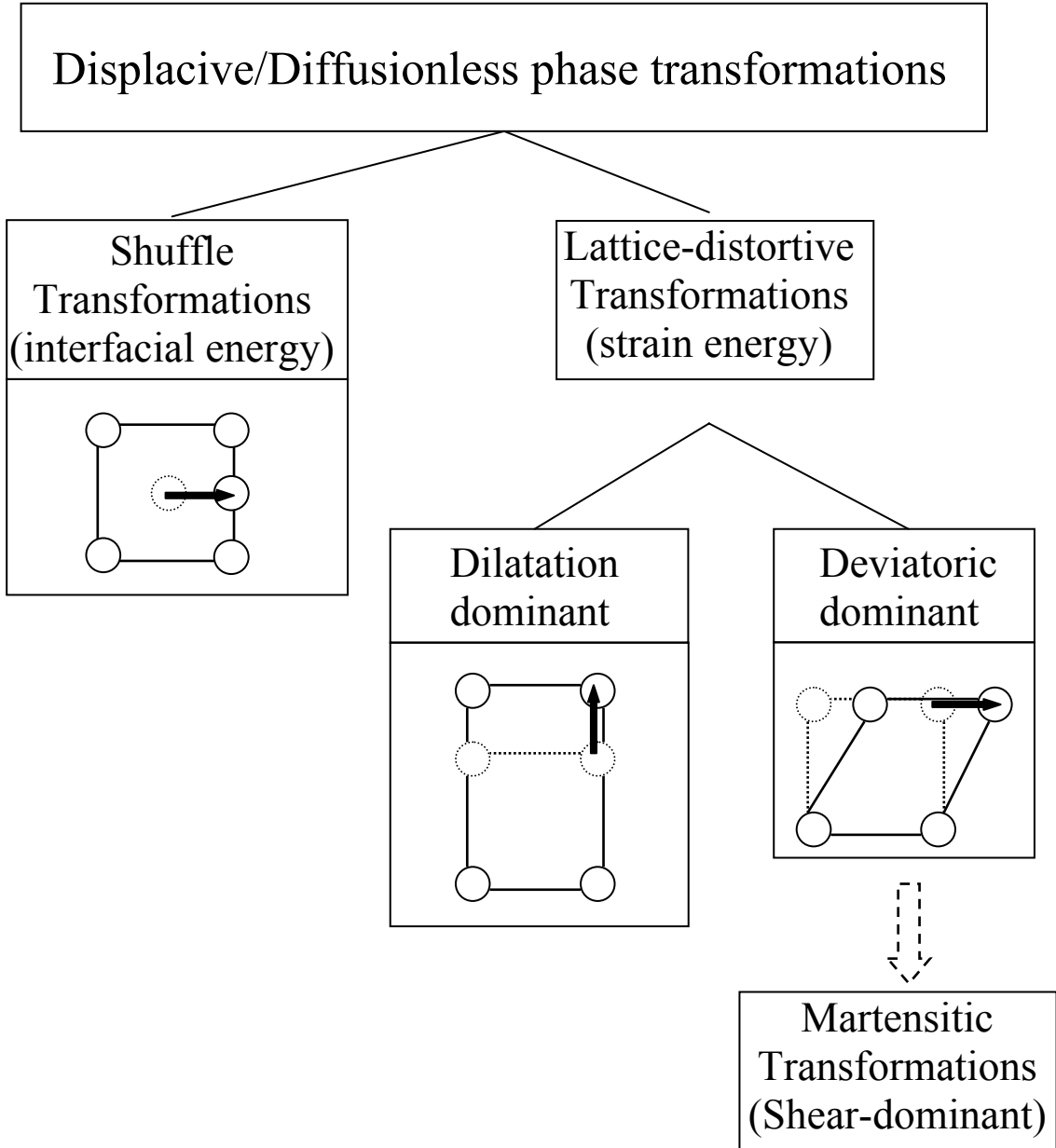


Fig. 1.2 Classification scheme for displacive/diffusionless phase transformations

there is insufficient time for the eutectoid diffusion-controlled decomposition transformation (which is described in the previous section) to occur, and the steel transforms to martensite, which is simply a supersaturated solid solution of carbon in α -Fe ($\gamma \rightarrow \alpha'$).¹³ Therefore, the average chemical composition of martensite is identical to that of the parent austenite.

It has been shown that a fully grown plate spanning a whole grain may form within $\sim 10^{-7}$ s. As plates are formed, they immediately grow to their full size with a speed of sound.¹⁴ The rapid nucleation and growth of martensite give rise to an athermal character of the MT. In the vast majority of cases, the extent of reaction is found to be virtually independent of time.¹⁵

$$1 - V_{\alpha'} = \exp[\beta - (M_s - T)] \quad \text{where } \beta \approx -0.011 \quad (1.1)$$

$V_{\alpha'}$ is the fraction of martensite and T is a temperature below M_s , the temperature martensitic transformation starts. This is called Koistinen and Marburger equation. It should be noted that time does not enter in this relation, so that the fraction of martensite depends only on the undercooling below the martensite-start temperature. In hardened steels, the martensitic phase is not a kinetically equilibrium state and can not be found in the Fe-C phase diagram.

Martensite is also known to be formed at very low temperatures, where diffusion, even through interstitial atoms, is not conceivable to occur. The totality of above observations demonstrates convincingly that martensitic transformations are diffusionless.

1.4.2 Martensite Crystallography

Since the formation of martensite cannot rely on assistance by thermal activation, there must exist a high level of continuity across the interface, which should be coherent or semi-coherent. Observations have shown that the transformed regions appear relatively coherent with the surrounding austenite. This means that intersection of the lenses with the surface of the specimen does not result in any discontinuity. Therefore, lines on a polished surface are displaced, as illustrated in Fig. 1.3, but remain continuous after the transformation. In fact, the naive picture of a perfectly coherent interface should give way to a picture of semi-coherent interface in which an array of parallel dislocations is the price paid for accommodating the lattice mismatch between the austenite matrix and the martensite nucleus.¹⁶

Assuming that it is a twinning shear occurring parallel to the habit (twinning) plane plus a simple uniaxial tensile dilation perpendicular to the habit plane, as shown in Fig. 1.3, the habit plane, which is common to both the austenite and martensite, is observed to be macroscopically undistorted, i.e. all directions and angular separations in the plane are unchanged during transformation. Hence, the shape deformation accompanying a MT can be characterized by the invariant plane strain (IPS), by which the positions or magnitude of vectors lying in the habit plane will not be changed. In an IPS, the strain experienced by any point in the lattice has a common direction and its magnitude is proportional to its distance from a fixed plane which is not distorted by the strain.

To illustrate the martensite crystallography, Bain proposed a lattice distortion with the minimum of atomic movement and the minimum of strain in the parent lattice, demonstrating how the bct lattice could be obtained from the fcc structure in

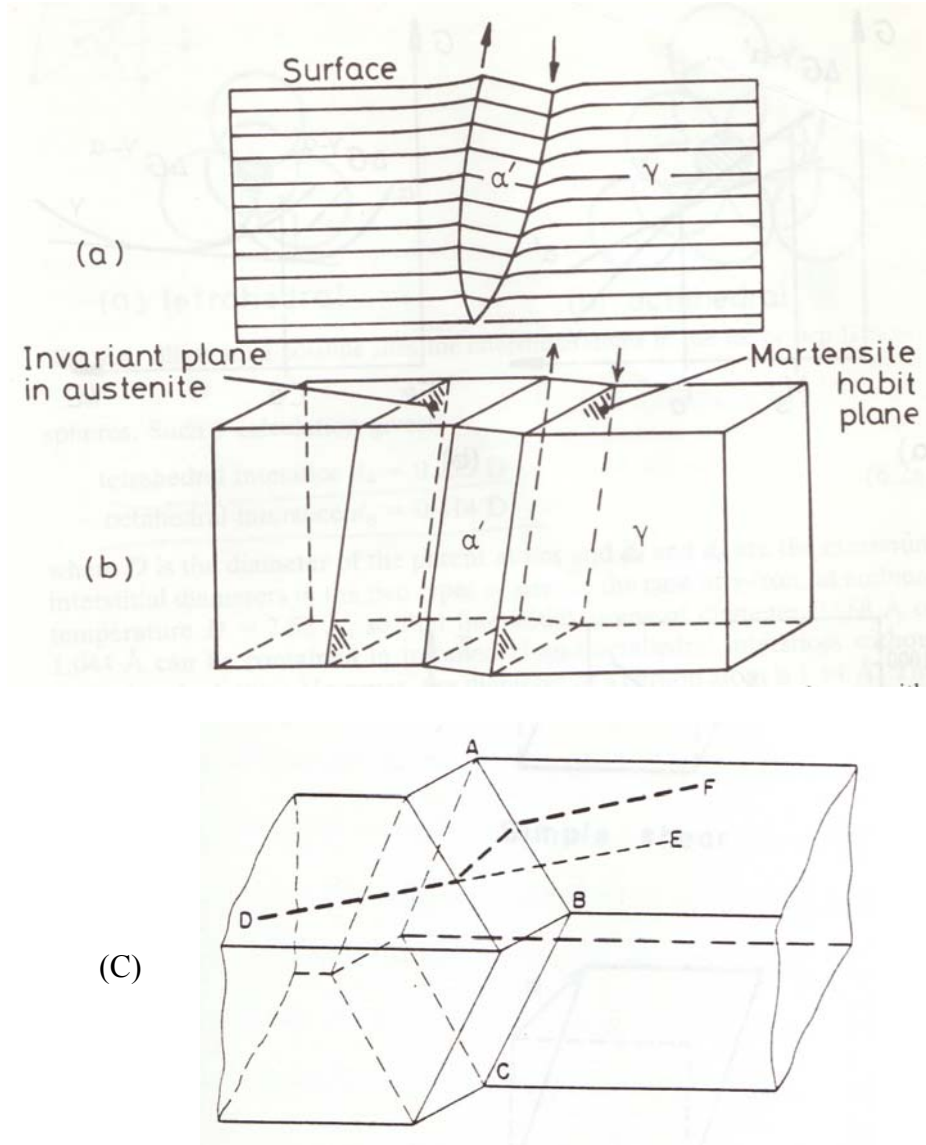


Fig. 1.3 (a) and (b) illustrate how a martensite plate remains (macroscopically) coherent with the surrounding austenite and even the surface it intersects; (c) Schematic representation of the invariant-plane strain shape deformation characteristic of a MT. The initial straight scratch DE is displaced to the position DF when the martensite plane ABC is formed. The plane ABC is invariant (undistorted and unrotated as a result of the MT).¹⁷

1924.¹⁸ Using the convention of x, y, z and x', y', z' representing the original and final axes of the fcc and bcc unit cell as plotted in Fig. 1.4, an elongated unit cell of the bcc structure can be drawn within two fcc cells. Transformation to a bcc unit cell is achieved by a 20% compression along the z axis and a 12% uniform expansion along the x and y axes. Examination of Fig. 1.4 shows that the Bain deformation results in the following correspondence of crystal planes and directions between the parent and the product phase:

$$(111)_\gamma // (011)_\alpha, \quad [001]_\gamma // [001]_\alpha, \quad [1\bar{1}0]_\gamma // [100]_\alpha, \quad [110]_\gamma // [010]_\alpha,$$

But in fact, the experimentally observed orientation relationships are irrational. The relative directions can vary between $\langle \bar{1}01 \rangle_\gamma // \langle 1\bar{1}1 \rangle_\alpha$ (the Kurdjumov-Sachs relation) and $\langle 1\bar{1}0 \rangle_\gamma // \langle 101 \rangle_\alpha$ (the Nishiyama-Wasserman relation) and these two orientations differ by $\sim 5^\circ$ about $[111]_\gamma$. We will deal with this inconsistency later.

In Fig. 1.5, the austenite (fcc) is represented as a sphere which, as a result of the Bain distortion, is deformed into an ellipsoid of revolution which represents the martensite (bcc). The expression of the ellipsoid is given by:

$$\frac{x'^2}{1.12^2} + \frac{y'^2}{1.12^2} + \frac{z'^2}{0.80^2} = 1 \quad (1.2)$$

There are no lines in the $(010)_\gamma$ plane which are undistorted. The lines, wx and yz , are undistorted in their magnitudes but rotate to the new positions $w'x'$ and $y'z'$. These directions constitute the initial and final cones of the unextended lengths. Any vector lying inside these cones is reduced in length by Bain deformation and any vector lying outside these cones is extended. The combined effect of the Bain strain and the rigid body rotation (with an angle θ) is the reason why the observed irrational orientation relationship differs from that implied by the Bain strain. However, in

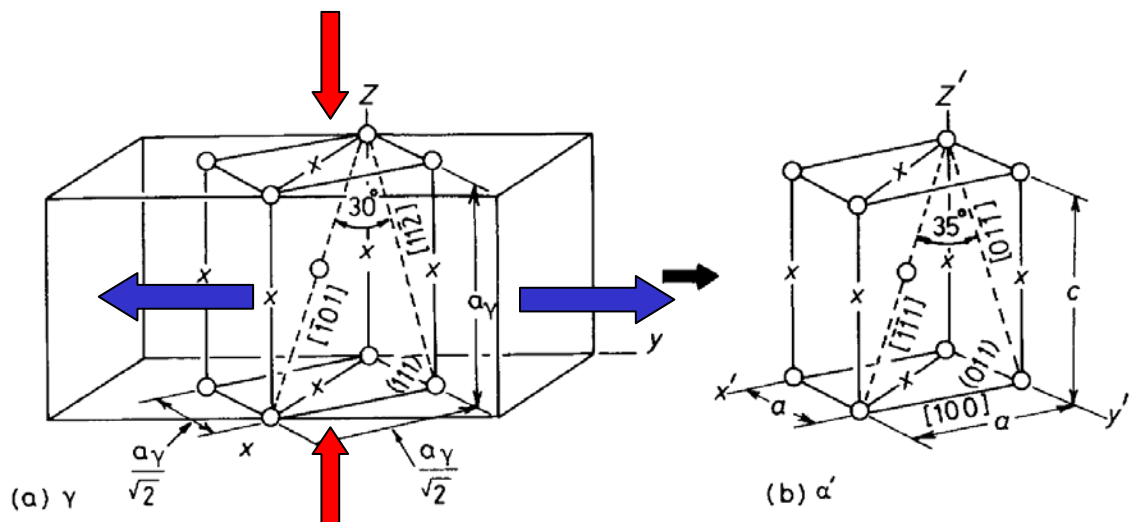


Fig. 1.4 Bain correspondence for the $\alpha \rightarrow \alpha'$ transformation. Possible interstitial sites for carbon are shown by crosses. To obtain α' the γ unit cell is contracted about 20% on the C axis and expanded about 12% on the a axes.

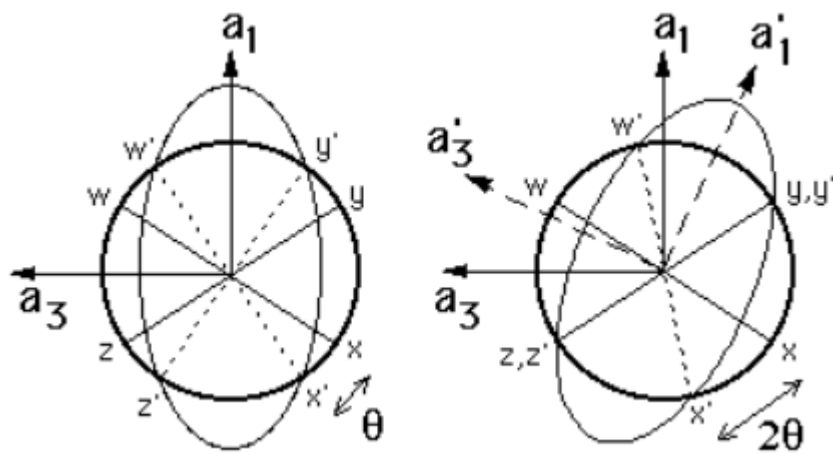
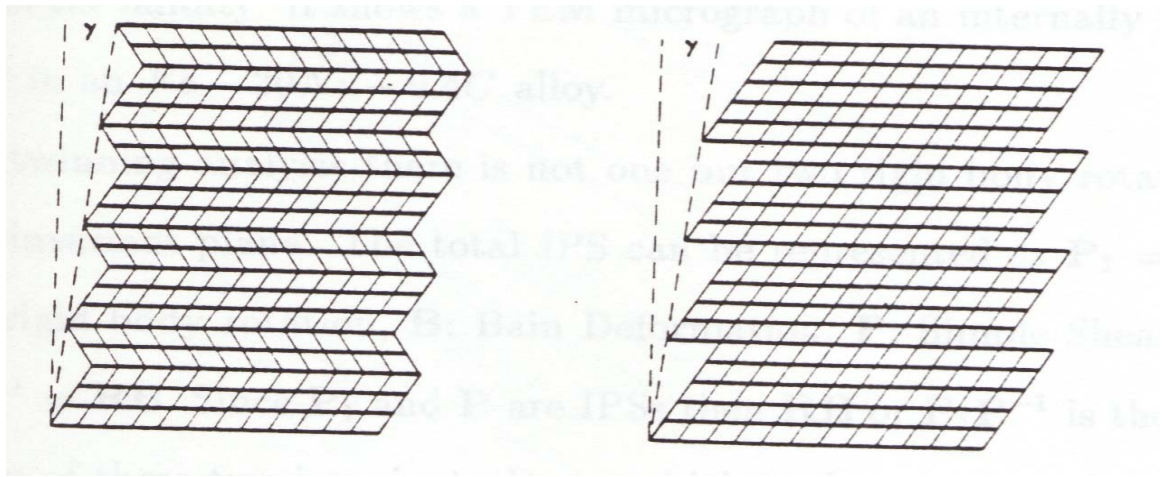


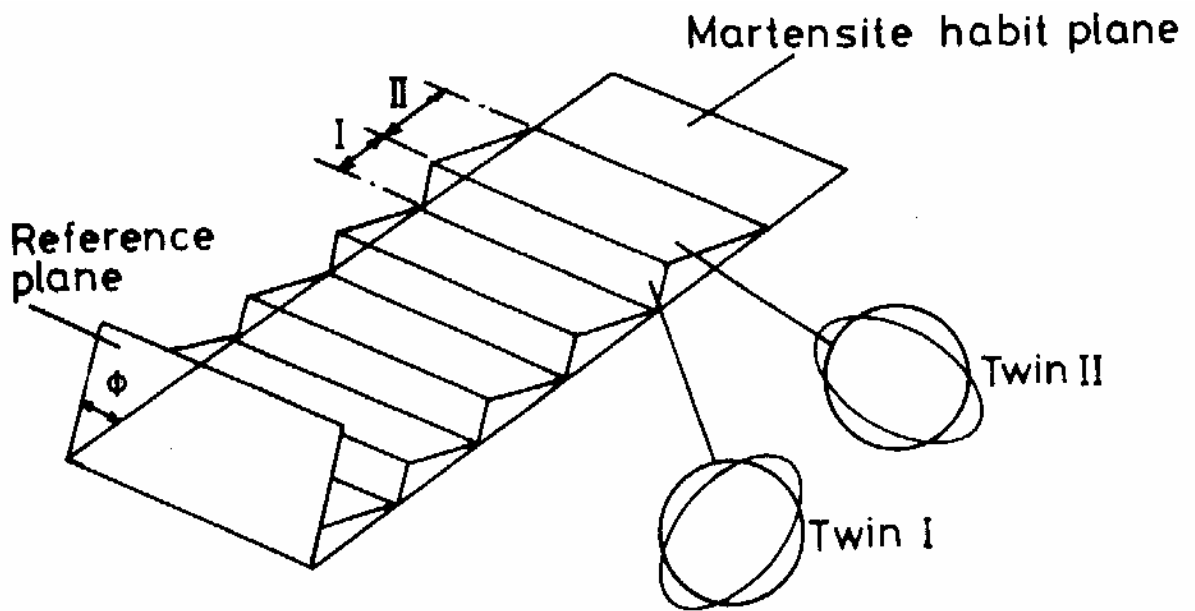
Fig. 1.5 (a) The effect of the Bain strain on austenite, which when undeformed is represented as a sphere of diameter $wx=yz$ in 3D. The strain transforms it to an ellipsoid of revolution. (b) The invariant-line strain obtained by combining the Bain strain with a rigid body rotation through an angle θ .

order to find an invariant plane in the fcc structure due to transformation, it requires that the vector oa_2 (perpendicular to the paper) must also be undistorted.¹⁹ Now, it is clear that the Bain deformation does not fulfill the requirements to bring about a transformation with an invariant plane. Instead, the total transformation strain can be envisioned as the sum of a total of three strains: Bain, lattice-invariant distortion and a rigid body rotation and these three components are not necessary to occur in a step-lock fashion.

From the above discussion, it can be seen that the key to the crystallographic theory of martensitic transformations is to postulate an additional distortion which reduces the extension of oa_2 to zero. A direct consequence of this lattice invariant distortion is the manifestation of a martensite substructure in the form of slip or twins, as illustrated in Fig.1.6 (a). These are called the lattice invariant shear, since neither process changes the structure of the martensite. In the case of slip, the martensite is a single crystal, though internally slipped. In the case of twinning, the lattice deformation along adjacent regions of the martensite occurs along crystallographic equivalent directions. The distortion is such that the adjacent regions fit together along a twinning plane in the martensite. The features of twinned martensite plates are shown in Fig. 1.6 (b). The two adjacent contraction axes were originally 90° from each other. A vector lying in the interface which experiences contraction in region A would undergo expansion in region B. The end result is an overall averaged cancelled out vector with local expansions and contractions. The resulting zig-zag interface cancels the long range interfacial strain. Note that the relative twin thicknesses



(a)



(b)

Fig. 1.6 (a) As shown for twinning (left) and slip (right), the same magnitude of the homogeneous shear, as given by the angle γ , can be accomplished by either. (b) Twins in martensite may be self-accommodating and reduce energy by having alternate regions of the austenite undergo the Bain strain along different axes.

depend on the value of γ . And by also adjusting the width of the individual twins, the habit plane of the plate can even be made to adapt to any desired orientation.

1.5 Shape Memory Alloys

In Fe-C martensites, the attendant volume changes and large shear deformations are accommodated by plastic deformation. Hence, these transformations are irreversible. As such, the martensitic transformation is hysteretic, meaning that the forward and the reverse transformations start at different temperatures, which are typically a few hundred degrees in hard steel. Having been formed by a shear, martensite is generally characterized by an acicular microstructure, as shown in Fig. 1.7. The lenticular shape of some of the dark martensite portions recognizable in the right-hand part of the figure reduces the shear stresses created by the transformation. This shear stress is large, as predicted by the Bain model, indicating that the ideal c/a ratio equals $\sqrt{2}$ of the fcc and bcc structural transformation. This is comparable to the observed c/a ratio of Fe-C martensite, being of the order of 1.1 or less.²⁰

Shape memory alloys (SMAs) undergo a reversible martensitic transformation with relatively small temperature hysteresis. Reversibility can be assured in two ways. First, the transformation can be second order, and second, it can be of first order if the lattice constants of the parent and product structures permit the martensite to grow in the austenite without creating long-range stress fields or excess interfacial energy. SMAs thus form a subgroup of all alloys undergoing a martensitic transformation. These materials have potential technical applications and their martensitic transformations have been extensively studied in the past few decades.

1.5.1 Shape Memory Effect

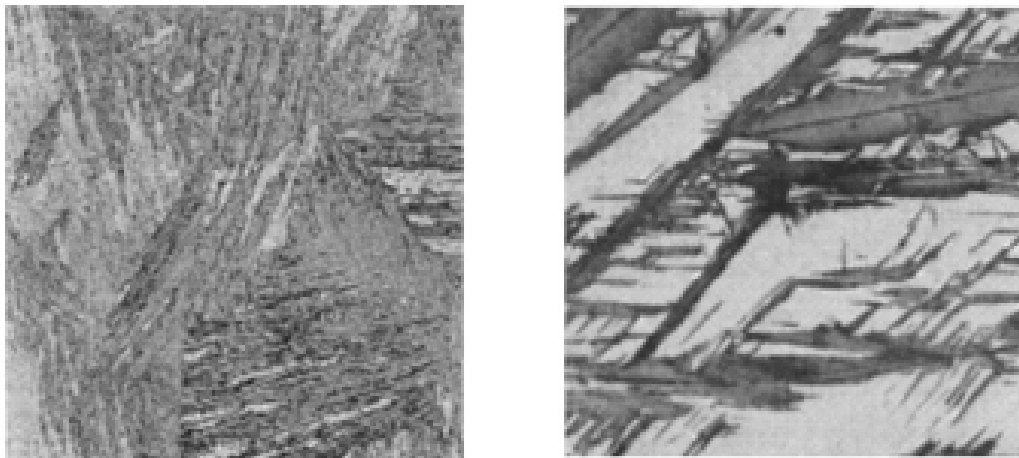


Fig. 1.7 Typical martensitic microstructures of low (left) and high (right) carbon steels. Note that the microstructures have an irregular character.

The shape memory effect (SME) is a unique property of certain alloys exhibiting martensitic transformations. A SMA that is deformed at a low temperature ($T < T_M$) recovers its original shape by the reverse transformation upon heating above a critical temperature. This effect was first found in an Au-47.5at%Cd alloy by Chang and Read,²¹ and then it was publicized with its discovery in Ni-Ti alloys by Buehler et al..²² Historical developments of the study of SME has been reviewed by Waymen et al..²³ If subsequent cooling back to the temperature of deformation does not restore the specimen to its deformed shape, this type of memory is known as the one-way SME. However, under suitable thermomechanical treatments involving the martensite and the parent phase, e.g. introducing precipitation of Ti_3Ni_4 in Ni-rich Ti-Ni alloys, thereby training the material to transform back and forth to predetermined shapes, it constitutes a two-way SME.²⁴ Obviously, the difference between the one-way SME and two-way SME is that the latter is associated with cooling. A schematic illustration of the one-way and two-way SME is given in Fig. 1.8.

Considering that the martensitic transformations are associated with hysteresis, four temperatures are generally required for characterization of the reversible SME. Transformation to austenite begins at the austenite start temperature, A_s , and ends at the austenite finish temperature, A_f . Accordingly, transformation into martensite begins at the martensite start temperature, M_s , and finishes at the temperature M_f , shown in Fig 1.9. In the following chapter 3 and chapter 4, $T_M (= (M_s + M_f) / 2)$ is used as martensitic transformation temperature for simplicity.

It has been shown in the previous section that the invariant plane strain condition is necessary in reducing strains associated with the formation of a

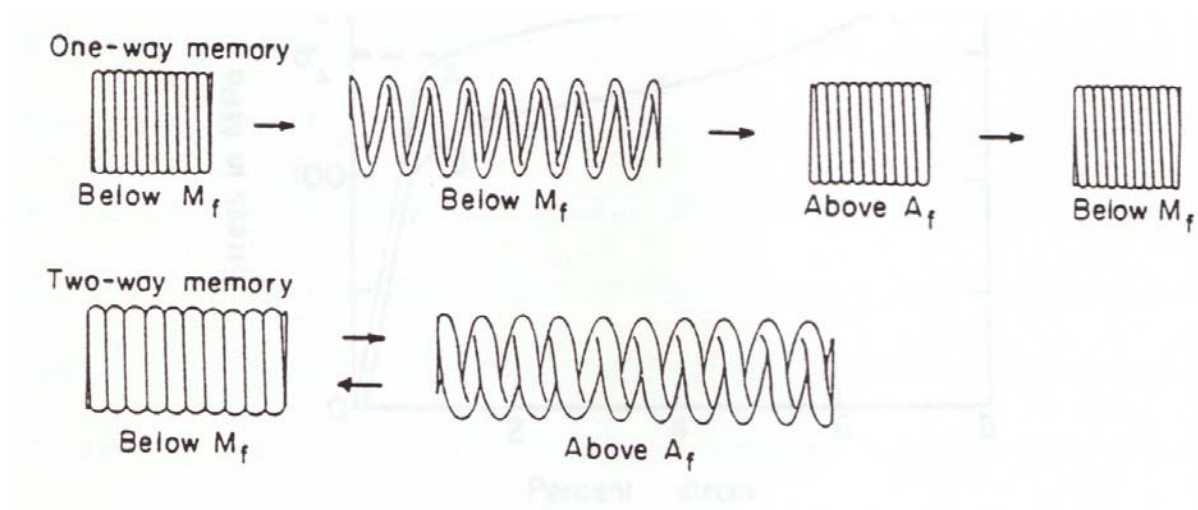


Fig. 1.8 Coil-spring example illustrating the differences between the one-way and two-way shape memories.

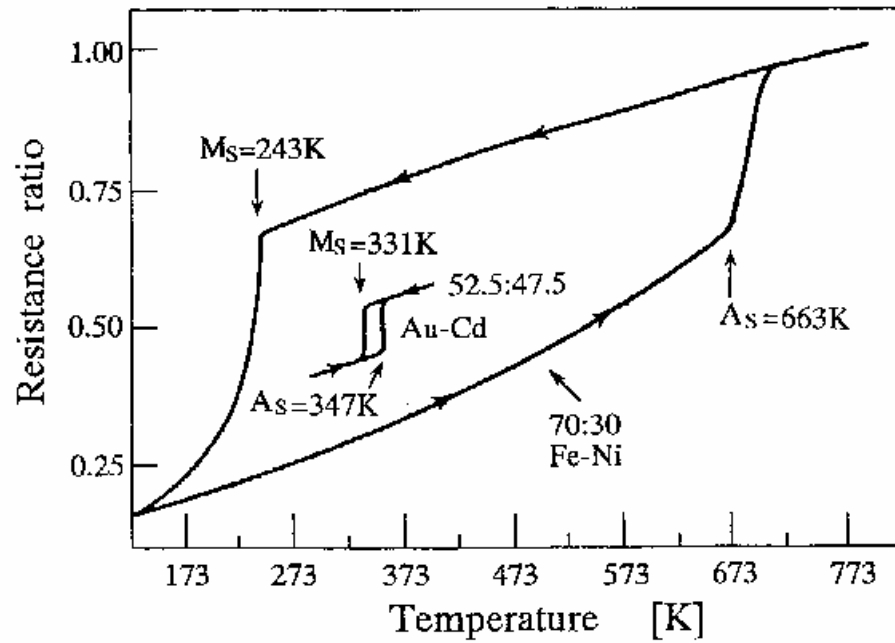


Fig. 1.9. Electrical resistance changes during cooling and heating Fe-Ni and Au-Cd alloys, illustrating the hysteresis of the martensitic transformation on cooling, and the reverse transformation on heating. (After Kaufman and Cohen)

martensite plate. However, a simple shear component is still not eliminated under this condition. As shown in Fig. 1.6 (b) and discussed before, the martensites in region A and in region B have the same structure, but their orientations are different. They are referred to as different martensitic variants. Thus, a second step strain accommodation is necessary and this may be possible by the combination of different martensitic variants, which is called the self-accommodation of martensites. The mechanism of SME is described by using a simplified model of a single crystal parent phase, as shown in Fig. 1.10 (a). Suppose a single crystal of austenite was cooled below M_f , at which temperature the entire sample has transformed, martensites are formed in a self-accommodation manner. Macroscopically, this process produces no change of the shape of the specimen. However, these martensitic variants are twin related and quite mobile. Thus, if an external stress is applied, the twin boundaries move so as to accommodate the applied stress, and it will be transformed to a single variant state if the external stress is high enough, creating a large twinning shear strain. Unloading the sample leaves it deformed, but when the specimen is heated to a temperature above A_f , the crystallographically reversible transformation causes the sample to snap back to its original macroscopic shape. An optical microscopical image illustrating self accommodation of martensitic variants in Fe-Ti-Ni has been shown in Fig. 1.10 (b).

1.5.2 Thermoelastic Shape Memory Alloys

Originally, the notion of the thermoelastic transformation was introduced by Kurdjumov and Khandros, who observed the growth and shrinkage of a martensite plate upon cooling and heating respectively, in an Au-Cd alloy.²⁵ Nowadays, a

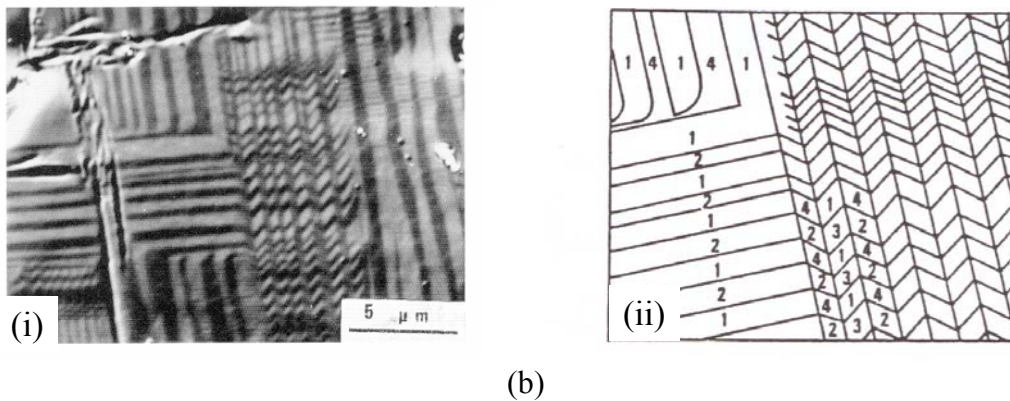
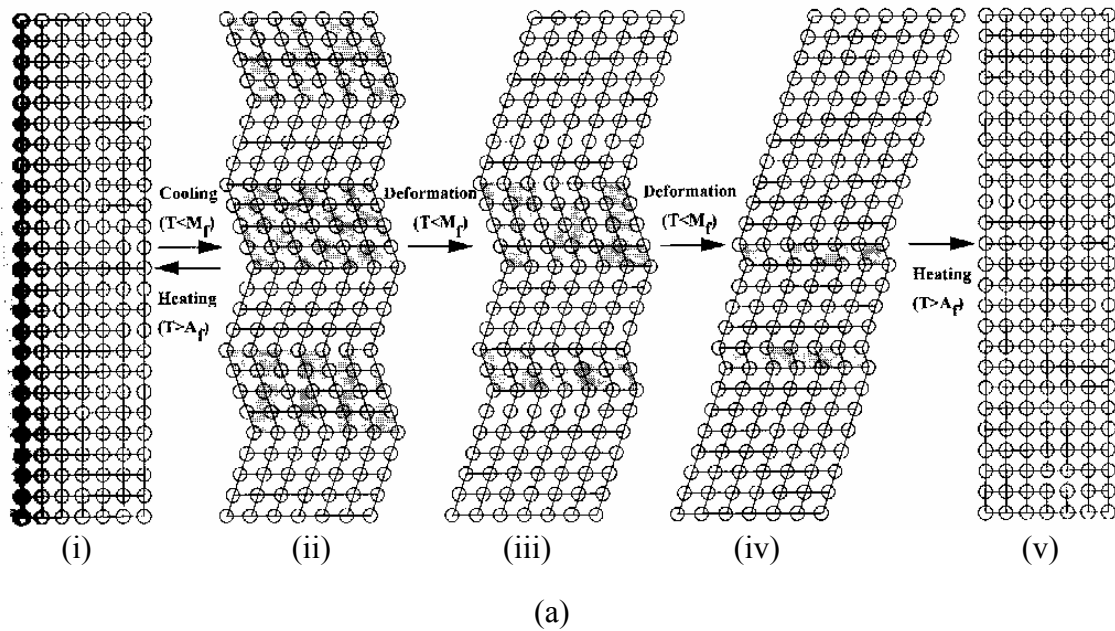


Fig. 1.10 (a) mechanism of SME; (i) original parent single crystal, (ii) self-accommodated martensite, (iii)-(iv) deformation in martensite proceeds by the growth of one variant at the expense of the other (i.e. twinning or detwinning), (v) upon heating to a temperature above A_f , each variant reverts to the parent phase in the original orientation by the reverse transformation;²⁶ (b) Optical micrograph of self-accommodation of the R-phase (Ti-48.2Ni-1.5Fe (at%) alloy).²⁷

number of thermoelastic SMAs have been extensively studied,²⁸ although none of them is as commercially useful as Nitinol.²⁹ NiTi alloys transform from the parent phase (β) with a B2 structure to the product phase with a monoclinic B19' structure, or more often in association with the two-step transformation from the β to a trigonal phase (so called R-phase) and to the B19' phase on cooling.^{30, 31, 32, 33} This transformation is reversible and effectively enables the alloy to be deformed by a shear transformation, i.e. without irreversible plastic deformation occurring, by up to 16% elongation or contraction. In contrast to the hard martensite in steel, the martensitic phase in shape memory alloys (SMAs) is pseudo-elastically soft due to twin motion. Thus the SMAs can be deformed below M_s easily and recover their original forms by re-heating to above the M_s . These unique properties are used in such applications as, e.g. toys, self-erecting space antennae, etc..

The transformation in NiTi is interesting for two reasons: first, it involves a diffusionless transformation from one ordered structure to another. Fundamentally, if the austenitic phase is ordered, the martensitic phase must also be ordered. Secondly, the mode of the transformation is such that very extensive deformation (up to 16%) can occur by a thermoelastic martensitic shear mechanism, i.e. the transformation is reversible. Another interesting feature of this transformation is that it appears to bring about an abrupt change of the apparent Young's modulus and yield strength. This change in Young's modulus also leads to distinct changes in the modulus of resilience, the 'damping' properties of the material being much greater in the NiTi martensite.³⁴

1.5.3 Ferromagnetic Shape Memory Alloys (FSMAs)

In spite of the large strain achieved, the activation of the thermoelastic SME is slow and inefficient because it depends on the transportation of heat, i.e. heating, especially cooling, of the sample. In principle, It is also possible to bring about the martensitic phase transformation by application of a magnetic field, which enables the devices to operate at high frequencies and facilitates their remote control. However, the strength of the field required is prohibitively large for practical applications.³⁵

Instead, a magnetic field can be very effective in changing the twin structure, and hence the sample shape, if the uniaxial easy direction of magnetization changes across the twin boundary and the anisotropy energy is large. Subsequently, a new form of magnetic-field-induced strain has been observed in certain SMAs within their ferromagnetic martensitic phase and these alloys that exhibit magnetic-field-induced strain (MFIS) are called ferromagnetic shape memory alloys (FSMAs).³⁶ FSMAs distinguish themselves from the thermoelastic shape memory alloys by the fact that the magnetic field induced shape change occurs fully within the low-temperature martensitic phase.

This new FSM effect is associated with the motion of twin boundaries between regions in which the magnetization direction differs. It necessitates a large magnetocrystalline anisotropy. Therefore, the field-induced strain in FSMAs arises from a mechanism different from that responsible for magnetostrictive materials, i.e. the rotation of the magnetization direction having appreciable spin-orbit coupling. In FSMAs, the application of a magnetic field in a certain direction with respect to a martensitic twin boundary can create a pressure of $\Delta M \cdot H$, due to the Zeeman energy difference, on the twin boundary. If the magnetocrystalline anisotropy is sufficiently

strong so that the moments in unfavorably orientated martensitic variants cannot rotate into the field direction, the Zeeman energy may be reduced by twin boundary motion, shown in Fig. 1.11. As a result, the martensitic variants with favorable orientation to the field grow at the expense of other variants. Eventually, the maximal magnetic field induced strain is limited by the tetragonality ($1-c/a$) ratio. The distinction between the strains due to twin boundary motion and magnetostriction is that the former is linearly proportional to magnetization, M , below saturation, while the latter is quadratically proportional to M below saturation. FSMAs can be found naturally in Fe-based alloys and a few engineered alloys, for example, FeNiCoTi.³⁷ FePt alloys³⁸ are FSMAs but their transformation temperatures are at low technologically uninteresting temperatures. Fe₇₀Pd₃₀ alloys^{33,39} are FSMAs at slightly below room temperature (RT) with reversible field-induced strains of 0.5% at -17 °C and other compositions have the potential of being engineered. FeMnSiX alloys⁴⁰ are SMAs and potentially FSMAs, but they are limited in their usefulness due to their large hysteresis.

It is thus obvious that the twin boundary motion can be induced by the mechanical stress in all the SMAs. The same effects of macroscopic deformation can be produced by exerting magnetic forces to the twin boundaries in FSMAs, which makes this new class of material technically interesting.

1.6 Premartensitic Transformations

Pre-martensitic phenomena have provoked considerable attention in recent years from researchers, and are mainly concerned with ordered compounds exhibiting order-order martensitic transformations. They have been observed in the form of

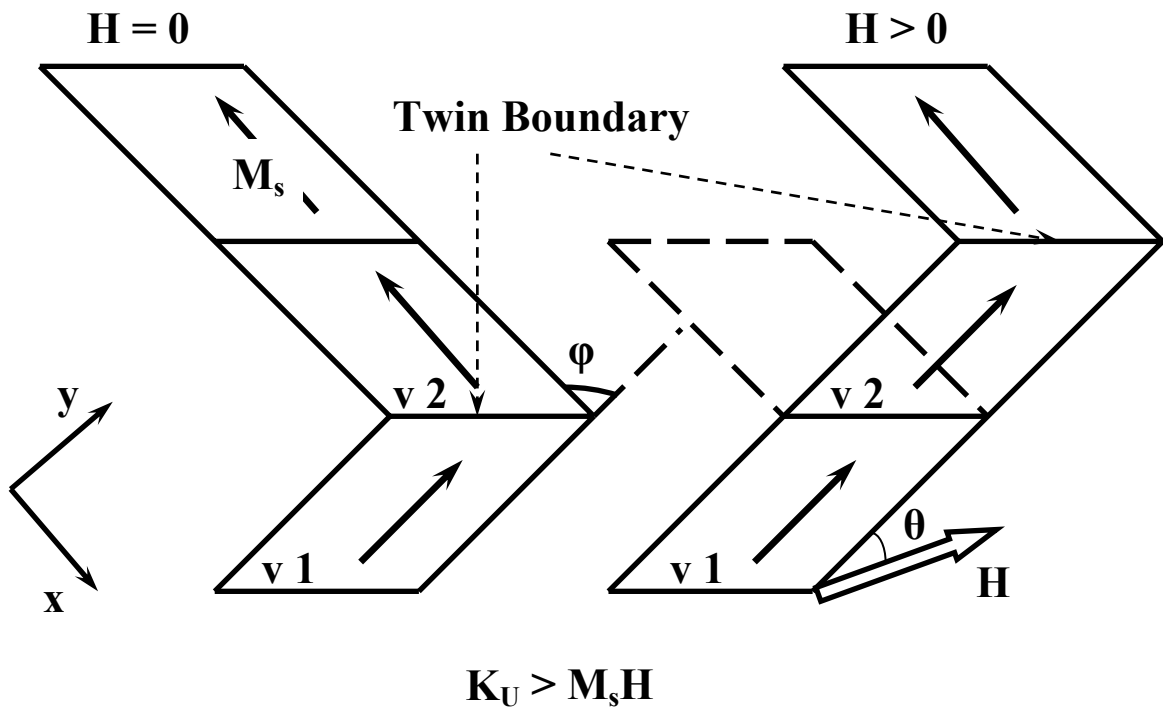


Fig. 1.11 Magnetic-field-induced twin boundary motion. If the martensitic phase is magnetic with a strong magnetocrystalline anisotropy that changes direction across the twin boundary, application of a magnetic field generates a Zeeman pressure on the twin boundary. This pressure tends to grow variant 1 at the expense of variant 2.

anomalous diffraction effects or even diffuse streaking as well as a resistivity anomaly, e.g. observed in NiTi alloys.⁴¹ It would follow that the elastic constants, or certain shear modes at finite wave vectors, decrease upon approaching the martensitic transformation from above.⁴² Considering the transformation is fcc-fct, one would expect that the elastic constant $(C_{11}-C_{12})/2$ approaches zero at the transformation temperature, which is the case in InTi, for example.⁴³ In the best known SMA, NiTi, both $(C_{11}-C_{12})/2$ and C_{44} soften prior to the formation of the monoclinic martensite phase.⁴⁴ For FSMAs, anomalies of the elastic constants are also magnetically driven.⁴⁵ Almost complete softening of $(C_{11}-C_{12})/2$ is reported in FePd.⁴⁶

Precursor phenomena are considered pretransitional not only because they occur when a phase transition is anticipated, but because they typically imply the presence of some lattice disturbance which is suggestive of the ensuing phase. It suggests that there may exist some highly effective yet very general mechanism by which the low temperature phase is making its presence felt even far into the high temperature phase. In a word, the effect is an intriguing one, particularly bearing in mind the relatively low undercoolings associated with ordered alloys, which could be conjectured that some process is occurring to effectively aid the martensitic transformation.

1.6.1 Charge Density Waves (CDW)

It is well-known that the electron concentration (e/a) is one of the most important parameters to determine the stability of crystal structure (and magnetic structure) in (ferromagnetic) shape memory alloys. This is due to a coupled distortion of the conduction electrons density and the lattice leading to an overall total decrease

in the system's energy. It is a Fermi driven phenomenon on which a modulation of the conduction electrons occurs concurrently with a lattice distortion.

Peierls⁴⁷ suggested that in a one-dimensional metal, electrons fill all the conduction-band orbits up to a wave vector K_f at absolute zero. However, such a linear metal is unstable with respect to a static lattice displacement of wave vector $G=2K_f$. A consequence of such a distortion is the creation of an energy gap at the Fermi surface, as shown in Fig. 1.12. A nesting of the Fermi surface gives rise to a lowering of the electronic energy in the figure. The distortion due to a lowering of the electronic energy is balanced by a price paid in elastic energy. The equilibrium state is achieved at

$$\left\{ \frac{d}{d\delta} (E_{elec} + E_{elas}) \right\} \Big|_{T_M} = 0 \quad (1.3)$$

where δ is the extent of deformation.

The Peierls' instability demonstrates that the martensitic transformation has a purely electronic origin, which is due to a favorable Fermi surface geometry that is necessary for the formation of a CDW. The nesting is more probable in lower dimensional systems, such as the experimentally observed 1-D conductors $KCP(K_2Pt(CN)_4)Br_{0.3} \cdot 3H_2O$ ⁴⁸ and $TTF-TCNQ$ ⁴⁹, because a simple structure is involved.

The electron-phonon coupling is essential because without it the columbic energy of the CDW would be prohibitive. Chan and Heine have demonstrated that in order to assist CDWs, a soft phonon mode is usually known to occur above the transition temperature.⁵⁰ One of the effects of a CDW is the loss of periodicity in at

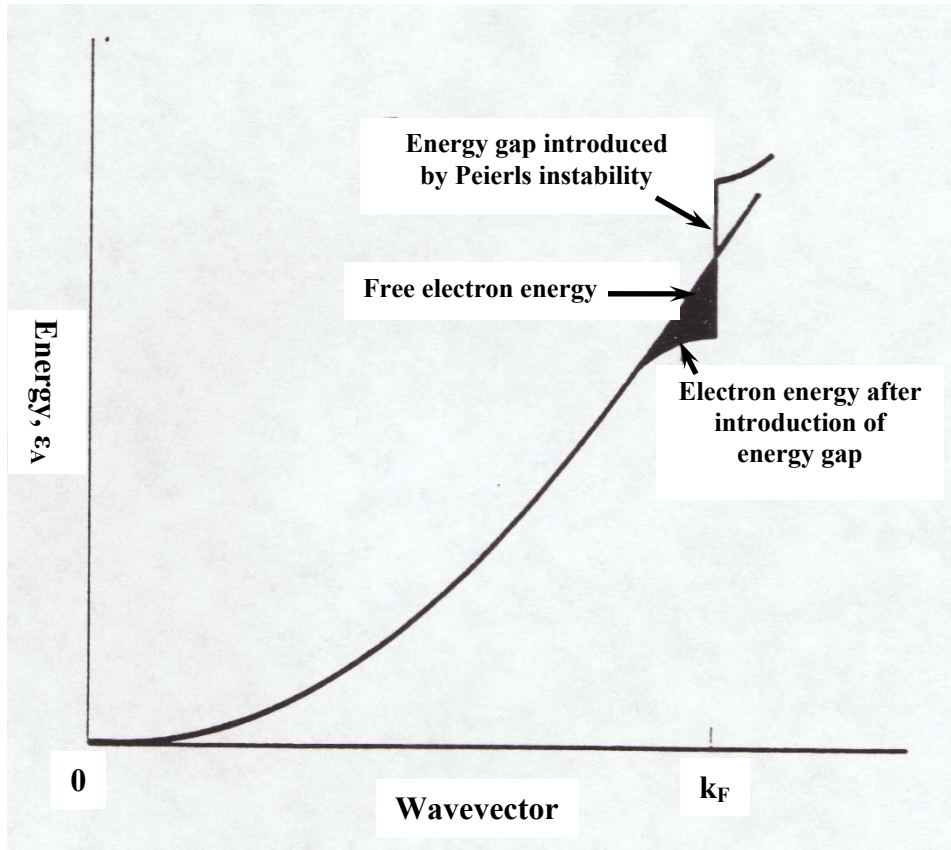


Fig. 1.12 Peierls instability. Electrons with wave vectors near the Fermi surface have their energy lowered by a lattice deformation.⁵¹

least one of the lattice directions, making the modulated crystal structure incommensurate with the basic lattice. Incommensuration arises because the wave vector of a CDW is determined by the Fermi surface and is therefore not necessarily an integral multiple of the reciprocal lattice vector of the parent phase. A further possibility of lowering the energy of an incommensurate state occurs by making the incommensurate state commensurate. Such a transition makes the lattice further undergo a distortion in which case the CDW wave vector becomes an integral fraction of the underlying lattice. This commensurate state is referred to as the “lock-in” state.

Thus two phase transformations are associated with a CDW formation: the normal parent to incommensurate transition (usually a second order) and the incommensurate to commensurate transition (first order). A lattice distortion due to a CDW can be studied by employing diffraction techniques (electron, neutron, x-ray) to reveal the satellite reflections near the Bragg peaks of the parent phase. The satellite reflections are a consequence of the new superlattice associated with the formation of a CDW. The separation of these satellites from the Bragg reflection is the reciprocal lattice vector determined by the CDW wave vector. Barsch et al. suggested that the formation of incommensurate displacement patterns in the parent lattice leading to the MT and CDWs are the underlying cause of the MT.⁵²

1.6.2 Martensite Nucleation

In order to understand the various anomalies prior to the MT, the mechanism of MT, essentially the nucleation mechanism, is worth of a brief discussion. It is now generally accepted that the martensite nucleation is heterogeneous, which relies on

some nonuniformity in the system. Early experiments on small particles of Fe-Ni alloys revealed that the fraction of transformed particles increases with decreasing temperature in a way which is particle size dependent.^{53,54} This dependence implies a nucleation mechanism which relies on pre-existing nucleation sites in the lattice. Among various nucleation mechanism proposed, the ones having received most attention are those which depend on lattice defects and pre-existing strain fields. Cohen et al.⁵⁵ advanced the theory that strain fields within the lattice could distort local regions toward the martensitic configuration, and these regions would serve as “strain embryos”, which would become unstable toward growth into the martensite as temperature was decreased below some threshold.

To study the precursor effects in MT materials, it is also helpful to explain the homogeneous transformation mechanism which is responsible in many 2nd order displacive structural transformations. Zener was the first to point out that mechanical lattice instabilities result in anomalous elastic constant behavior and phonon dispersion curves.⁵⁶ Significantly, the particular elastic modulus or phonon mode which softens in these materials is indeed the mode which measures the harmonic response of the lattice to exactly that distortion which deforms the parent lattice into the martensitic phase. Because of the recurring relationship between the softening elastic or phonon mode and the transformation temperature in the A15 compounds,^{57,58} SMAs etc.,^{59,60} the transformation is often referred as to a “soft mode transition”. The soft mode transition arises from the softening of a particular vibration mode all the way to $\omega=0$, and the ensuing mechanical instability which

drives the lattice into the martensitic deformation, initially proposed by Cochran⁶¹ and Anderson.⁶²

Until now, the nucleation of MT materials is far from being fully settled because it is extremely difficult to study this complex event which occurs at such great speeds as to exclude experimental observation. But it remains mysterious and intriguing and derives the investigations of the existence of precursor behavior which suggests that the lattice is anticipating the transformation as much as 100 K above the transformation temperature.

1.6.3 Precursor Effects

Across the whole spectrum of systems undergoing MTs, steel martensites are strongly first order; SMAs are moderately first order; the low T_C A15 compounds, In-Tl are nearly second order. The martensitic systems in the hard steel have not shown significant precursor effects except for defect related anomalies. For the moderately and weakly first order martensites, pretransitional phenomena have virtually become the norm rather than the exception. Measurements have been made of precursor anomalies in thermal expansion coefficients,⁶³ acoustic attenuation,^{64,65} internal friction,^{66,67} electrical resistivity,^{68,69} and other transport coefficients. In x-ray experiments, “ghost” spots (both commensurate⁷⁰ and incommensurate⁷¹ with the reciprocal lattice) and diffuse scattering⁷² have been observed. Neutron measurements have indicated marked pretransitional softening of entire phonon branches⁷³ and of well defined $q \neq 0$ phonons⁷⁴, as well as anomalous elastic scattering known as the “central peak”.⁷⁵ Experimental results were found to be in excellent agreement with theoretical calculations which attribute the phonon softening to

electron-phonon coupling and specific nesting properties of the Fermi surface.⁷⁶ In particular, the so-called tweed structure has been observed by high-resolution transmission electron microscopy (TEM) studies, intriguing us with the baffling nature of the precursor effects.^{46,77,78,79,80}

With a few exceptions,^{81,82} tweed is usually seen as an apparently unchanging state which is stable during aging or tempering. It appears reversibly on heating and cooling through the phase transition, and is therefore assumed to be a stable, non-transient configuration. Tweed cannot be a metastable state in which the system attempts to globally transform from austenite to martensite, because the system chooses to return to the tweed as it is reheated. Through tweed observations in TEM, it was immediately recognized that it is associated with diffraction patterns which are consistent with the presence of $\{110\}$ planes shearing in $\langle 1 \bar{1} 0 \rangle$ directions. Furthermore, it is this shear mode that couples to the elastic constant C' which is seen to soften in many MT materials as the MT temperature is approached. Hence, the tweed is not caused by a phonon instability, but is due to local inhomogeneities (e.g. compositional fluctuations, defects, residual strain) that couple to the soft modes.⁸³

SMA's undergoing a MT exhibit measurable volume and shape changes as the symmetry decreases, e.g. from cubic to tetragonal to orthorhombic, which are generally preceded by the so-called "precursor phenomena". The elastic energy induced by the lattice mismatch between the parent and product phase can be so large that it renders the nucleation of homogeneous martensite energetically unfavorable. It was proposed that the 1st order MT is mediated by constrained adaptive phases which are geometrically close to the martensitic phase and can be treated as a microscopic

limit of accommodation of twinning with twin thickness of several atom layers.⁸⁴ Experimentally, a rich variety of precursor phenomena have been observed in the vicinity of the moderately first order MT in SMAs. Some of these aforementioned precursor effects, such as the occurrence of the intermediate tweed structures and the modulated pre-martensite phase, are not common to all materials, but others are present in almost all bcc solids known so far and they are intimately related to the MT mechanism. Among them, the most significant effect is the low TA_2 [110] phonon branch ([110] propagation, $[1\bar{1}0]$ polarization), together with a low value of the elastic constant C' . Both of them soften on cooling towards T_M .

Chapter 2

Phase Transformations in NiMnGa FSMAs

2.1 Martensitic NiMnGa

2.1.1 Introduction

In 1968, P.J. Webster was the first to describe in detail the magnetic properties of a new alloy with stoichiometric composition Ni_2MnGa .^{85,86} Extensive research in Poland⁸⁷ and later on in Russia^{88,89,90} revealed the existence of a martensitic transformation in this system. Large, reversible, magnetic-field-induced strains of order 0.2% were first reported in single crystals of Ni_2MnGa by Ullakko et al. in 1996 and a shift in the martensitic transformation temperature of at most a one or two degree under 10 kOe magnetic field was also reported.⁹¹ In 1997, Ullakko and coworkers⁹² and a little later Wuttig and James first suggested and established that this transformation can be used in the form of a two-way shape memory (SM) effect. In 1999, a 5% shear strain was discovered at RT in a field of 4 kOe in 5-layer tetragonal NiMnGa martensite by Murray et al..⁹³ More recently, the MFIS close to 10% was found in 7-layer orthorhombic NiMnGa modulated martensite,⁹⁴ which is, as for now, the largest MFIS attained in FSMAs.

The necessary conditions for the occurrence of FSMAs have been overviewed by Wuttig et al.^{36,95} and a constrained theory of magnetostriction intended to describe strain versus field and the associated microstructural changes in these materials is given by DeSimone and James.⁹⁶ Various phenomenological models have been

proposed to understand the elastic and magnetic properties in FSMAs. O'Handley⁹⁷ presents a model for the magnetization process, field-induced strain by twin-boundary and phase-boundary motion and accounts for the magnetic anisotropy, based on a particular twinned domain structure. It shows good agreement with experimental data of Ullakko et al. and suggests that the competition of twin blocking stress and magnetic driving force leads to a restricted temperature window for magnetic actuation using Ni₂MnGa alloys. L'vov⁹⁸ starts from an expression for the Helmholtz free energy of a cubic crystal to derive the expressions for the static magnetic susceptibility and for the magnetization of the martensite. Their analysis demonstrates that the magnetization of FSMAs is closely related to the spontaneous strains arising at martensitic temperature T_M , which indicates a strong magneto-elastic coupling in the vicinity of martensitic phase transformation.

2.1.2 Crystal Structures of Martensitic NiMnGa

The crystal structure of Ni₂MnGa alloys has been extensively studied by means of x-ray or electron diffraction, TEM and neutron diffraction. Neutron diffraction is a more powerful tool than x-ray because the coherent nuclear scattering amplitudes of the constituent atoms are significantly different so that the second neighbor ordering, as well as the occupancies of the different atomic sites can be determined.

The crystal structure of the austenite phase in the stoichiometric alloy has been determined as cubic with L2₁ (Heusler) atomic order (space group: $Fm\bar{3}m$). Fig. 2.1 depicts a unit cell of an austenitic phase of Ni₂MnGa.

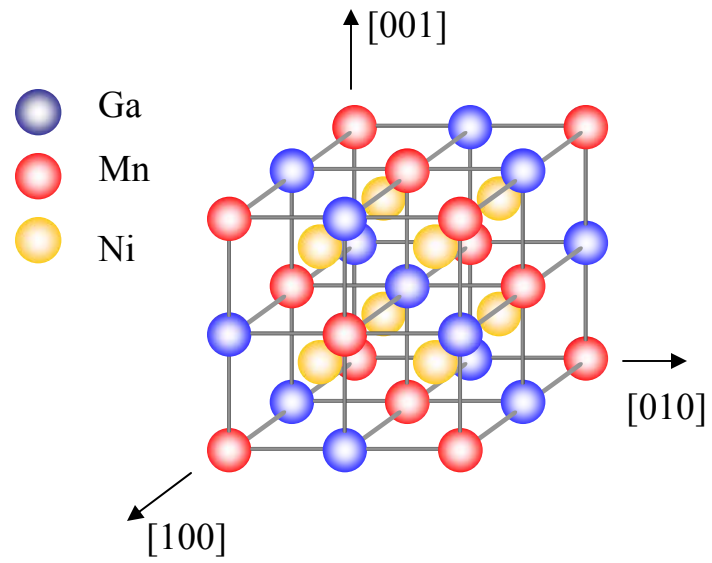


Fig. 2.1 $L2_1$ cubic structure of NiMnGa austenite phase.

Through the studies of composition dependence of lattice stability in NiMnGa alloys, different types of martensitic phases of lower symmetry have been identified based on the different modulations along specific crystallographic directions, as shown in Fig. 2.2. And it is suggested that the nonstoichiometric compositions are more suitable candidates to obtain large strains at higher temperatures. It should be noted that the crystallographic axes of all following martensitic structures correspond to the axes of the austenite structure (cubic lattice). However, the crystallographic axes of the martensitic unit cell are aligned along $[\bar{1}10]$, $[001]$ and $[110]$ directions of the cubic parent phase.

3-layered modulation (3M):

3-layer modulation of the lattice has been observed in certain crystals, although the cubic symmetry of the lattice has not been changed. This structure is related to a pre-martensitic phase, which will be introduced in details in the next section.

5-layered modulation (5M):

Early Neutron diffraction data showed that during martensitic transformation, a simple contraction along one of the $\langle 100 \rangle$ directions of the cubic occurred. There is a strong deformation of the cell ($c/a = 0.94$), however, only accompanied by a 1% decrease in cell volume. This martensitic structure is formed by the tetragonal distortion of the parent $L2_1$ phase and the martensitic lattice is subjected to periodic shuffling along the $(110)[\bar{1}10]$ system and the modulation period is five (110) planes, which is the so-called 5-layered martensite of body-centered tetragonal structure(space group: $I4/mma$).^{99,100} It is the martensitic phase in

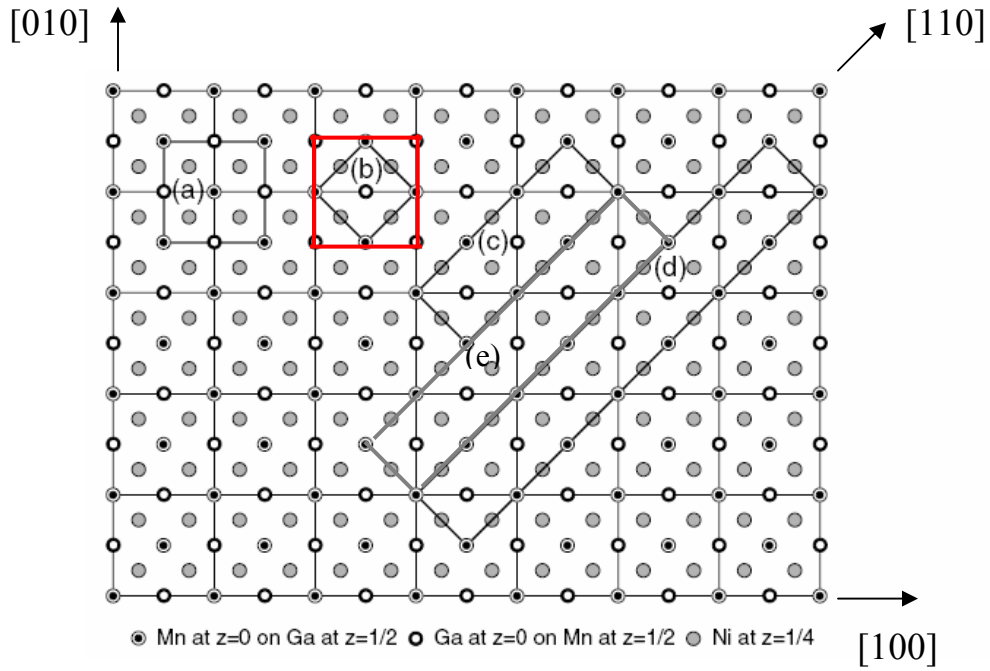


Fig. 2.2 Projection on (001) of the ideal $L2_1$ Heusler alloy structure showing: (a) the $L2_1$ unit cell, (b) the body centered tetragonal unit cell, the red square is a tetragonal cell, comparable to the cubic cell (a), (c) the premartensitic 3M super-cell (d) the martensitic 7M super-cell (e) the martensitic 5M super-cell. All the cells have the same c axis perpendicular to paper.¹⁰¹

which a maximum 6% strain is can be induced by a magnetic field. Fig. 2.3 illustrates the stacking sequences of the 5-layered structure observed in NiMnAl alloys.¹⁰²

7-layered modulation (7M):

A variant showing a 7-layered modulation was found in stressed martensites. It has a body-centered monoclinic (close to orthorhombic) structure with seven (110) plane modulation (space group: Pnnm). When the long a-axis is aligned into the short c-axis direction, the martensitic variant produces a 10% strain as pointed out early in this chapter.

Non-modulated structure (T):

In NiMnGa alloys with a relatively high martensitic transformation temperature, a body-centered tetragonal structure having $c/a > 1$ without modulation has been reported.⁹⁹ An analysis of the X-ray patterns indicates that the structure is the face-centered tetragonal (BCT) $L1_0$.¹⁰³ The unit cell of $L1_0$ lattice and the correspondence between the B2-type lattice and $L1_0$ lattice are depicted in Fig. 2.4. This transition is also the Bain-type distortion as a path from BCC to FCC. The non-modulated martensite receives less attention because both the compressive stress required to obtain a single variant state and the blocking stress on the twin boundaries for variant-reorientation are so high that the magnetic field required to induce the shape change is beyond industrial capacity.¹⁰⁴

Other more complicated modulations, such as 8M and 10M, involved in the martensitic phase in NiMnGa alloys have been reported, but the structure and properties of these modulated phases are less studied and understood.^{105,106,107}

2.1.3 Magnetic-field-induced Strains in NiMnGa

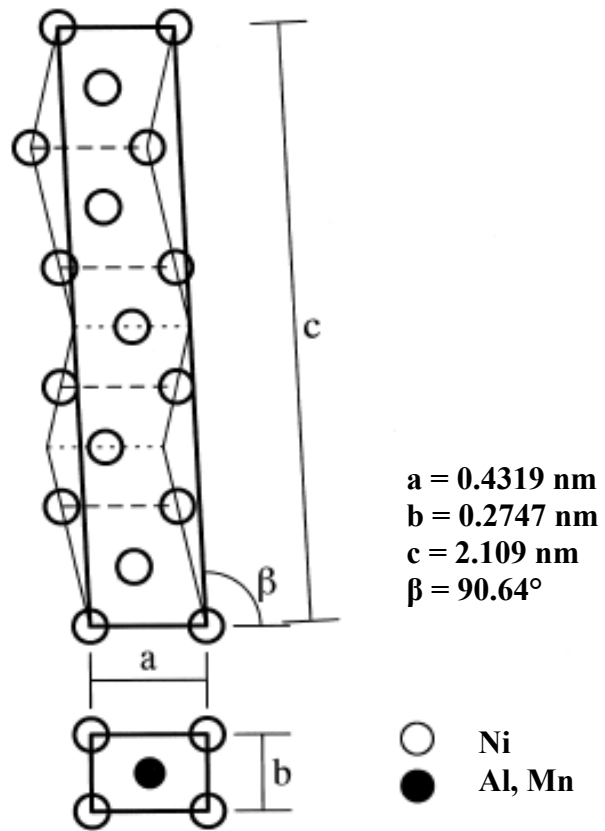


Fig. 2.3 The structure of 10M martensite and the lattice parameters obtained from the electron diffraction patterns for $\text{Ni}_{50}\text{Al}_{19}\text{Mn}_{31}$ alloy.

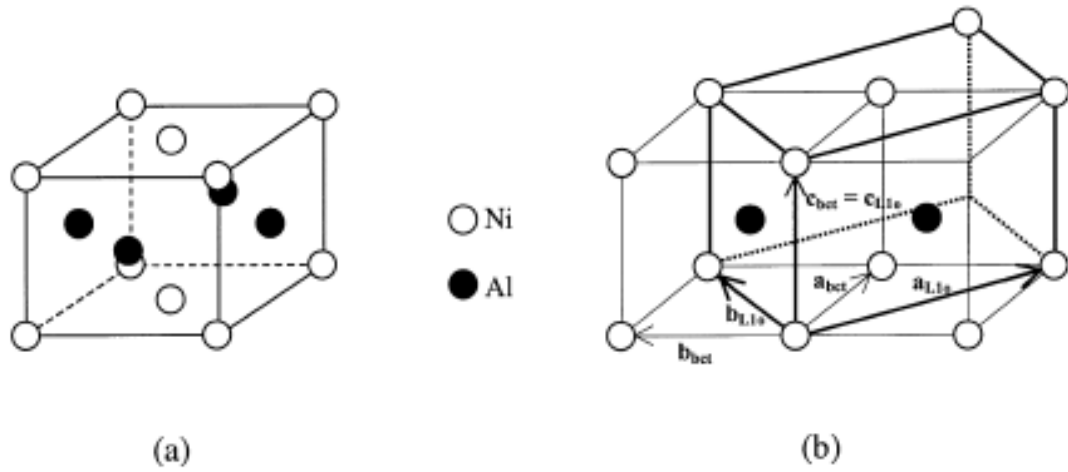


Fig. 2.4 (a) Scheme of the $L1_0$ cell. (b) Lattice correspondence between the “cubic” axes and those for the $L1_0$ cell.

As mentioned earlier, the large mechanical strain induced by the magnetic field is realized through the twin boundary motion and martensitic variant redistribution. The thermodynamic driving forces should have a magnetic component and be connected with high magnetic anisotropy and significant differences in magnetization free energies for different martensitic variants. Hence, magnetic anisotropy energy is a key property to understand the FSM effects in martensitic NiMnGa. Considering a tetragonal ferromagnetic crystal with a uniaxial anisotropy, the energy density of the anisotropy is written as:¹⁰⁸

$$E_{ma} = K_{u1} \sin^2 \theta + K_{u2} \sin^4 \theta + K_{u3} \sin^4 \theta \cos 4\varphi \quad (2.1)$$

where θ and φ are polar coordinates, K_{ui} are the magnetic anisotropy constants. If K_{u1} is positive, the crystal has an easy axis of magnetization along the c axis (5M). If K_{u1} is negative and $K_{u1} < -2K_{u2}$, the crystal has an easy plane of magnetization, in which the ab-plane is the easy plane and the c axis is the hard magnetization direction (T). For an orthorhombic crystal, the magnetic anisotropy energy is expressed using directional cosines α_i as:

$$E_a = K_1 \alpha_1^2 + K_2 \alpha_2^2 + K_3 \alpha_3^2 + K_4 \alpha_1^2 \alpha_2^2 + K_5 \alpha_2^4 \quad (2.2)$$

For 7M martensite, experimental results show that K_1 and K_2 are the predominant terms in the above equation (2.2), which refers to two axes [100] and [010] that can be described as hard and intermediate axes.^{109,110}

The structural, magnetic and mechanical properties of martensitic phases in NiMnGa with tetragonal 5M, (close to) orthorhombic 7M, and nonlayered tetragonal T crystal structures have been studied. The results have been summarized by Sozinov et al. and collected in table 2.1.¹¹¹ In NiMnGa alloys, both the austenitic and

Martensite type	5M (c/a<1)	T (c/a>1)	7M (a>b>c)
Composition, at% ($\pm 0.5\%$)	Ni _{49.2} Mn _{29.6} Ga _{21.2}	Ni _{52.1} Mn _{27.3} Ga _{20.6}	Ni _{48.8} Mn _{29.7} Ga _{21.5}
Lattice parameters, nm	a=0.594 b=0.594 c=0.559	a=0.546 b=0.546 c=0.658	a=0.619 b=0.580 c=0.553
Cell volume, nm ³	0.197	0.196	0.199
$\epsilon_0=(1-c/a)\%$	5.89	20.5	10.66
σ^s , MPa	1	12-20	1.1
σ^f , MPa	2.1	12-20	1.9
$(\mu_0 M_s)$, T	0.6 \pm 0.05	0.6 \pm 0.05	0.6 \pm 0.05
Magnetic anisotropy 10 ⁵ J/m ³	1.45 (K _u)	-2.03 (K _u)	1.6 (K _a) 0.7 (K _b)
MSM strain, %	5.8	Less than 0.02	9.4

Table 2.1 Single-crystal samples of martensitic NiMnGa with different crystal structures at RT.

martensitic phases are ferromagnetic with the magnetic moment confined mainly in the Mn sites as shown by neutron diffraction experiments and theoretical calculations.¹¹² However, the largest contribution to the magnetic anisotropy energy comes from Ni, according to Enkovaara et al..¹¹³

2.2 Pre-martensitic NiMnGa

The martensitic transition in SMAs is first order transformation, which is due to the anharmonic coupling between a phonon on the transverse TA₂ branch and the long-wavelength shear mode related to C'.^{114, 115} The precursor phenomena in thermoelastic SMAs, which originate from the electron-phonon coupling and specific nesting features of the Fermi surface,¹¹⁶ are expected to be a second order transformation as a consequence of weak restoring forces in specific crystallographic directions that announce the possibility of a dynamical instability. Recently, interest in the study of FSMAs had increased since their ferromagnetic properties provide an additional degree of freedom to control the shape memory effect associated with the martensitic phase transformation. Scientifically, the NiMnGa system in its stability range offers various scenarios to investigate the coexisting interactions of electron-phonon, magnetoelastic and Jahn-Teller mechanisms.

2.2.1 Multi-stage Transformations in NiMnGa

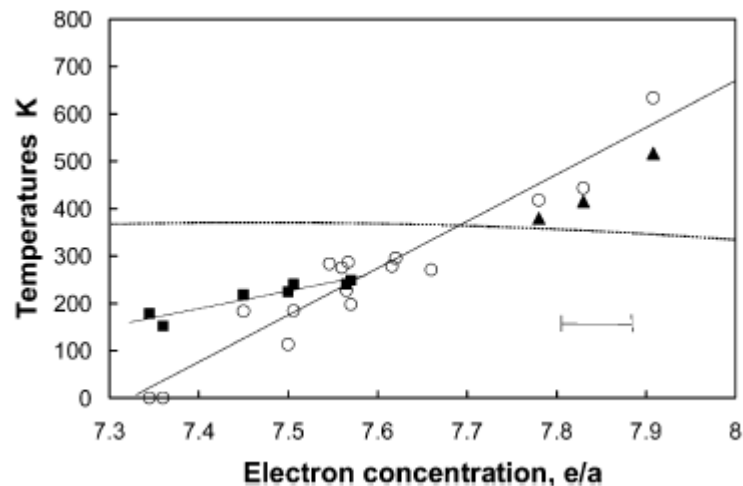
Extensive studies have been carried out to investigate the stability of the magnetic and crystallographic structures in NiMnGa alloys,^{117,118} the transformation path is found to be composition dependent and firstly described by plotting the different transformation temperatures as functions of an empirical parameter α known as a weighted composition ($\alpha = x \text{ at\%Ga} + y \text{ at\%Mn}$, with $x + y = 1$).^{119,120} The phase

diagram is better depicted in terms of the average valence electrons per atom (e/a) considering the electronic origin of the MT,^{121,122} shown in Fig. 2.5 (a). Noteworthy, the Curie temperature does not change much with varying electron concentration, but the martensitic transformation temperature and the intermediate transformation temperature increase linearly with increasing e/a ratio. At $e/a \approx 7.7$, the magnetic and structural transformation temperatures merge. In terms of presence or absence of different modulated phases, we can broadly classify NiMnGa alloys into 3 categories.

Group I is composed of alloys with $e/a < 7.6$ and T_M below RT. These alloys exhibit both the intermediate (incommensurate and commensurate) transformations, as observed in α -U.¹²³ The sequential appearances of austenite, incommensurate phase, commensurate phase and martensite on cooling have recently been summarized and sketched in Fig. 2.5 (b).

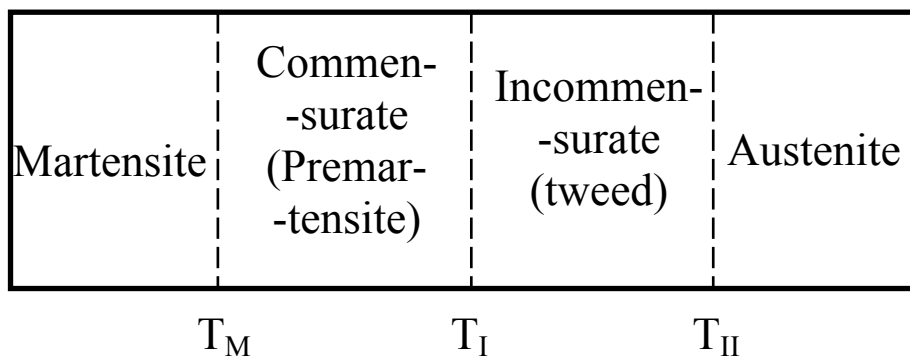
Alloys in Group II are characterized by a suppressed commensurate transformation ($T_I = T_M$). This is similar to the cases of NiAl,^{124,125} FePd,¹²⁶ FePt¹²⁷ and In-Tl¹²⁸ materials. Incommensurate phases (referred to as tweed, in real space) are present in these materials, but the commensurate phases are absent prior to the MT.

Group III holds alloys with $e/a > 7.7$ and $T_M < T_C$. The martensitic phase transformation occurs before the ferromagnetic phase transition. Austenite transforms directly into martensite without any commensurate structure observed. These behaviors are comparable to those found in Cu-based SMAs, which are classified as ordinary SMAs with entropy driven MT.^{129,130}



(a)

← Temperature



(b)

Fig. 2.5 (a) Characteristic phase transformation temperatures as a function of the electron concentration for NiMnGa alloys. The uncertainty for e/a is shown by the horizontal error bar; (b) Paradigm of the multistage displacive structural transformations with modulated precursor phases of NiMnGa alloys with $e/a < 7.6$.

The evolution of crystal structures changes along different paths in NiMnGa has been studied via TEM by a few research groups. The unstrained image of L2₁ structure is a square pattern of sharply aligned white dots.¹³¹ Upon cooling towards T_M, the corresponding microstructure of the parent phase exhibits well pronounced precursor effects, in the form of dynamically modulated structure and intense diffuse streaking along <110> crystallographic directions. The normal L2₁ cubic patterns are severely disturbed, reflecting an inhomogeneous assembly of ultrafine locally distorted regions randomly distributed in the parent phase, known as the tweed strain contrast, resolved by high-resolution, multibeam phase contrast imaging (HRTEM) and the results are shown in Fig. 2.6.¹³² Further studies indicate that for alloys belonging to group I, the diffuse streaking on the diffraction patterns increases on cooling but is abruptly replaced by the well pronounced system of sharp Bragg-like satellites, characteristic of the commensurate phase at T_I.¹³³ Thus, T_I is defined as the pre-martensitic phase transformation temperature in NiMnGa FSMA. Later, TEM images show that the cubic symmetry of the crystal lattice of the high temperature parent phase is kept unchanged between T_I and T_M.¹³⁴ The extra spots in the TEM patterns indicate the lattice of commensurate, premartensitic phase is three times larger than the lattice of the parent phase. In contrast, the in situ slow cooling TEM observations confirm the lack of commensurate phase formation close to T_M for alloys in group II. Weak and diffuse maxima located at the same positions as the satellites of the commensurate phase are visible close to T_M, however, the appearance of weak spots in among the streaks never becomes sharp before transforming into 5-layered martensite. Thus, the stability towards the shear to the 5-layered tetragonal

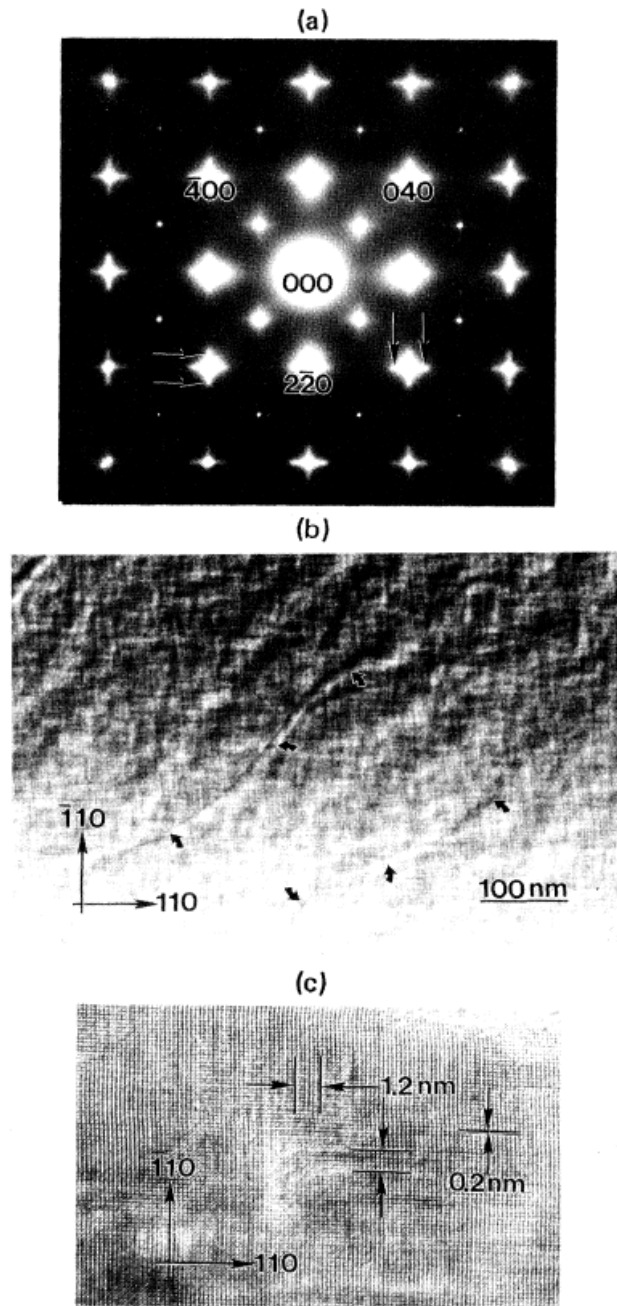


Fig. 2.6 (a) A symmetric (001) zone-axis electron diffraction patterns of the high-temperature parent $L2_1$ structure obtained at 293 K. (b) The CTEM microstructural image produced under two-beam bright-field condition; (c) The HRTEM microstructural image showing local atomic displacements and domain structure.

structure shows up prior to the soft mode condensation characteristic of the commensurate pre-martensite phase. Investigations on alloys of group III indicate that a sequence of martensitic and intermartensitic transformations takes place, whereas the low temperature martensitic phase directly reverts to the parent phase on heating. No pre-martensitic phase transformation has been identified.

Now, we would like to clarify two key points to the general framework for the different multi-stage transformation mechanisms in MTs of NiMnGa system.

The displacive structural transformation to the low symmetry martensitic phase, under certain circumstances, is preceded by a transformation in which an incommensurate phase (referred to as “tweed” in real space) locks into a commensurate modulation. Studies of the pertinent phase diagram of Fig. 2.5(a) reveal that the commensurate phase may or may not be observed but never without a preceding incommensurate modulation.

Although dynamical precursors of parent phase in a wide composition range of NiMnGa generally exist, eventually, two types of independent lattice instabilities are in mutual competition. Consequently, the materials will transform either directly by the martensitic transformation (e.g. alloys in group III) or through a soft mode condensed phase transformation (e.g. alloys in group I). As a consequence, the premartensitic transformation becomes less likely as T_M increases.

2.2.2 Precursor Effects

The behavior of Young’s modulus, E , is very sensitive to the occurrence of both the premartensitic and the martensitic phase transformation. The measurements of the Young modulus of various NiMnGa alloys have been done and are shown in

Fig. 2.7. An almost linear softening of E of the parent phase, not only in ferromagnetic state but also in paramagnetic state, has been observed, demonstrating the lattice instability of the cubic structure before reaching T_M or T_I . Below T_M or T_I , alloys of different categories display many different behaviors. Alloys in group I show two minima in $E(T)$ curve, clearly marking the boundaries of the premartensitic and the martensitic transformation, respectively. Only one minimum identified in the $E(T)$ curve of alloys belonging to group II, which corresponds to the martensitic transformation. And alloys in group III display additional stiffening at the ferromagnetic ordering temperature in martensite, suggesting a two-step martensitic phase transformation. On cooling, the E modulus shows stiffening at a higher rate in martensite than the softening in austenite.

The two shear elastic constants C_{44} and C' show noticeable decrease at the pre-martensitic transformation temperature for alloys of group I, indicating partial dynamical instability for all long wavelength shear distortions. On the other hand, the longitudinal elastic constants C_{11} and C_L do not exhibit anomalous behavior.^{135,136,137} The softening of C' , associated with a shear of the $\{110\}$ plane along the $\langle 1\bar{1}0 \rangle$ directions, is more pronounced than that of C_{44} , resulting in a relative increase of the elastic anisotropy (C_{44}/C') at the intermediate phase transition. No elastic constant vanishes at the pre-martensitic transformation point, suggesting the pre-martensitic transformation in NiMnGa rather a (weak) first order transition than a continuous one. Marked increases of C' and C_{44} on further cooling below T_I are reported in the premartensitic phase, which clearly indicates the formation of commensurate phase prior to the MT.

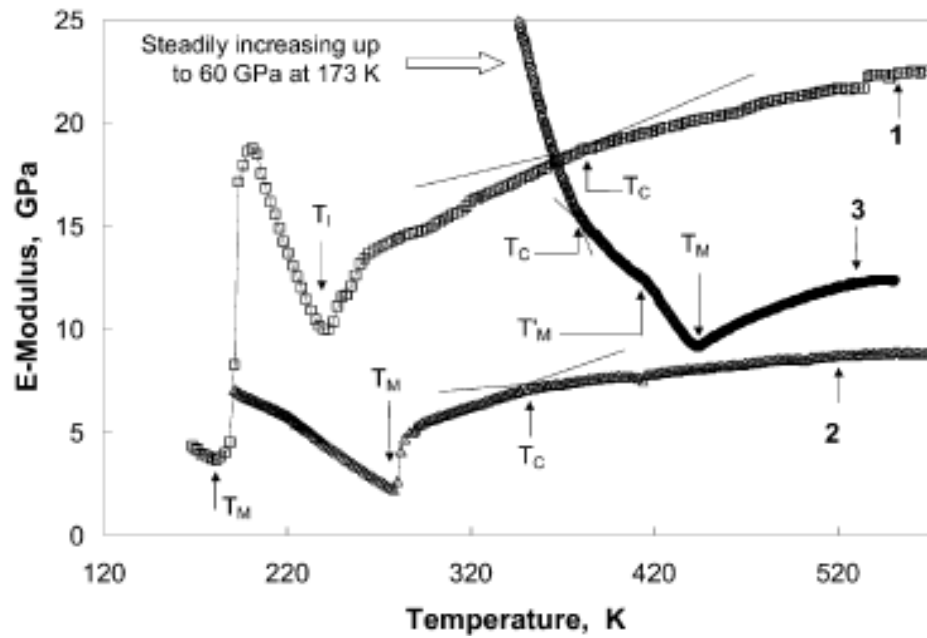


Fig. 2.7 Elastic modulus vs. temperature curves recorded during cooling for NiMnGa alloys of group I, II, and III, respectively.

The dependence of the elastic constants on uniaxial compressive stress and magnetic field has been studied.^{138,139,140} C_L , C' and C_{44} are all found to increase up to a saturation value with increasing magnetic field up to 6 kOe. And all elastic constants increase with increasing stress, indicating an overall stiffening of the crystal. The increase is nonlinear and seems to reach a saturation value under a maximum stress of 10 MPa during the experiments. The relative changes of the elastic constants are larger than that expected from purely vibrational anharmonic contributions. It is proposed by these authors that the application of a uniaxial stress may induce rotation of magnetic domains and change the magnetization, giving rise to a modification of the values of elastic constants. Hence, the anomalous behavior of stress dependence of elastic constants undoubtedly demonstrates the existence of a magnetoelastic interaction in NiMnGa FSMAs. On the other hand, the magnetic field dependence of all the elastic constants correlates with the square of the magnetization, consistent with the bilinear coupling between the magnetization and the homogeneous shear proposed before.¹⁴¹

Being the only known ferromagnetic Heusler alloys undergoing a martensitic transformation, NiMnGa alloys have been extensively investigated the lattice stability through phonon anomalies by inelastic neutron scattering.

Phonon dispersion curves of stoichiometric Ni₂MnGa single crystals have been determined and are shown in Fig. 2.8.¹⁴² The significant $(\zeta \zeta 0)$ TA₂ phonon softening, together with a dip of phonon frequency at a wave vector $\zeta_0 \approx 0.33$ has been observed. This phonon branch, for ζ close to 0, corresponds to the elastic constant C' , which is anomalously low in parent phase in NiMnGa alloys. In addition,

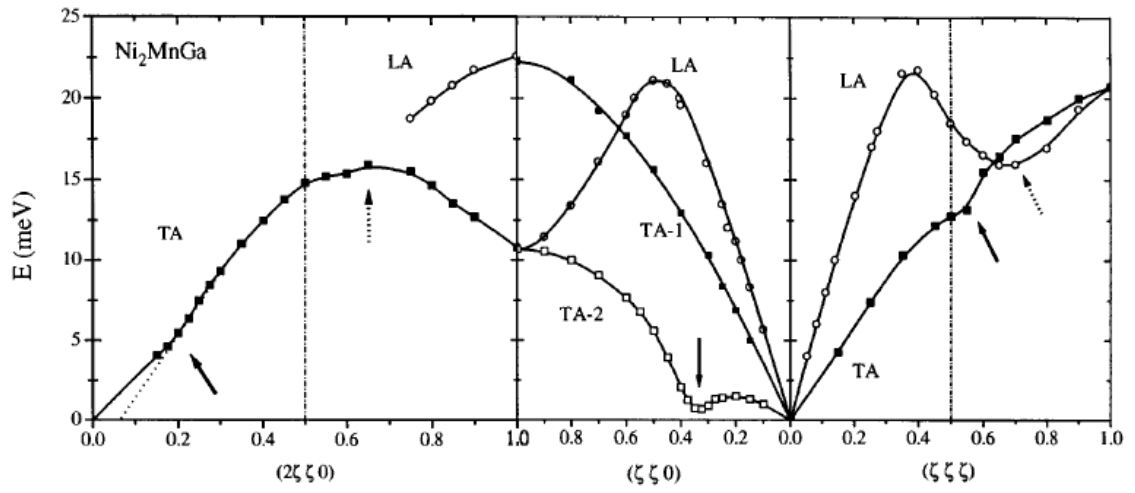


Fig. 2.8 Measured acoustic-phonon dispersion curves for the parent $L2_1$ phase of Ni_2MnGa .

slight wiggles at finite wave vectors in the $(\zeta \zeta \zeta)$ and $(2\zeta \zeta 0)$ TA branch and dip in $(\zeta \zeta \zeta)$ LA branch at $[2/3, 2/3, 2/3]$ are reported and attributed to e-ph coupling and coulomb contribution, respectively.

The most striking feature is the strong temperature dependence of the TA_2 branch with polarization along $[1 \bar{1} 0]$, plotted in Fig. 2.9. The wiggle in this branch eventually leads to a distinct minimum at $\zeta_0 \approx 0.33$ upon cooling to T_I , although the phonon frequency never softens completely, i.e. its energy remains finite. An up-turn of the phonon frequency of the soft mode is observed slightly below T_I , accompanied by an abrupt change of diffuse patterns from diffuse streaking to sharp Bragg-like satellites, confirming that the development of commensurate pre-martensitic phase between T_I and T_M . Thus, the pre-martensitic phase involves a $[1/3 \ 1/3 \ 0]$ modulation along the $[1 \bar{1} 0]$ crystallographic direction of the austenite $L2_1$ Heusler structure, so-called 3-layered modulation.

Considering the influence of mode softening on mean square atomic displacements, the following expression should be used:¹⁴³

$$|u_q|^2 \approx \frac{kT}{NM\omega^2(q)} \quad (2.3)$$

where $|u_q|^2$ is the contribution of the phonon with wave vector q and frequency ω to the atom mean square displacement. N is the number of atoms with mass M and k is the Boltzmann constant. It can be seen that if the contribution of vibrations with $q \neq 0$ and $\omega \rightarrow 0$ (soft mode in premartensitic NiMnGa) dominates, the amplitudes of the thermal vibrations of atoms increase at the soft mode condensation temperature. Consequently, the interatomic distances are enlarged due to the anharmonic effects.

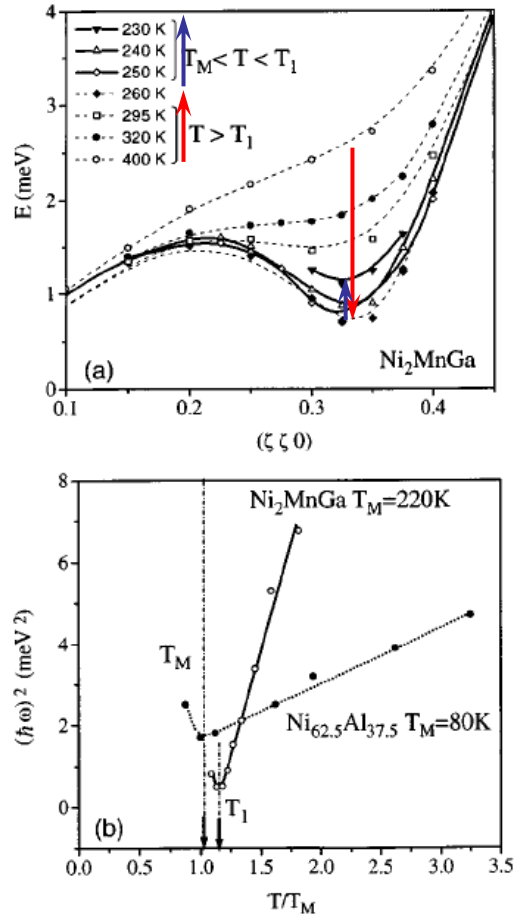


Fig. 2.9 (a) Temperature dependence of the phonon anomaly in the $(\zeta, \zeta, 0)$ TA_2 branch in the parent and the premartensitic phases of Ni_2MnGa . (b) $(\hbar\omega)^2$ vs T/T_M for the $(\zeta, \zeta, 0)$ TA_2 mode for Ni_2MnGa and $\text{Ni}_{62.5}\text{Al}_{37.5}$ in the point where the dispersion curve is a minimum.

In case of NiMnGa alloys, the lattice parameter of the premartensitic phase (at $T_M < T < T_I$) becomes three times larger, compared to that of the $L2_1$ structure (at $T > T_I$), although the cubic symmetry has not been changed. It indicates that this premartensitic transformation in NiMnGa is an independent structural transformation that only involves shuffle strains but not the final tetragonal martensite strain.

Zheludev et al. indicated that the wiggle of TA_2 soft phonon persisted above the Curie point in stoichiometric Ni_2MnGa , which eliminates the magnetoelastic origin of the premartensitic phase transformation. Two years later, a careful plotting of the square of the phonon energy, $(\hbar\omega)^2$ measured at the dip of the TA_2 branch, as a function of temperature by Stuhr et al. shows a linear dependence, but with a distinct slope change at T_C ,¹⁴⁴ strongly suggesting that the phonon softening depends on the magnetic ordering in this material. Hence, the magnetoelastic coupling (magnon-phonon interaction) not only influences the MT, but enhances, if not originates, the pre-martensitic phase transformation as well in NiMnGa FSMA.

The modulated premartensitic phase has only been observed in alloys of group I, in which the T_M is separated sufficiently from T_C . In these alloys, the magnetoelastic interaction is sufficiently strong so that the soft phonon is frozen below T_I and the system is driven through a premartensitic transformation. Without finding an up-turn of phonon energy above T_M , Stuhr et al. excluded the premartensitic phase in their non-stoichiometric NiMnGa sample, which is expected to belong to group II. It is suggested that the occurrence of MT at high temperatures prevents the frequency of the soft phonon from reaching a value small enough to enable the development of the premartensite phase.¹⁴⁵ In group III, the occurrence of

the martensitic transition inhibits the existence of the premartensitic phase because the magnetic contribution is absent (Structural transformation takes place prior to the ferromagnetic one). Phonon anomalies in non-magnetic NiAl alloys and NiMnGa FSMAs are listed in Table 2.2, where the role of magnetoelastic coupling is clearly illustrated.

In addition, internal friction¹⁴⁶ and resistivity measurements¹⁴⁷ clearly state the premartensitic phase transformation of alloys in group I. A small latent heat about 9 J/mol (Latent heat of MT: 100 J/mol) convincingly stresses that the premartensitic transformation of NiMnGa alloys at T_1 is a weakly first-order transformation preceding the formation of martensite.¹⁴⁸ Landau models for the premartensitic transformation¹⁴⁹ have been proposed and successfully explain that: i) the electron-phonon originates a first order premartensitic transformation from a bcc to a micromodulated phase in NiMnGa; ii) the magnetoelastic coupling enables the existence of a commensurate phase prior to the MT. Details of the Landau theory applying to the premartensitic phase transformation in NiMnGa will be discussed in Chapter 4, together with our experimental results.

2.3 Research Motivations

According to the discussion given above, NiMnGa martensites with $c/a < 1$ are technically interesting in terms of the magnetic shape memory effect. Magnetic anisotropy is one of the important factors to determine the MFIS in NiMnGa alloys, because it provides the underpinning of the driving force for field induced twin boundary motion. Until now the temperature dependence of the FSME has not been fully understood because the accommodation of the NiMnGa martensite gives rise to

NiMnGa FSMAs	Non-magnetic NiAl
Phonon softening is along specific crystallographic directions, which is along $\langle 110 \rangle$.	
Phonon energy, $(h\omega)^2$, decreases linearly on cooling to T_M , announcing lattice instability prior to MT.	
Dip $(1/3 \ 1/3 \ 0)$ at the $(\zeta, \zeta, 0)$ TA_2 phonon branch in NiMnGa is comparable to that in NiAl $(1/6 \ 1/6 \ 0)$, considering that the $L2_1$ unit cell is twice as large as the B2 unit cell.	
Tweed structure has been observed in the parent phase.	
Phonon energy shows slop change at T_C .	N/A
Below T_C , Phonon softening in NiMnGa is more pronounced than that of NiAl.	Phonon softening in NiAl is comparable to that of the paramagnetic phase of NiMnGa.
Commensurate phase exists above T_M in certain compositions, in which cases, up-turn of phonon energy of the soft mode occurs.	No intermediate phase present prior to MT. Soft mode phonon always keeps softening above T_M .
Phonon softening originates from e-ph coupling, and is enhanced by magnetoelastic coupling.	Phonon softening results from e-ph coupling
Minimum position of the $(\zeta, \zeta, 0)$ TA_2 branch is independent on temperature.	Minimum position of the $(\zeta, \zeta, 0)$ TA_2 branch is temperature dependent.
Both C' and C_{44} softens on cooling.	All elastic constants stiffens upon cooling except C'

Table 2.2 Comparison of precursor effects observed in ferromagnetic NiMnGa alloys and non-magnetic NiAl alloys.

a multi-variant state on cooling the material below T_M , which complicates the magnetic anisotropy analysis.

In chapter 3, we study the fundamental magnetic properties of a nonstoichiometric NiMnGa single crystal and investigate the magnetocrystalline anisotropy energy of the martensitic phase with the so-called singular point detection (SPD) method. It reveals the temperature dependence of magnetic driving force in martensitic NiMnGa and helps to understand the mechanism of MFIS in NiMnGa and other similar FSMAs.

In addition, precursor effects of NiMnGa, interesting from the scientific point of view, will be studied. While there have been extensive theoretical investigations on NiMnGa premartensite, experimental evidence testing those well established theories is less extensive. For one example, Landau model predicts a change in slope around T_C for the temperature dependence of C' , an indication of magnetoelastic coupling in NiMnGa alloys. However, no significant change in any of the moduli has been observed at the Curie point up to date. For another, in comparison to the study of structural transformations, the magnetic properties in austenitic NiMnGa were practically not investigated. With more and more manifestations of magnetoelastic coupling effects in NiMnGa, magnetic signatures of precursor phenomena are expected to occur.

Chapter 4 highlights the elastic and magnetic precursor phenomena in FSMA $\text{Ni}_{49.0}\text{Mn}_{23.5}\text{Ga}_{27.5}$ (wt%). The results confirm the premartensitic transformation at T_1 , illustrate its magnetoelastic character and demonstrate that the coexistence of a finite

magnetic susceptibility and that a vanishing magnetic anisotropy in the premartensitic state is the signature of the tweed.

Chapter 5 summarizes our contributions to understand the magnetoelastic coupling in NiMnGa FSMAs.

Chapter 3

Actuation Field in Martensitic $\text{Ni}_{49.0}\text{Mn}_{23.5}\text{Ga}_{27.5}$ Alloy

3.1 Introduction

Large magnetic field induced strains (MFIS) and high operating frequencies make magnetoelastic materials attractive candidates for transducers and actuators in which a large amount of energy is transferred between the magnetic and mechanical states. Among them, rare-earth magnetostrictive materials are capable of delivering strains of the order of 10^{-3} .^{150,151} This large magnetostriction is caused by a full 90° magnetic moment rotation with the external magnetic field. Therefore, magnetostrictive materials with low magnetic anisotropy are technically interesting because they only require small actuation field for operation. A well-known example is the $\text{Tb}_{0.3}\text{Dy}_{0.7}\text{Fe}_2$ alloy (Terfenol-D) that has achieved great commercial success.

NiMnGa FSMAs are now actively studied as a new class of magnetoelastic materials due to the super magnetic-field-induced strain they achieve (6% for 5-layered and 10% for 7-layered NiMnGa martensite). This super magnetostrain is obtained by the martensitic variants reorientation. Therefore, the material works fully within the low temperature martensitic phase. FSMAs are expected to be magnetically hard and elastically soft, i.e. high magnetic anisotropy and low blocking twinning stress are the two key requirements for NiMnGa martensite to obtain maximum strain under external magnetic field.

In this chapter, we report the effect of decreasing temperature on the profile of magnetization curves and indirectly the FSM effects in a $\text{Ni}_{49.0}\text{Mn}_{23.5}\text{Ga}_{27.5}$ (wt%)

crystal. The uniaxial magnetocrystalline anisotropy constant K_1 of the martensitic phase are calculated using the so-called singular point detection (SPD) method. The results indicate that the magnetic anisotropy increases with decreasing temperature and becomes saturated below 150 K. The calculated K_1 is in good agreement with published data and fits the magnetization power law well.

3.2 Experimental Procedures

3.2.1 Sample Information

A $\text{Ni}_{49.0}\text{Mn}_{23.5}\text{Ga}_{27.5}$ (wt%) single crystal was prepared by AdaptaMat OY, Finland. It undergoes an austenite-martensite transformation on cooling at $T_M = 276$ K and its Curie temperature T_C is located at 383 K. According to the neutron powder diffraction measurements, the $\text{Ni}_{49.0}\text{Mn}_{23.5}\text{Ga}_{27.5}$ austenite phase shows the typical cubic $L2_1$ structure, with $a=0.583$ nm at 413 K. Below T_M , at 227 K, the martensitic phase exhibits a characteristic pattern of a body centered tetragonal (bct) structure, with $c=0.559$ nm and $a=0.595$ nm ($c/a=0.94$), corresponding to the 5-layered modulated lattice reported before.¹⁵² Details of the neutron powder diffraction results will be shown in the next chapter. The sample information has been summarized in Table 3.1.

3.2.2 Experimental Methods

Very thin circular disks with diameter 3 mm and thickness 0.2 mm were cut with a wire electrical discharge machining (EDM) at room temperature. These disks were orientated with a (110) normal to contain $[001]$, $[110]$ and $[1\bar{1}1]$ directions in the plane so that the measuring magnetic field could be applied parallel to the circular

Composition	Ni _{49.0} Mn _{23.5} Ga _{27.5} (wt%)
Electron concentration (e/a)	7.56
Curie temperature (T _C)	383 K
Premartensitic transformation temperature (T _I)	333 K
MT temperature (T _M)	276 K
Martensitic structure	Tetragonal, c/a = 0.94
Density	8.1 g/cm ³
Maximum free strain	58 μm/mm at 0.5 T
Compressive strength	700 MPa
Resistivity	62×10 ⁻⁸ Ω m
Threshold field strength	250 kA/m
Maximum cycle energy density	90 kJ/m ³

Table 3.1 Sample information (PT temperatures, structures, e/a, etc.).

disk surface and aligned along the desired crystallographic directions. Magnetic measurements were carried out with a superconducting quantum interference device (SQUID) magnetometer. Prior to each M-H measurement, the specimen was heated above its Curie temperature and subsequently cooled down to the measuring temperature before applying magnetic field parallel to its cubic [001] crystallographic direction. It is well known that for SMAs, the strain energy associated with the martensitic transformation can be minimized by the self-accommodation of martensitic variants, i.e., the formation of martensitic variants in compatible crystallographic directions. Because the static equilibrium obtained by contacting twinned regions along their edges, the most probable direction of the short axes of the variants is along one of the three primary orthogonal axes of the cubic lattice of the untransformed single crystal. Hence, the specimen was initially in an equi-variant state, in which the three types of tetragonal variants are equally distributed along the primary orthogonal axes of the austenite cubic lattice. For simplicity, we call 1/3 of them the axial variants whose c axis is parallel to the field direction and the other 2/3 the transverse variants.

3.2.3 SPD Technique

With zero-field cooling below T_M , the martensitic phase represents to essentially a polycrystalline state composed of same volume fractions of the three tetragonal variants, which makes the determination of anisotropy constants difficult. Tickle and James overcome this difficulty by compressing their specimen into a single-variant state using an intricate fancy fixture at the measuring temperatures. Thus, M-H curves parallel and perpendicular to the compression axis can be

measured, respectively.¹⁵³ Here, we illustrate the use of the so-called single point detection technique to calculate the magnetic anisotropy constants based on the M-H curves of NiMnGa martensite in equi-variant state, which is easy to obtain, as described above. The SPD technique was originally applied to measure the magnetic anisotropy in polycrystalline materials. In principle, the magnetization curve for a single crystal with the field orientated in its hard direction has a knee at the anisotropy field, H_A , shown in Fig 3.1. The singularity is a consequence of the intersection of the two different branches of the magnetization curve. For $H < H_A$, M depends almost linearly on M , while as $H > H_A$, M reaches saturation magnetization, M_s , which is a constant. A smoother M-H curve is expected if the magnetic field is applied to a polycrystalline magnetic material. However, the singularity at $M(H_A)$ can still be detected by the peak of d^2M/dH^2 as a function of H . The amplitude of the peak should be proportional to the volume fraction of crystallites oriented with their easy axes perpendicular to H . The sharpness of the change of $M(H)$ at H_A depends on the distribution of hard axes, and the ratio of the first to second order anisotropy constants, according to G. Asti et al..¹⁵⁴

3.3 Results and Discussions

Temperature dependence of magnetization under field cooling and subsequent heating at 1 kOe field is shown in Fig. 3.2. Considerable magnetization changes clearly mark both the austenite-martensite transformation at $T_M=276$ K and the Curie transformation at 383 K. The martensitic transformation is completely reversible and displays a 7 K thermal hysteresis. The magnetization changes significantly during the martensitic phase transformation because the magnetic anisotropy of the martensite is

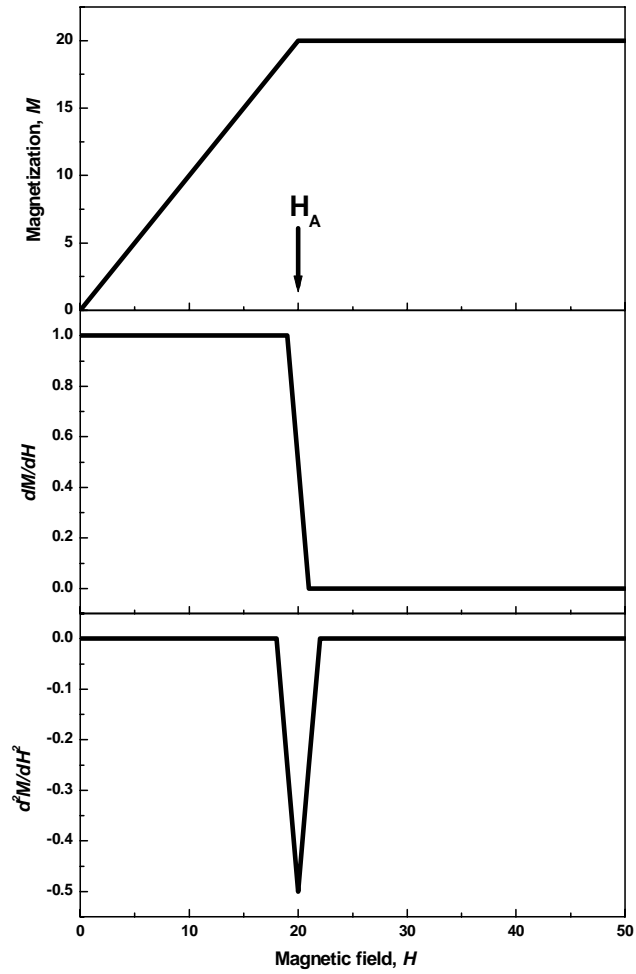


Fig. 3.1 Illustrating the SPD method to estimate the anisotropy field in materials. The dip in d^2M/dH^2 curve corresponds to the anisotropy field, H_A of the material.

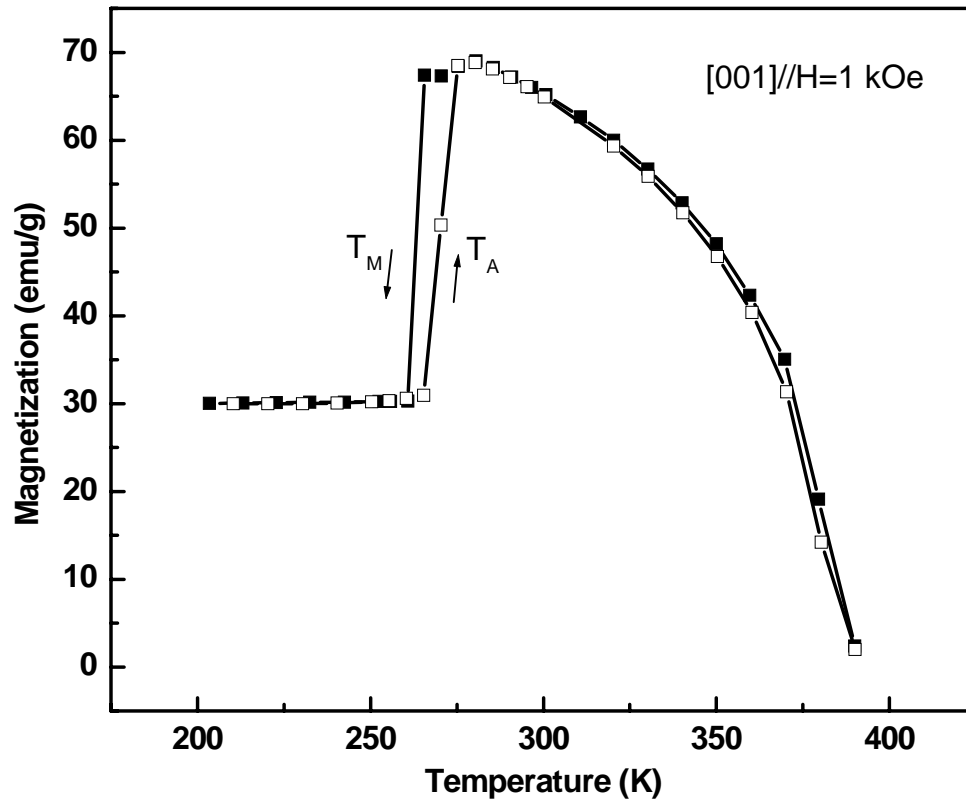


Fig. 3.2 Temperature dependence of magnetization of single crystal $\text{Ni}_{49.0}\text{Mn}_{23.5}\text{Ga}_{27.5}$ by field cooling and heating under 1 kOe. Field was aligned along the [001] crystallographic direction at room temperature.

about two orders of magnitude higher than that of the austenite. No further substantial structure change is observed down to 5 K.

A series of magnetization curves is measured at various temperatures below T_M by applying magnetic fields up to 2 T. These curves show a strong temperature variation, suggesting that different mechanisms for lowering the internal energy occurred during cooling.

When measured close to T_M , the magnetization curves display a jump of the magnetization, together with large hysteresis in the first quadrant, as shown in Fig. 3.3. This type of magnetization curves indicates the occurrence of magnetic field induced twin boundary motion, an unequivocal sign of a large MFIS. Typical magnetic behavior can be seen at 268 K. Magnetization first increases linearly with increasing the field, which suggests that the magnetization rotates off its easy axis. At 4 kOe, an abrupt increase in magnetization occurs. Afterwards, magnetization curve levels off. The event signifies that twin boundary motion is initiated at this moment and the rotational process is replaced by the structural rearrangement of martensitic twin variants. The twin boundary motion results in the growth of the existing favorable 1/3 axial variants at the expense of the other 2/3 transverse ones whose hard axes are aligned parallel to the field. At the end of the magnetization process, the reorientation of the transverse variants is complete and the specimen is in a nearly single variant state with magnetization vectors lying in the external field direction. Because the structural anisotropy within a tetragonal variant is large, this field induced variant reorientation produces large MFIS when the long axes of the initial variants become the short axes in the field direction. On the return path,

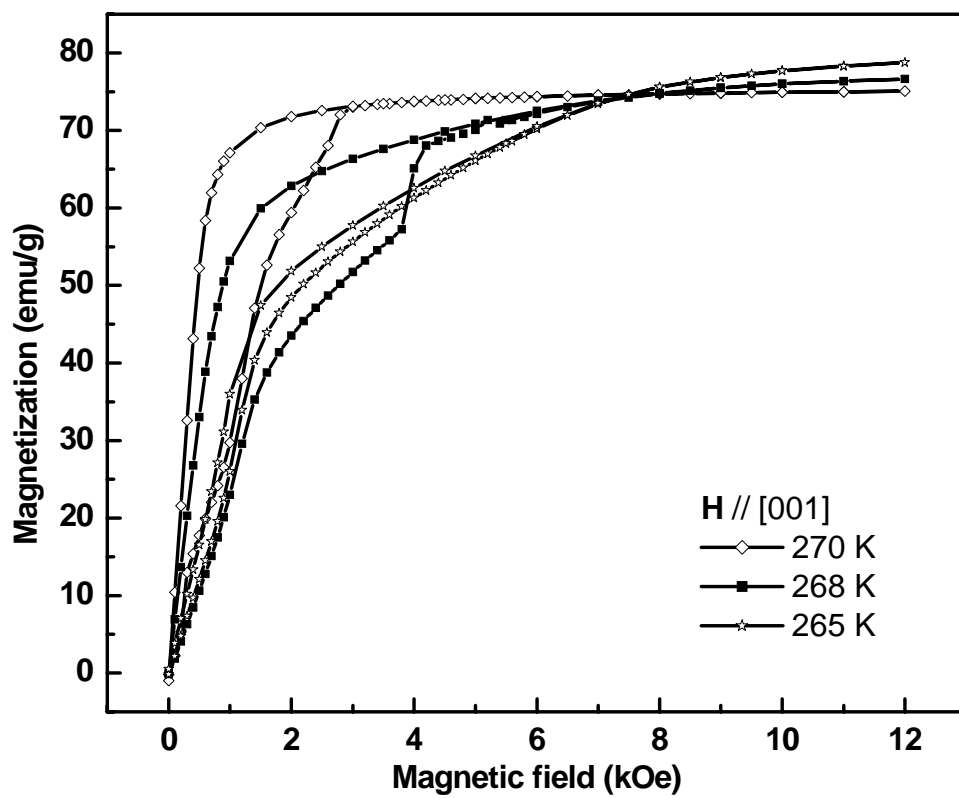


Fig. 3.3 Magnetization curves measured close to T_M . It demonstrates the occurrence of FSM effects with the large hysteresis observed at corresponding temperatures.

magnetization decreases slowly from the saturation value toward the low field, resulting in large transient hysteresis in the first quadrant. The area of the hysteresis represents the energy dissipated due to martensitic variants redistribution. All following magnetization cycles are square-like loops, indicating that the specimen stays in the single variant state with its easy axis parallel to the field direction. The material can be reactivated by subsequently applying magnetic field along two different perpendicular austenite cubic axes. Fig. 3.3 illustrates that the temperature range of variant redistribution is narrow. About 30 K below T_M , the hysteresis becomes indiscernible. This is in agreement with the fact that MFIS decreases with increasing distance from the martensitic transition, For example, Yu et al. reported that the MFIS decrease three times at 30 degree below T_M .¹⁵⁵ It should be noted that in all cases the specimen exhibits very small remanence magnetization and hysteresis, which demonstrates that the magnetization of the single variant takes on different orientations by breaking up into multiple 180° magnetic domains to minimize magnetostatic energy. As a result, the local average magnetization within the martensitic variants is variable and can be changed by a magnetic field. This reveals why early models failed to explain the maximum of magnetic driving force is limited and independent of the magnetic field. These models, assuming each variant as a single domain structure with a constant magnetization and constrained magnetic direction, predicted a linearly infinite increase of magnetic driving force with applying magnetic field.^{156,157}

Next, Fig. 3.4 shows several typical magnetization curves measured below 250 K with little hysteresis detected. It indicates that at low temperatures, martensitic variant

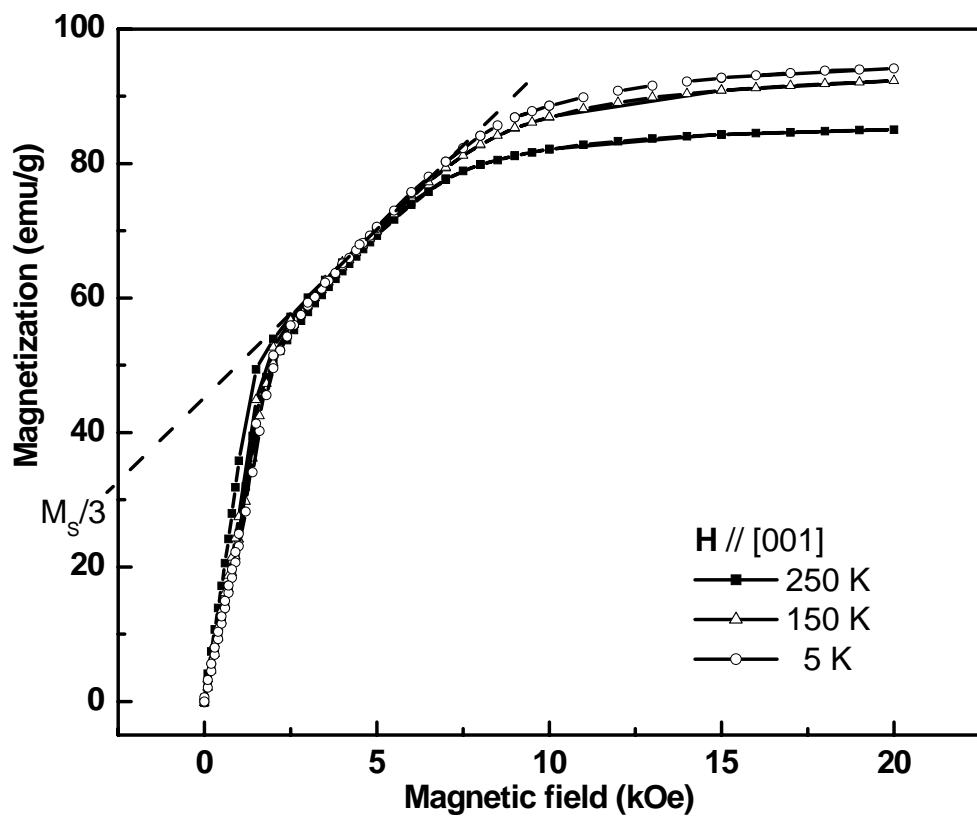


Fig. 3.4 Magnetization curves measured at 250 K, 150 K and 5K, characterized by the multiple slope changes with changing field.

reorientation is inhibited and magnetization rotation predominates the whole magnetization process. Magnetization curves are characterized by multiple distinct slope changes which are associated with the responses of different twin variants to the applied field. Three stages of magnetic process can be defined for all the magnetization curves measured in Fig. 3.4 and different mechanisms of magnetization along either easy or hard magnetic direction are accounted, respectively. In the first stage, the 1/3 axial variants are saturated by 180° magnetic domain walls motion in easy-axis bands, supported by the fact that after extrapolating the linear increase of magnetization of the broken-slope curves above 2 kOe external field, the interception of magnetization equals 1/3 of the final saturation magnetization. It confirms that the specimen is in an equi-variant state, in agreement with the study of fraction dependence of magnetization in NiMnGa alloys by A.A. Likhachev et al.. A relatively large magnetic field (around 1.2 kOe) required to saturate these favorable variants may be understood by considering the existence of internal obstacles, like the structural inhomogeneities due to the self-accommodation of different variants, acting as a pinning center for magnetization saturation. Next, magnetization of the other unfavorable transverse variants increases dramatically because of the applied external field and the internal mean field provided by the already aligned axial variants. In contrast to the magnetization mechanism in stage 1, the rotation of magnetic vectors in magnetic hard directions seems to be responsible for this slow increase of magnetization. Finally, the specimen approaches saturation with applying field above 1 T. Thus, no (or very small) reorientation of the martensitic variants has been observed when the specimen is magnetized below 250

K. Consequently, large field-induced strain associated with FSME is no longer expected.

As pointed out early, the modulated bct martensite has a uniaxial magnetic anisotropy, and its easy axis is along the short c crystallographic axis. Considering the Zeeman energy density and magnetic anisotropy energy density, the total energy density of the material can be written as:

$$E = -HM_s \cos \theta + K_1 \cos^2 \theta + K_2 \cos^4 \theta \quad (3.1)$$

where K_1 and K_2 are the first and second order of magnetic anisotropy constants, θ is the angle between the magnetization vectors and the c axis, and M_s is the saturation magnetization of the material. According to equation (3.1), the magnetization curve can be described by the following expression:

$$HM_s = [2K_1 + 4K_2(M/M_s)^2](M/M_s) \quad \text{for } H \leq H_A \quad (3.2)$$

where H_A is the anisotropy field. Qualitatively fitting the experimental data shown in figure 3.4 indicates that K_1 is positive and increases with decreasing temperature whereas K_2 is negative and changes very little on cooling. This is consistent with the fitting results based on the first-principles calculations made by J. Enkovaara et al., who also found that the absolute value of K_2 ($-0.3 \mu\text{eV}$) is much less than K_1 ($170 \mu\text{eV}$).¹⁵⁸

In order to investigate the mechanism of the MFIS in NiMnGa, it is critical to know the temperature dependence of the magnetic anisotropy. The non-zero magnetic driving force responsible for twin boundary motion are:

$$f_{mag}(h) = \int_0^h (m_a(h) - m_t(h)) dh \quad (3.3)$$

If the specimen is in its single variant state, the above magnetic driving force equals its magnetic anisotropy. However, with zero-field cooling below T_M , the martensitic phase is a polycrystalline domain state composed of equal volume fractions of the three tetragonal variants, rendering the determination of anisotropy constants difficult. The singular point detection (SPD) technique has been applied successfully to measure the magnetic anisotropy in polycrystalline materials and NiMnGa martensites of multi-variant state,¹⁵⁹ as well as in very small specimen in which easy and hard magnetization directions are difficult to be determined. As discussed early in this chapter, the anisotropy field, H_A , can be expressed as:¹⁶⁰

$$H_A = (2K_1 + 4K_2) / M_s \quad (3.4)$$

The singularity at H_A of the magnetization curves of a martensitic $\text{Ni}_{29.0}\text{Mn}_{23.5}\text{Ga}_{27.5}$ in Fig. 3.4 can still be observed by calculating the successive derivatives of M with respect to H . The SPD technique, which provides precise measurements of the anisotropy field, is thus a powerful tool to estimate the magnetic anisotropy constant K_1 at low temperatures where magnetization along easy and hard directions of the martensitic single variant is not easily measured simultaneously. Fig. 3.5 plots the first and second derivatives of field dependence of magnetization at various temperatures, based on the data of figure 3.4. The peak position in the first derivative of magnetization corresponds to the field to saturate the 1/3 axial variants. And the valley of the second derivative of magnetization reflects the anisotropy field H_A of the martensitic $\text{Ni}_{29.0}\text{Mn}_{23.5}\text{Ga}_{27.5}$. The anisotropy field increases with decreasing temperature and saturates below 150 K. According to equation (4), anisotropy constant K_1 can be calculated assuming that in uniaxial magnets, K_2 is negligible.

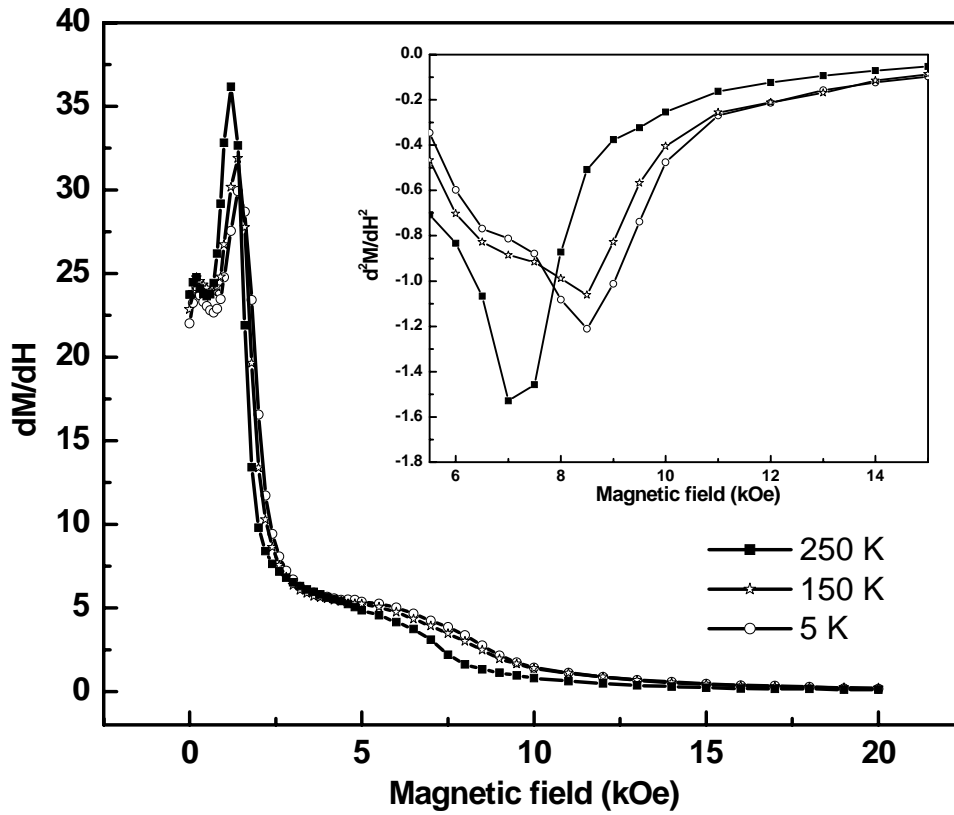


Fig. 3.5 First derivative of magnetization as a function of H at corresponding temperatures. Inset fig. shows the field dependence of second derivative of magnetization at corresponding temperatures.

Temperature dependence of K_1 is plotted in Fig. 3.6, together with the corresponding saturation magnetizations determined at temperatures below T_M . The calculated results of K_1 are comparable with the published data of $2.45 \times 10^5 \text{ J/m}^3$ measured in a single variant state by Tickle and James. Fitting the above data by the magnetization power law

$$K_1(T)/K_1(5\text{ K}) = [M_s(T)/M_s(5\text{ K})]^n \quad (3.5)$$

indicates that n is close to 3, which is expected for the uniaxial anisotropy of tetragonal martensite. The results are plotted in Fig. 3.7.

It is reported that the temperature dependence of the blocking stress has an exponential-like character and the energy necessary to move the twin boundaries increases faster than the magnetic anisotropy energy during cooling.¹⁶¹ Therefore, an ever increasing magnetic field is needed to move the twin boundaries, and eventually, it becomes impractical. For the present non-stoichiometric $\text{Ni}_{49.0}\text{Mn}_{23.5}\text{Ga}_{27.5}$ specimen, magnetic driving force is higher than the blocking stress between T_M and 250 K. Although the 180° magnetic domain wall motion occurs within each martensitic, the magnetic vectors stay in their magnetic easy direction. Instead, abrupt reorientation of martensitic variants takes place, which gives rise to the large MFIS in FSMAs. However, below 250 K, the blocking stress starts to overcome the magnetic driving force. Then, the application of an external field results in the rotation of the magnetization vectors in unfavorable martensitic variants. Upon saturation, the Zeeman energy is the same in neighboring martensitic variants, therefore it is unlikely for the observed field-induced strains are associated with twin boundary motion. Hence, FSM effects are suppressed and only the typical magnetostriction strain can

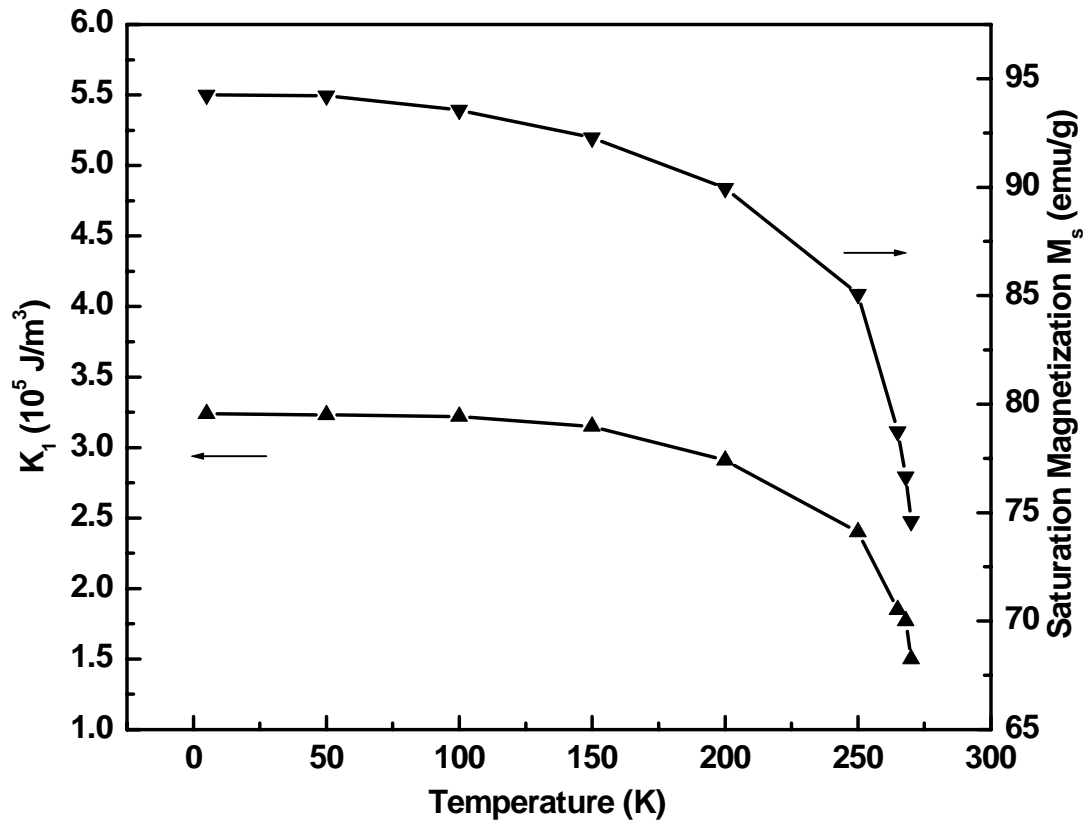


Fig. 3.6 Temperature dependence of saturation magnetization and magnetic anisotropy constant K_1 of martensitic $\text{Ni}_{49.0}\text{Mn}_{23.5}\text{Ga}_{27.5}$.

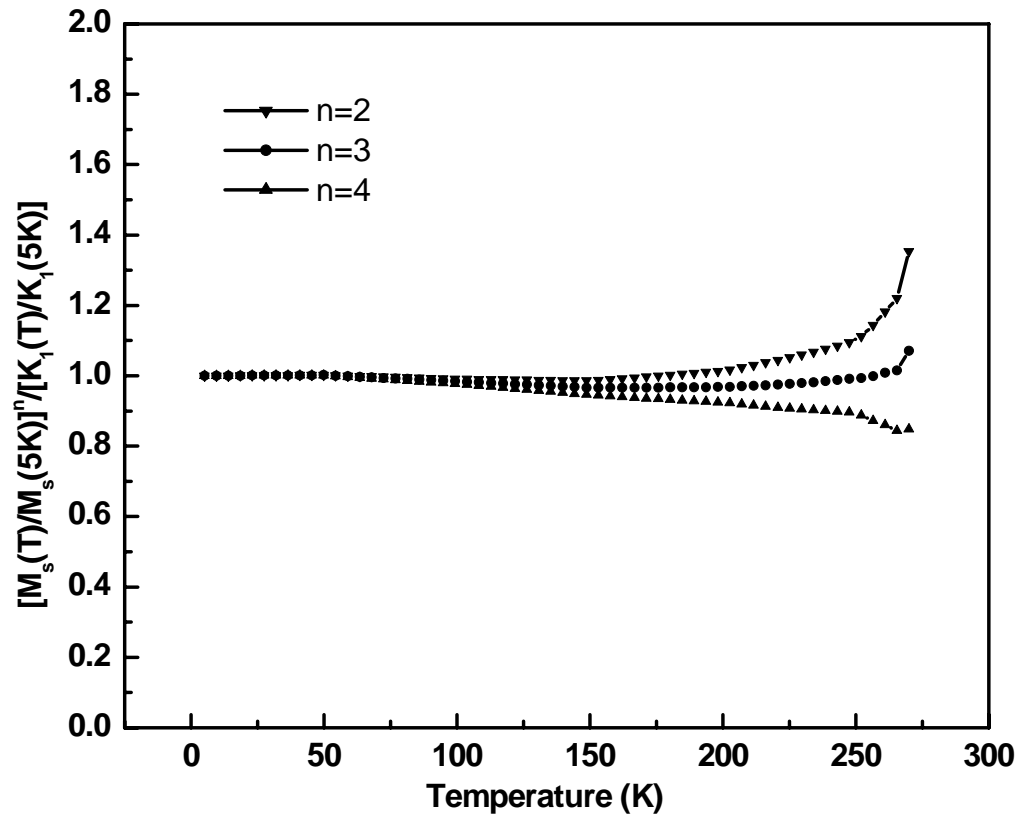


Fig. 3.7 Dependence of normalized K_1/M_s^n for $n=2, 3$ and 4 .

be found. The mechanism of MFIS has been plotted in Fig. 3.8. The difference between the magnetostrain in FSMAs (with high magnetic anisotropy) and magnetostrictive materials (with low magnetic anisotropy) has been summarized in Table 3.2.

It is reasonable that when the martensitic SMA is in its multi-variant state, the existence of additional twin boundaries can inhibit the growth of the existing residual variants and thus strongly increase the blocking stress on twin boundaries. The material is necessary to be prestressed to bias a single variant state and operate by applying a competing variable magnetic field to induce shape change. This strategy has significant technological implications because it will improve the MFIS both by expanding the temperature window of field-induced martensitic variant redistribution, and by achieving maximum strain response in the external magnetic field as well. To facilitate this mode of operation and to study the temperature dependence of magnetic properties in NiMnGa crystals, the application of SPD technique is advantageous because the specimen can be used in its equi-variant state, which is technically easy to obtain. The temperature dependence of magnetic anisotropy can be precisely determined, and this result shines a light on the mechanism of the MFIS after realizing the connection between the fundamental magnetic properties and the magnetic driving force in FSMAs.

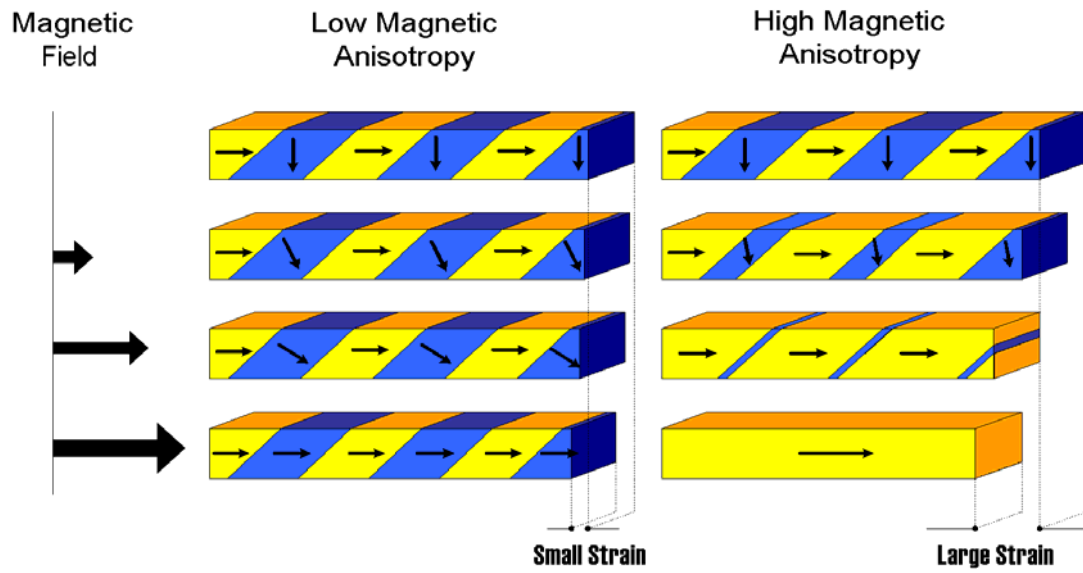


Fig. 3.8 Mechanism of martensitic variant redistribution under magnetic field (for simplicity, the variant is drawn to be in single magnetic domain structure, which is not true in reality).

FSMAs	Magnetostrictive Materials
Super field-induced strain is due to twin-boundary motion. The strain is tied to the crystallography, not the direction of M.	Field-induced strain is a result of magnetization rotation to the crystallography; The strain is tied to M, not the lattice.
The strain turns on in the low-temperature martensitic phase by a 1 st order structural transformation below T_M .	Magnetostrictive strain turns on below T_C with a 2 nd order magnetic transformation. It has a temperature dependence governed by $[M(T)/M(0)]^{l(l+1)/2}$.
The field-induced strains decrease as the strength of the magnetocrystalline anisotropy of the martensitic phase decreases below $M_s H$.	The smaller the anisotropy, the greater the strain accessible in a given field $H < H_a$.
The field-induced strain in finely twinned FSMAs is linear in H below saturation in the strong anisotropy limit.	The field-dependence of magnetostrictive strains in a hard-axis magnetization process is quadratic in H or M.
For demagnetized, equi-twin variant state, the strain is direction perpendicular to the field will be $\epsilon_{\text{perpen}} \approx \epsilon_{\text{parall}}/2$, where ϵ_{parall} is the field-induced strain parallel to the field.	

Table 3.2 Difference of magnetic-field-induced strains between FSMAs and magnetostrictive materials, after O' Handley et al..

Chapter 4

Elastic and Magnetic Properties of

$\text{Ni}_{49.0}\text{Mn}_{23.5}\text{Ga}_{27.5}$ Premartensite

4.1 Introduction

The stability of magnetic and crystal structure is very sensitive to the electron concentration in NiMnGa alloys. Among them, the sequence of phase transformation of NiMnGa alloys in group I, introduced in chapter 2, received extensive attention due to the rich variety of physical anomalies associated with the precursor effects prior to the MT. The proposed frame work of the transformation path of austenite \rightarrow incommensurate phase (tweed) \rightarrow commensurate phase (premartensite) \rightarrow martensite has been confirmed by the observation of austenite, tweed and martensite by TEM and new modulated premartensite by inelastic neutron scattering and elastic constants measurements.

In this chapter, we present our experimental data to show both the elastic and magnetic anomalies closely related to the premartensitic transformation in $\text{Ni}_{49.0}\text{Mn}_{23.5}\text{Ga}_{27.5}$ (wt%). The magnetoelastic strain corresponding to the elastic constant C_{44} has been isolated, undoubted demonstrating the magnetoelastic condensation at T_1 . The slope change of C' at T_C , reported here for the first time, provides strong evidence of magnetoelastic coupling which enhances the premartensitic transformation in NiMnGa alloys. More important, a magnetic anomaly consisting of the coexistence of a finite magnetic susceptibility and a

vanishing magnetic anisotropy in premartensitic state, which is believed to be the signature of the tweed present above T_I , will be discussed.

4.2 Experimental Procedures

4.2.1 Sample Information

The specimen with the same composition as the one used in chapter 3 is investigated here. Sample information can be found in table 3.1 in the previous chapter.

4.2.2 High-resolution of Neutron Powder Diffraction

Powder neutron diffraction data were collected at various temperatures between 227 K and 413 K using the high resolution BT-1 32 detector neutron powder diffractometer at the NIST Center for Neutron Research. A Cu(311) monochromator with a 90° take-off angle, $\lambda=1.5403(2)$ Å, and in-pile collimation of $15'$ (minutes of arc) were used. A powder sample was sealed in a vanadium container inside a dry He-filled glovebox and a top loading closed cycle refrigerator (CCR) was used for temperature control. Diffraction data at each temperature were collected over the ranges of 3° to $168^\circ 2\theta$ with a step size of 0.05° for approximately 4 hours. The layout of the BT-1 instrument has been drawn in Fig. 4.1.

4.2.3 Elastic Measurement

The ultrasonic continuous-wave method (UCWM) was used to determine the velocities of C_{44} elastic waves of a single crystal specimen vibrating in the hundred kHz range. A magnetic field of 6.4×10^2 kA/m was applied during the measurement to saturate the specimen. Commercially available lead zirconic titanate based 1.5 MHz pressure and shear transducers generated and detected the desired standing waves. A

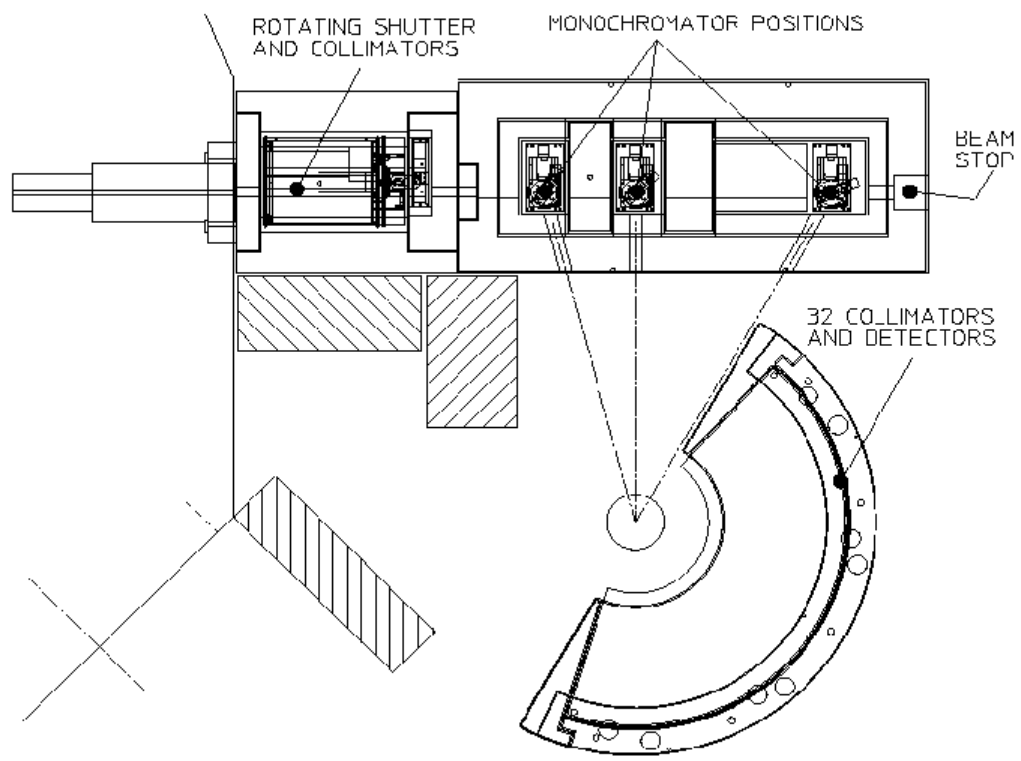


Fig. 4.1 Lay-out of BT-1 high-resolution neutron powder diffractometer.

thin layer of vacuum grease was applied between the sample and the transducers. The 2 mm thick rubber bands were fitted in the spaces between the transducers and sample. When the magnetic field is applied, two different field orientations were used, [001] and [100].

There are five modes with H along [001] and six modes with H [100] available to determine the elastic wave propagation, according to the sample's orientation and the elastic wave propagation (W) and the polarization (P) directions.¹⁶² Waves propagating in [110] with $[1\bar{1}0]$ polarization directly determines C' with [001] H and C^* with [100] H, shown in table 4.1. The detailed experimental set up can be found in elsewhere¹⁶³ and the layout of the experimental setup is shown in Fig. 4.2. The evolution of the internal friction (IF) and elastic constant C' during heating and cooling were studied by a cantilever oscillation measurement (COM) apparatus, which permits the simultaneous measurement of damping, modulus, and cantilever displacement on heating and cooling. This apparatus has been previously described,^{164,165} and the measuring methods has been depicted in Fig.4.3. It should be noted that the relative change of C' was measured at a frequency of at most kHz by COM, much lower than the frequencies utilized by the UCWM.

4.2.4 Magnetic measurement

To perform the magnetic measurements, very thin circular disks with a diameter of 3 mm and a thickness 0.3 mm were cut with a wire electrical discharge machining (EDM) at room temperature so that the demagnetization factor is close to 1. The disks were oriented with a (110) normal to contain [001], [110] and $[1\bar{1}1]$ directions in the plane and so that the measuring magnetic field could be applied parallel to the

\hat{H}	\hat{P}	\hat{W}	$C = \rho V^2$
[100]	[1 $\bar{1}$ 0]	[110]	$C^* = (a + c)^{-1}[c_{c_{44}} + a(C_{33} - C_{44} - C_{13})]$
[001]	[1 $\bar{1}$ 0]	[110]	$C' = (C_{11} - C_{12})/2$

Table 4.1 Elastic wave modes for C^* and C' . $a=C_{11}-2C_{44}-C_{13}$, $b=C_{11}-2C_{66}-C_{12}$, $c=C_{33}-2C_{44}-C_{12}$.

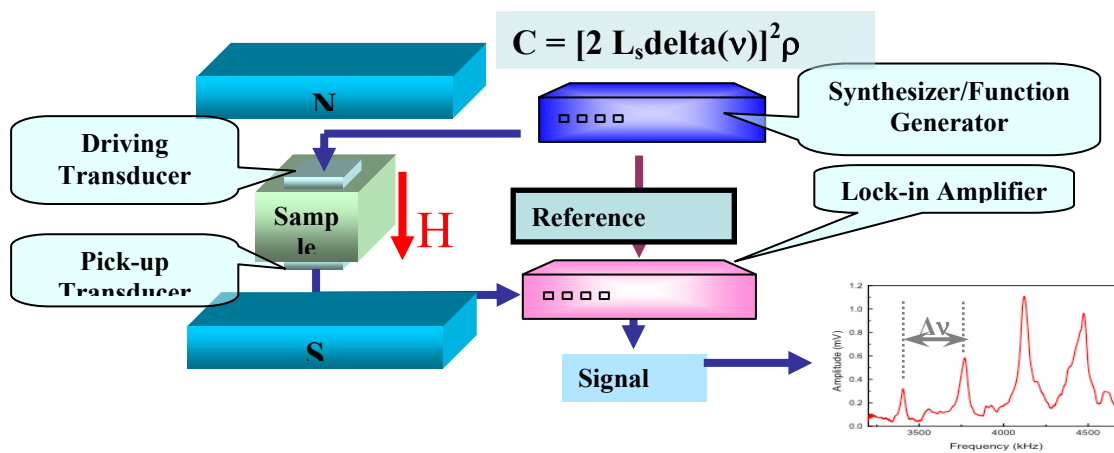


Fig. 4.2 Experimental setup of the ultrasonic continuous-wave method.

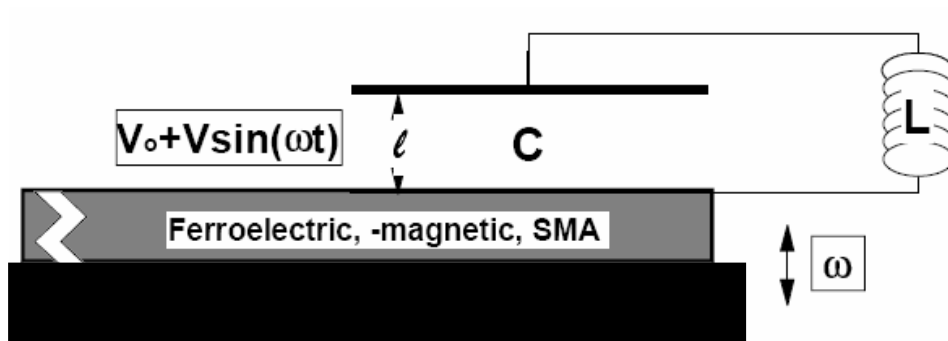


Fig. 4.3 Experimental setup of the cantilever oscillation method.

circular disk surface and aligned along the desired crystallographic directions. Magnetic measurements were carried out with a superconducting quantum interference device (SQUID) magnetometer. Prior to each measurement, the specimen was heated above its Curie temperature to ensure that each measurement corresponds to the first magnetization process.

4.3 Results and Discussions

4.3.1 Crystal structures

Crystal structures at various temperatures as determined by high-resolution neutron powder diffraction are shown in figure 4.4. At 413 K, $\text{Ni}_{49.0}\text{Mn}_{23.5}\text{Ga}_{27.5}$ is in the paramagnetic state. All the Bragg peaks observed could be indexed on a fcc $L2_1$ Heusler lattice with lattice parameter $a_c=5.83 \text{ \AA}$ (space group: $Fm\bar{3}m$). On cooling to 313 K, no additional peak appeared except that the increase of the [200] Bragg intensity confirms the establishment of the ferromagnetic ordering. However, pronounced intensity increases were observed at 2θ positions close to the potential peaks of the low temperature martensitic phase. The intensity increases indicate the appearance of an intermediate phase, reflecting that the material prepares for the martensitic transformation before it actually occurs. Upon cooling the specimen to 227 K, some of the original fcc diffraction peaks split, demonstrating that the material has transformed into a martensitic tetragonal structure (space group: $I4/mmm$). The refined lattice parameters of the tetragonal unit cell are $a_t=4.205 \text{ \AA}$, $c_t=5.585 \text{ \AA}$ ($c_t/a_t=1.33$). In order to compare them with the parent phase, the tetragonal structure is referenced to the $L2_1$ cubic coordinates in which case the new lattice parameters are $a_t=5.947 \text{ \AA}$ and $c_t=5.585 \text{ \AA}$ ($c_t/a_t=0.94$). Hence, the lattice distortion due to MT is

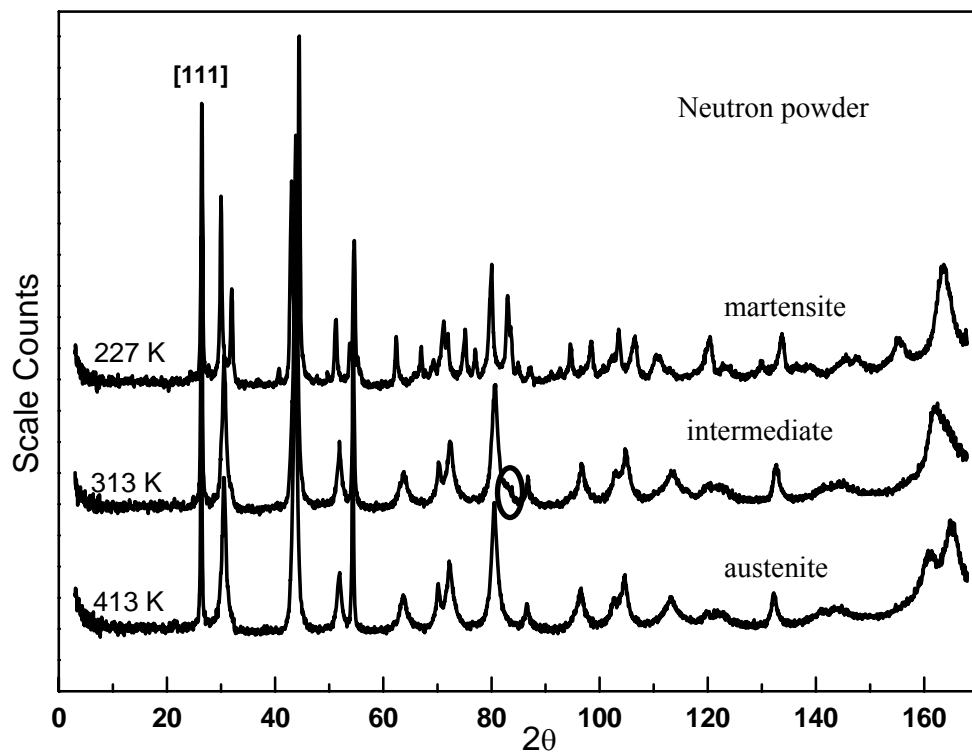


Fig. 4.4 Neutron powder diffraction patterns of $\text{Ni}_{49.0}\text{Mn}_{23.5}\text{Ga}_{27.5}$ at 413 K (parent phase), 313 K (premartensitic phase) and 227 K (martensitic phase), respectively.

about 6.1%. This tetragonal structure corresponds to the 5-layer modulated martensitic structure reported before.

Above T_M , small crystallite size and microstrain contribute to the peak broadening in all the diffraction data measured. Peak broadening stems from several sources, such as instrumental effects, finite crystallite size, strain and extended defects. We count the first three factors as the main reason for peak broadening observed in the neutron diffraction spectrum measured above T_M . It should be noted that the crystallite size is a measure of the size of a coherently diffracting domain, not generally the same thing as particle size. Here, we correct the instrumental effects for the Lorentzian peak shape:

$$\beta_{obs} - \beta_{inst} = \beta_{size} + \beta_{strain} \quad (4.1)$$

The contribution of small crystallite size can be assessed using by the so-called “Scherrer Formula”:

$$D_v = \frac{K\lambda}{\beta \cos \theta} \quad (4.2)$$

where D_v is the crystallite size; K is the Scherrer constant and is assumed to be 1; λ is the wavelength of the radiation and β is the integral breadth of a reflection (in radians) located at 2θ . Equation 4.2 was derived by Scherrer (1918), who was the first to observe that small crystallite size could give rise to line broadening. Although no broadening is associated with uniform strain, non-uniform strain leading to systematic shifts of atoms from their ideal positions in NiMnGa alloys will eventually result in peak broadening. This effect, first found by Stokes and Wilson (1944), was described by the following equation:

$$\varepsilon_{str} = \frac{\beta}{4 \tan \theta} \quad (4.3)$$

where ε_{str} is the average strain in the material. Note that crystallite size and strain broadening show a different θ dependence, which provides a way to separate these two effects. In this thesis, we applied the method proposed by Williamson and Hall (1953) to estimate size and strain broadening by analyzing the peak width (Full Width at Half Maximum, FWHM) as a function of 2θ . The W-H relationship for the Lorentzian peak shape can be expressed as:

$$(\beta_{obs} - \beta_{inst}) \cos \theta = \frac{\lambda}{D_v} + \frac{4\varepsilon_{str}}{\sin \theta} \quad (4.4)$$

The above expression indicates that if we plot $(\beta_{obs}-\beta_{inst})\cos\theta$ as a function of $4\sin\theta$, we can extract the crystallite size from the y-intercept and the strain from the slope of a linear fit to the experimental data. The fitting of the neutron diffraction peaks of (200) and (422) measured at 301 K has been shown in Fig. 4.5 and Fig. 4.6, respectively, to illustrate this idea. The fitting results show the FWHM (in this case, FWHM represents β in the above equations) of the cubic (200) and (422) peaks are 0.728° and 1.003° , much larger than the instrumental resolution for the corresponding 2θ s. Applying the fitting results of the broadening peak width into the W-H relationship of equation 4.4, the observed crystallite size in $\text{Ni}_{49.0}\text{Mn}_{23.5}\text{Ga}_{27.5}$ varies between 13 nm and 15 nm, close to the coherence length of tweed. The calculated microstrain of the cubic lattice varies from 0.28% to 0.49%. Detailed analysis of peak broadening has been discussed by Cullity,¹⁶⁶ Jenkin and Snyder.¹⁶⁷

4.3.2 Elastic anomalies

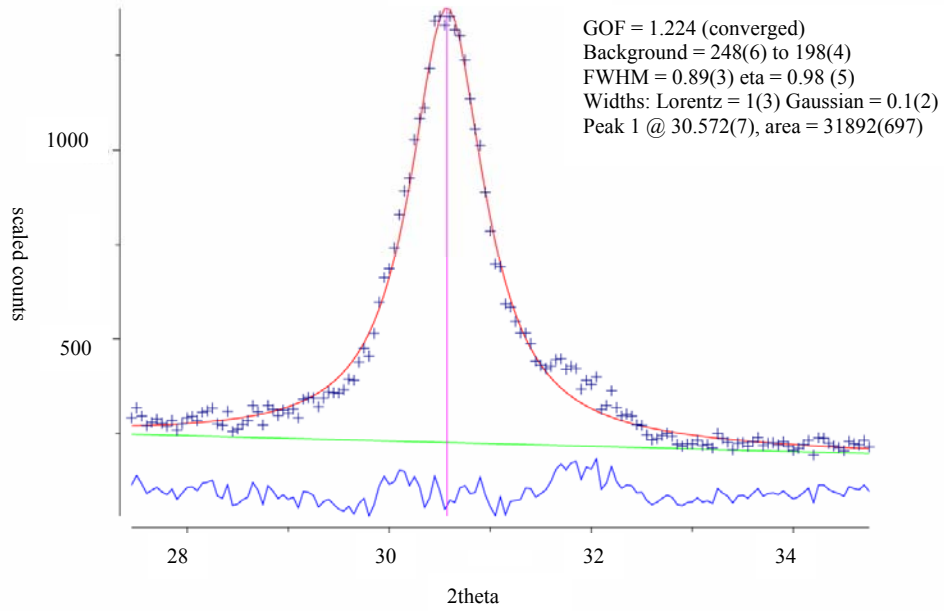


Fig. 4.5 (200) neutron peak broadening measured at 301 K for NiMnGa cubic structure.

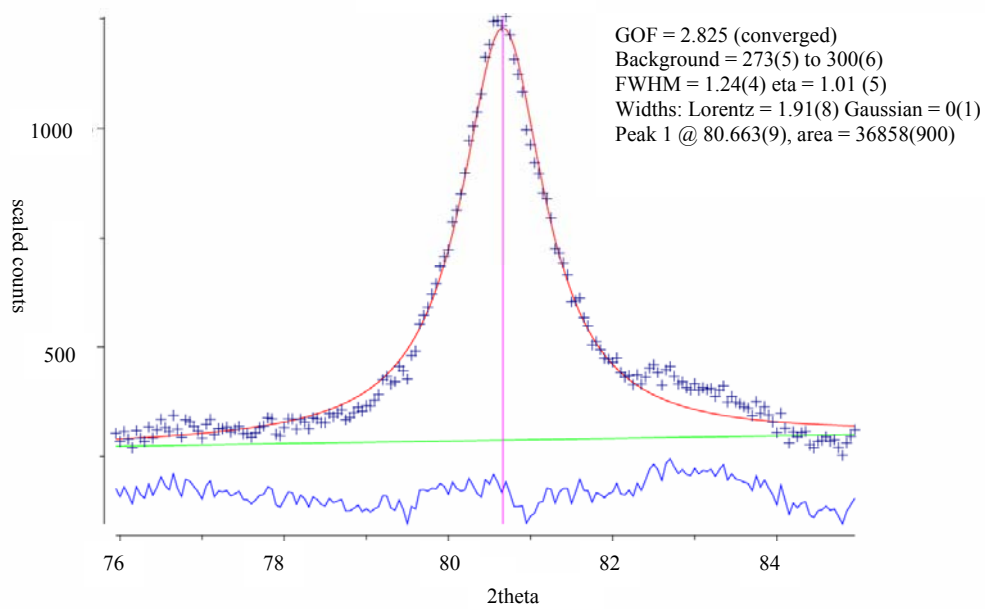


Fig. 4.6 (422) neutron peak broadening measured at 301 K for NiMnGa cubic structure.

Considering the internal strain that develops on cooling in NiMnGa, it is important to understand the elastic behavior in the vicinity of the phase transformations, because it provides insight into the nature of the transition. The high frequency elastic constant C_{44} measured by UCWM clearly demonstrates the presence of a commensurate, modulated phase on cooling between T_I and T_M , as illustrated in Fig. 4.7. Without applying an external magnetic field the high frequency C_{44} exhibits a linear softening between T_C and T_I (around 333 K). With further cooling below T_I , C_{44} stiffens as seen in curve (i). The up-turn at T_I reflects that, close to the T_M , the commensurate phase is more stable than the parent phase. For other compositions of NiMnGa, a similar tendency of the phonon frequency as a function of temperature was reported. The unique feature of the softening and subsequent hardening of both the relevant elastic constants and phonon frequency must be attributed to the combination of their magnetic and martensitic nature. Curve (ii) was measured in the same way except that a 8 kOe magnetic field was applied to the sample. Below T_C , the temperature dependence of the high frequency C_{44} of the magnetically saturated specimen varies completely opposite to the anomalies of the specimen in its non-magnetized state. C_{44} keeps increasing between T_C and T_I , leading to the classical ΔE effect. Specifically, once the spin system in the specimen is aligned by the external field, no magnetoelastic strain but only pure elastic strain can be detected with changing temperature. The magnetoelastic strain ϵ_{me} , (actually the ratio ϵ_{me}/σ at constant measuring stress σ) can be numerically calculated from the difference of C_{44} measured with and without magnetic field, curves (i) and (ii), and plotted in Fig. 4.8. It is not surprising to see that ϵ_{me} equals zero above T_C because the material is then in

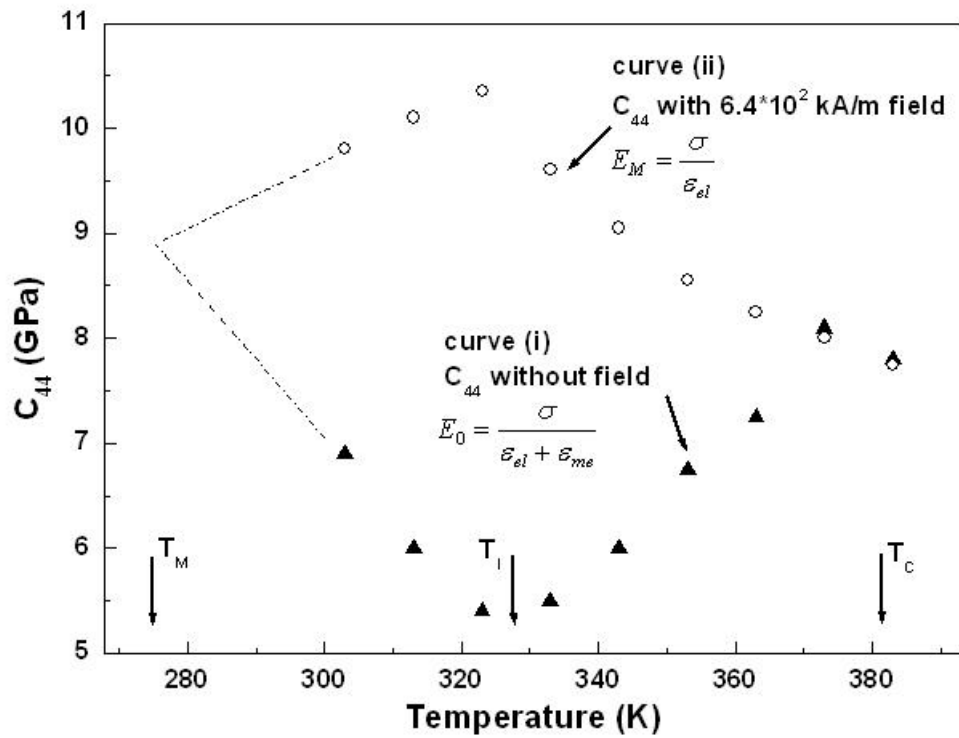


Fig. 4.7 Temperature dependence of the elastic constant C_{44} : (i) high frequency C_{44} measured without applying external magnetic field; (ii) high frequency C_{44} with 0.8 T magnetic field applied.

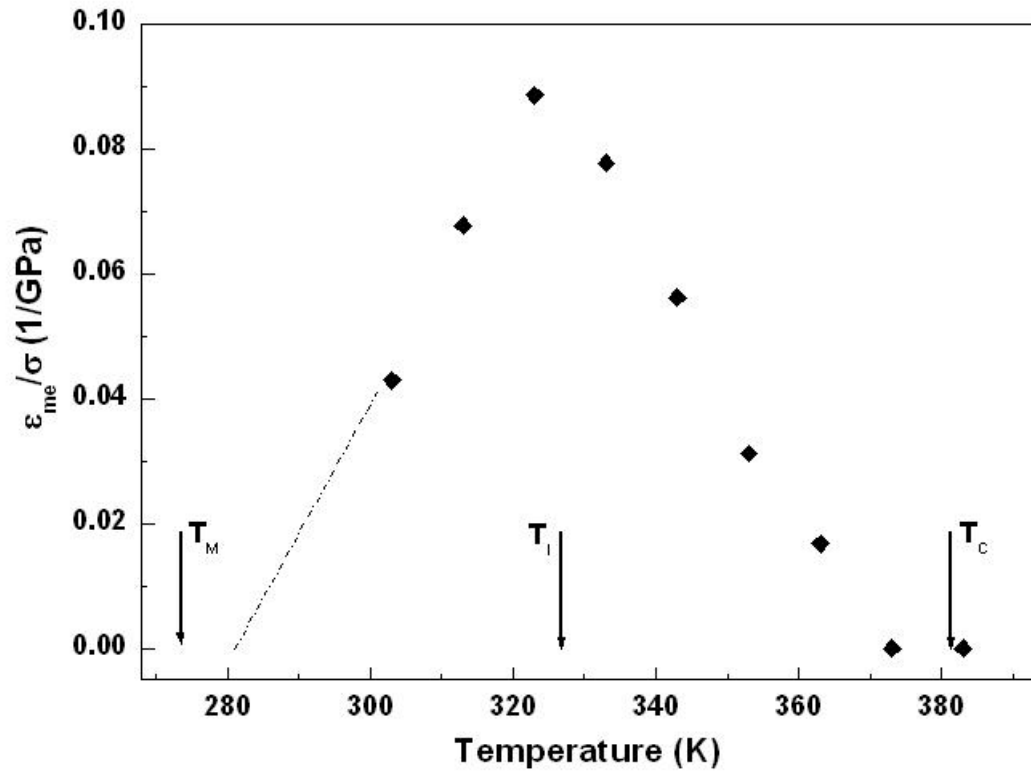


Fig. 4.8 Calculated ϵ_{me}/σ as a function of temperature.

its paramagnetic state. However, from the linear extension of the data in figure 4.8, it seems that ϵ_{me} approaches zero upon cooling the material to T_M as well. The magnetoelastic strain exhibits a maximum at T_I , providing clear evidence of a magnetoelastic condensation at the incommensurate/commensurate phase transition in agreement with the phonon condensation observed by neutron diffraction before. After the formation of the commensurate phase in the magnetically saturated specimen, C_{44} decreases with further cooling below T_I . This softening behavior is not fully understood yet.

The elastic constant C' is another important parameter to monitor the precursor phenomena in NiMnGa because it is associated with a weak restoring shear of the $\{110\}$ planes in the $\langle 1\bar{1}0 \rangle$ directions in the cubic lattice. Figure 4.9 displays the evolution of the low frequency C' and internal friction with cooling and heating above T_M measured by COM. The relative change of this low frequency C' decreases in several linear regimes starting in the high temperature phases, reflecting the increase of the lattice softening. Within the measuring temperature range, changes of slope only take place at temperatures corresponding to T_C and T_I . The coincidence of the Curie temperature and the temperature of the first kink during cooling suggests that the phonon softening depends on the magnetic ordering in the sample. It unambiguously affirms that the magnetoelastic coupling plays an important role in the premartensitic transformation and provides direct evidence to support the model predicting the multi-stage structural transformation by T. Castán et al.. Above T_C , magnetoelastic coupling can be understood by the direct interaction between the short-range magnetic fluctuations and the soft phonon potential in the paramagnetic

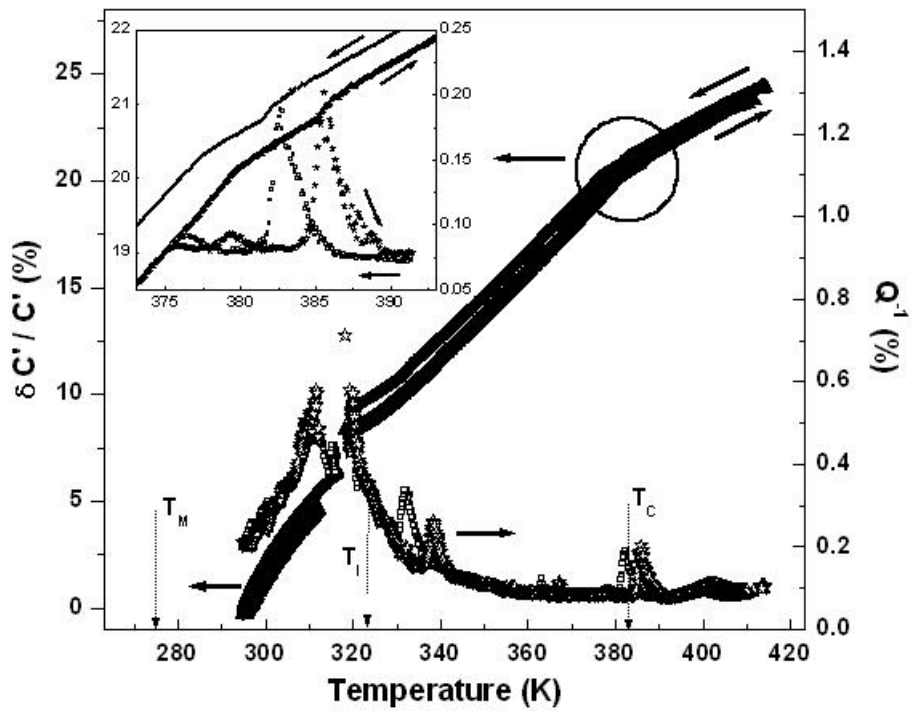


Fig. 4.9 Evolution of the low frequency C' and internal friction (IF) as a function of temperature (with cooling and subsequent heating).

parent state. The degree of phonon softening is enhanced after the material becomes ferromagnetic below T_C , where the spin system couples to the ionic displacement, producing the magnon-phonon interaction. In addition, both the IF peak and the C' kink observed at T_C show a temperature hysteresis, magnified in the inserted sketch of figure 4.9. Hence, the transition is not a usual 2nd order one. Instead, it is expected to be a magnetic and elastic transition, which is weakly 1st order. It has been proposed that an incommensurate phase precedes the pre-martensitic phase transformation.¹⁴ Therefore it appears reasonable to assume that the weakly 1st order nature of the Curie transition reflects the entry into the incommensurate phase. A second kink of the low frequency C' was detected upon further cooling the specimen to T_1 where C' exhibits a discontinuity and a concurrent maximum of the IF. It has been pointed out that the commensurate phase exists in a cubic lattice whose lattice parameter is three times larger than the parent phase. The maximum of the IF could result from new domain boundaries forming in the commensurate phase.

4.3.3 Landau models

A few Landau models for the premartensitic transformation in NiMnGa have been proposed.¹⁵ Realizing that the wiggle of the TA_2 phonon branch can still be seen above the Curie temperature, the phonon softening is attributed to the electron-phonon coupling and specific nesting properties of the Fermi surface, similar to the non-magnetic NiAl alloys. Focusing on the $\bar{q} = [\zeta\zeta 0]$ projection of the cubic to tetragonal distortion, the simplest Landau free-energy expansion is:

$$F(\eta, \varepsilon) = \frac{1}{2} \mu \omega^2 \eta^2 + \frac{1}{4} \beta \eta^4 + \frac{1}{6} \gamma \eta^6 \dots + \frac{1}{2} C' \varepsilon^2 + \dots + k_{\eta\varepsilon} \varepsilon \eta^2 \quad (4.5)$$

where ε is the tetragonal strain; η is the amplitude of the anomalous phonon; $\omega^2 = \alpha(T-T_0)$ is the square of the anomalous phonon frequency; C' is the elastic constant and $k_{\eta\varepsilon}$ is a material dependent parameter denoting the symmetry allowed coupling between strain and shuffle. Other coefficients are all positive constants. By eliminating the local tetragonal strain ε , an effective free-energy can be written in terms of the shuffle η only:

$$F(\tilde{\eta}) = \frac{1}{2}\mu\omega^2\tilde{\eta}^2 + \frac{1}{4}\tilde{\beta}\tilde{\eta}^4 + \frac{1}{6}\gamma\tilde{\eta}^6 \quad (4.6)$$

where the renormalized coefficient

$$\tilde{\beta} = \beta - \frac{2k_{\varepsilon\eta}^2}{C'} \quad (4.7)$$

The associated tetragonal distortion involved along the transformation path is

$$\varepsilon = -\left(\frac{k_{\eta\varepsilon}}{C'}\right)\eta^2 \quad (4.8)$$

The coupling between the two strains thus makes it possible for $\tilde{\beta}$ to be negative and hence leads to a first order transition at T_1 before the complete soft-mode condensation at T_0 .

Next, because the phonon softening is more pronounced in NiMnGa than that in NiAl, the role of the magnetism should be considered. We study the phase transformations in NiMnGa in terms of a Landau expansion of the only most relevant strain and magnetization variables, including nonuniform strains or modulations. Considering the magnetoelastic coupling between M , the magnetization (treated as a scalar here) and η , a plane modulation strain, and between M and ε , a $(110)[1\bar{1}0]$ homogeneous shear strain, the free energy can be expressed by:

$$F_{general}(\eta, \varepsilon, M) = F_{shuffle}(\eta) + F_{shear}(\varepsilon) + F_{magnetization}(M) + F_{me}(\eta, \varepsilon, M) \quad (4.9)$$

where

$$\begin{aligned} F_{shuffle}(\eta) &= \frac{1}{2}\mu\omega^2\eta^2 + \frac{1}{4}\beta\eta^4 + \frac{1}{6}\gamma\eta^6 \\ F_{shear}(\varepsilon) &= \frac{1}{2}C'\varepsilon^2 \\ F_{mag}(M) &\approx A(M - M_0)^2 \\ F_{me} &= \frac{1}{2}k_1M^2\eta^2 + \frac{1}{2}k_2M^2\varepsilon^2 \end{aligned} \quad (4.10)$$

Again, in equations (4.10), ω represents the frequency of the soft mode transverse phonon at wave vector $\langle 1/3, 1/3, 0 \rangle$ and $C'=(C_{11}-C_{12})/2$. Both quantities are temperature dependent. Following Planes et al., the purely magnetic energy expression F_{mag} can be linearized around a value M_0 above T_1 , where M_0 denotes the equilibrium magnetization close to the premartensitic transformation. The coupling between η and ε has been excluded now, because it is supposed to be negligible in comparison with the magnetoelastic coupling. All coefficients in the above energy expressions are positive constants.

Minimization of equation (1) with respect to M and ε leads to an effective free energy $F_{eff}(\eta)$ dependent on η alone:

$$F_{general}(\eta, \varepsilon, M) = F_{eff}(\eta) = \frac{1}{2}\mu\tilde{\omega}^2\eta^2 + \frac{1}{4}\tilde{\beta}\eta^4 + \frac{1}{6}\tilde{\gamma}\eta^6 \quad (4.11)$$

where

$$\tilde{\beta} = \beta - \frac{k_1^2 M_0^2}{A} \quad (4.12)$$

together with a given transformation path

$$\varepsilon = 0$$

$$M = \frac{M_0}{1 + \frac{k_1}{2A}\eta^2} \quad (4.13)$$

It can thus be seen that the strong coupling between M and η leads to $\tilde{\beta} < 0$ in which case a first order transition will occur. The elastic anomalies of Ni_{49.0}Mn_{23.5}Ga_{27.5} alloy measured close to T_I confirm such a weakly 1st order transition predicted by the above model.

More interestingly, considering the influence of the magnetism, the soft phonon frequency is formally given by:

$$\omega^2 = a(T - T_I) + b(T - T_C) \quad (4.13)$$

where a and b are positive constants. This relationship indicates that the frequency of the soft mode phonon should exhibit a kink at the Curie Temperature, which has been observed by Stuhr et al.. The constant C' can be renormalized in a similar way: according to equations (1) and (2), an effective C'_{eff} can be written as

$$\frac{1}{2}C'_{eff} \varepsilon^2 = \frac{1}{2}C' \varepsilon^2 + \frac{1}{2}k_2 M^2 \varepsilon^2 \quad (4.14)$$

Since C' has been observed to exhibit a linear decrease on cooling to T_I, it is reasonable to assume that C'=p(T-T_I). And, close to the magnetic ordering temperature, the squared magnetization can be approximated by M²=q(T-T_C) (p and q are positive constants in these two expressions). Thus, equation (4.14) can be reduced to:

$$C'_{eff} = p(T - T_I) + q(T - T_C) \quad (4.15)$$

Equation (4.15) qualitatively explains the kink of C' observed at the magnetic ordering temperature in Fig. 3. Detailed discussions about the theoretical model of

Landau theory applied to premartensitic phase transformation can be founded in references [148] and [149].

4.3.4 Magnetic Properties.

In comparison to the information available on all structural transformations, the magnetic properties of NiMnGa in the premartensitic state are much less well known. With more and more manifestations of magnetoelastic coupling effects in NiMnGa, magnetic signatures of precursor phenomena are expected to occur.

The magnetization of $\text{Ni}_{49.0}\text{Mn}_{23.5}\text{Ga}_{27.5}$ specimen was determined as a function of temperature between 5 K and 390 K. An external 100 Oe magnetic field was applied along the cubic [110] direction. As shown in figure 4.10, the temperatures T_C and T_M are well marked by considerable magnetization changes. In addition, a slight increase of the magnetization has been found above 340 K, and upon heating to T_C . This unusual magnetization increase is possibly due to the "lock in" transition at T_I . Recalling the well known facts of phonon stiffening in the commensurate phase below T_I , it is reasonable to assume that the spins are locked in the commensurate, modulated phase. Therefore, they can not respond to a small external field. However, the "lock-in" force is lowered after the material reaches the incommensurate phase on heating so that more and more spins can respond to the applied field. This subtle magnetization change can be only detected in the initial heating curve under an external field smaller than 100 Oe as the "lock-in" force in the commensurate phase is expected to be rather weak.

Figure 4.11 displays a series of temperature dependences of the magnetization curves determined in different external fields. During the measurements, the [001]

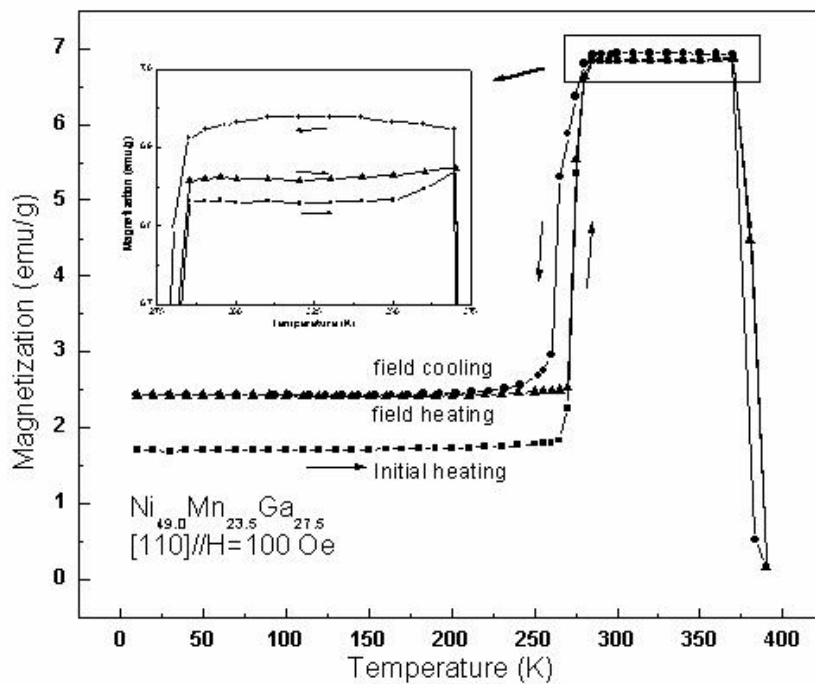


Fig. 4.10 Temperature dependence of magnetization of $\text{Ni}_{49.0}\text{Mn}_{23.5}\text{Ga}_{27.5}$ under 100 Oe magnetic field. The magnetic field is parallel to the crystallographic [110] direction of the cubic $L2_1$ structure. The sample was cooled to 5 K before applying the external field. Subsequently, the initial heating curve was measured in a 100 Oe field and followed by subsequent field-cooling and field-heating.

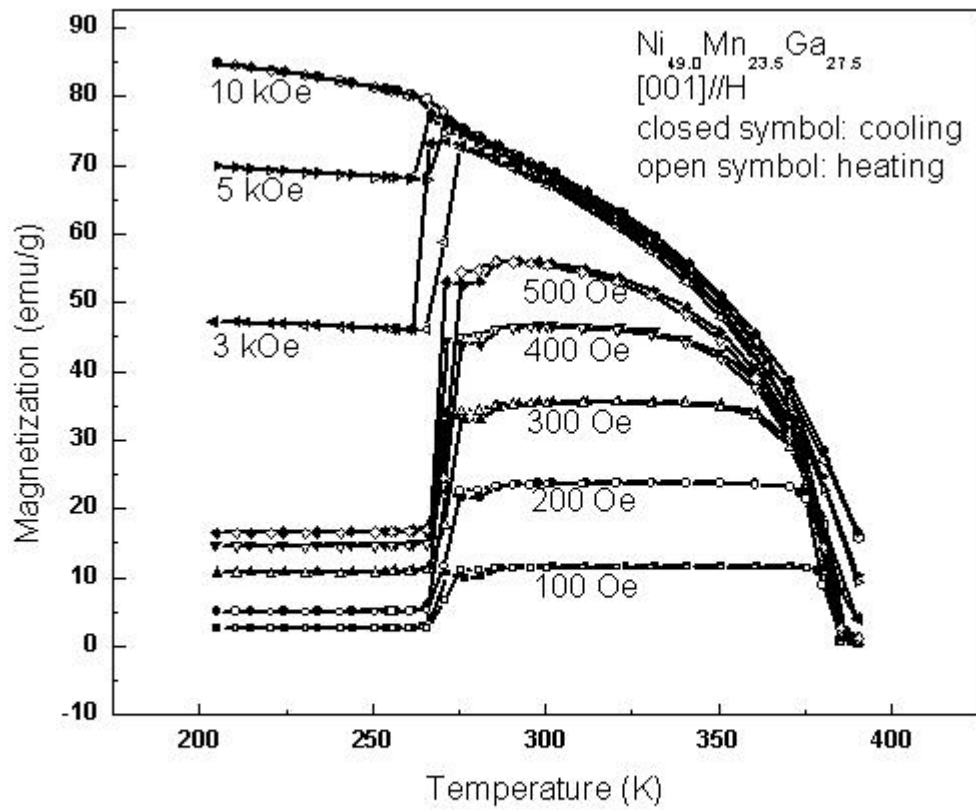


Fig. 4.11 Temperature dependence of the magnetization of $\text{Ni}_{49.0}\text{Mn}_{23.5}\text{Ga}_{27.5}$ under various fields. Magnetic field is parallel to the crystallographic [001] direction of the cubic $L2_1$ structure.

crystallographic direction was oriented parallel to the external field. When the sample was field-cooled and -heated under a magnetic field smaller than 500 Oe, a plateau of the magnetization was found between T_C and T_M . This effect is consistent with the results of temperature independent dc susceptibility measurements, plotted in figure 4.12. Experimentally, the easy direction of magnetization is not known precisely. Webster et al.⁷⁵ proposed that it might be in the $\langle 111 \rangle$ direction of the $L2_1$ cubic phase, however, they also mentioned that the difference of the magnetization curves in different orientations is small. Our measurements show that the [001] direction is the easiest direction of magnetization above T_M (the same as the easy direction in martensite), which will be explicitly demonstrated in the following discussion. This result is in agreement with the published data of Tickle and James in 1999. Figure 4.12 also exhibits a finite dc susceptibility of the premartensite phase in NiMnGa, meaning that a non-negligible field is required to magnetically saturate the specimen along the “easy” direction between T_C and T_M . This is one of the important characteristics of NiMnGa premartensite that distinguishes it from the classical soft magnetic materials.

The magnetization along the different crystallographic directions of [001], [110] and [111] were measured at various temperatures between T_C and T_M . For clarity, only typical magnetization curves at 300 K for fields under 1.2 kOe are displayed in figure 4.13. The results show that the material has a small coercivity and the aforementioned finite dc susceptibility. The magnetization curves along all three crystallographic directions exhibit little hysteresis and resemble each other closely. No traditional easy magnetization behavior can be observed along any

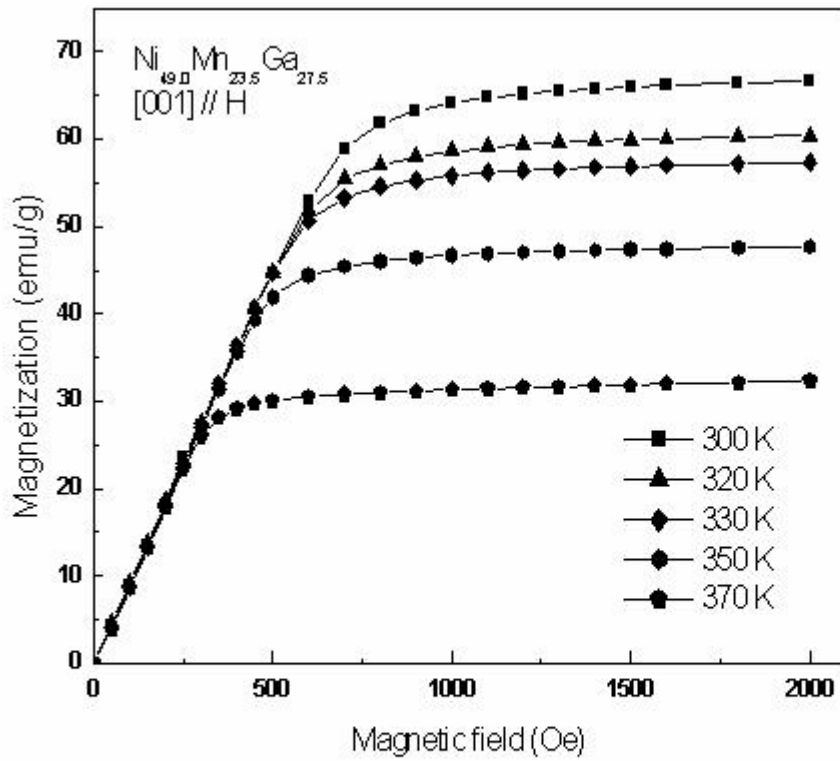


Fig. 4.12 Initial magnetization curves at various temperatures. Magnetic field direction parallel to the cubic [001] direction.

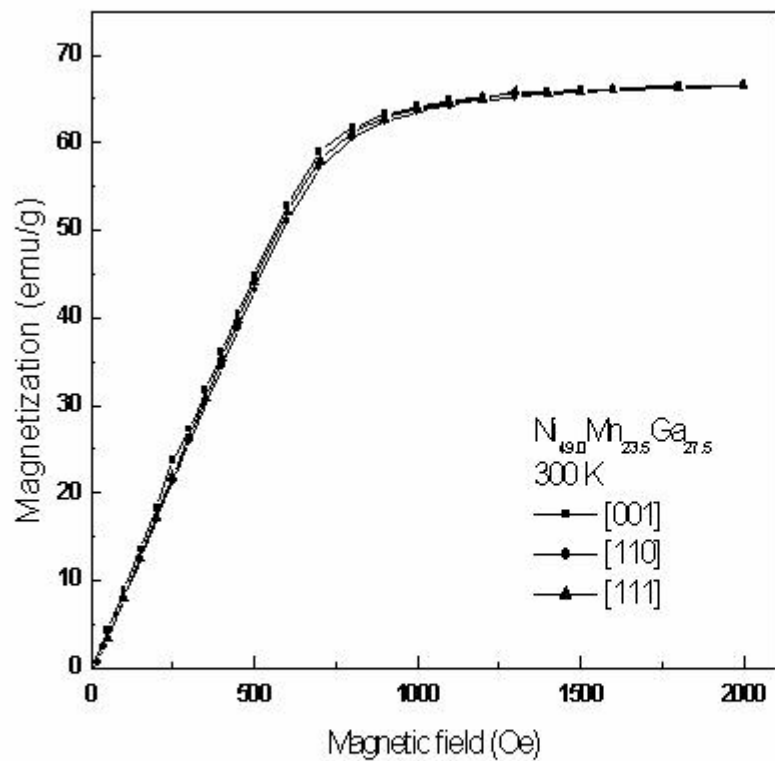


Fig. 4.13 Magnetization curves along [001], [110] and [111] directions in $\text{Ni}_{49.0}\text{Mn}_{23.5}\text{Ga}_{27.5}$ at 300 K.

crystallographic direction of premartensite NiMnGa, although the [001] direction appears to be softer than the other directions. By calculating the difference of the energy $\int HdM$ of the [001], [110] and [111] magnetization curves at all the measuring temperatures, the temperature dependence of the magnetic anisotropy constants K_1 and K_2 in cubic NiMnGa are obtained and plotted in figure 4.14. The result indicates that the premartensite NiMnGa has a very low magnetic anisotropy, $K_1 \approx 10^3 \text{ J/m}^3$ or less, comparable to that of the magnetically softest amorphous materials.¹⁶⁸ The coexistence of finite magnetic dc susceptibility and vanishing magnetic anisotropy is the signature of a magnetically compensated zero anisotropy state in FSMA NiMnGa alloys. Similar magnetic characteristics were reported for bcc magnetostrictive FeGa¹⁶⁹ and fcc FePd¹⁷⁰.

When analyzing the magnetic anisotropy of FeGa alloys containing defect clusters of $\langle 100 \rangle$ Ga-Ga pairs¹⁷¹ it was realized that the competition between the coherent crystalline anisotropy, K_1 , and the anisotropy created by the local uniaxial $\langle 001 \rangle$ pair anisotropies causes an eventual collapse of the magnetic anisotropy. In α -FeGa, $\langle 001 \rangle$ Ga-Ga pairs represent the smallest coherent defect that can introduce a local anisotropy field. In NiMnGa, the formation of defects associated with the premartensitic transformation has been confirmed through the diffuse peak of neutron scattering and ultrasonic attenuation.¹⁷² The local inhomogeneities, including local distorted regions and compositional fluctuations, couple to the soft modes to induce incommensurate nano-clusters (tweed). These clusters produce a locally strong strain field which is consistent with our observation of the significant peak broadening in the neutron diffraction data. Analysis of the random anisotropy model (and

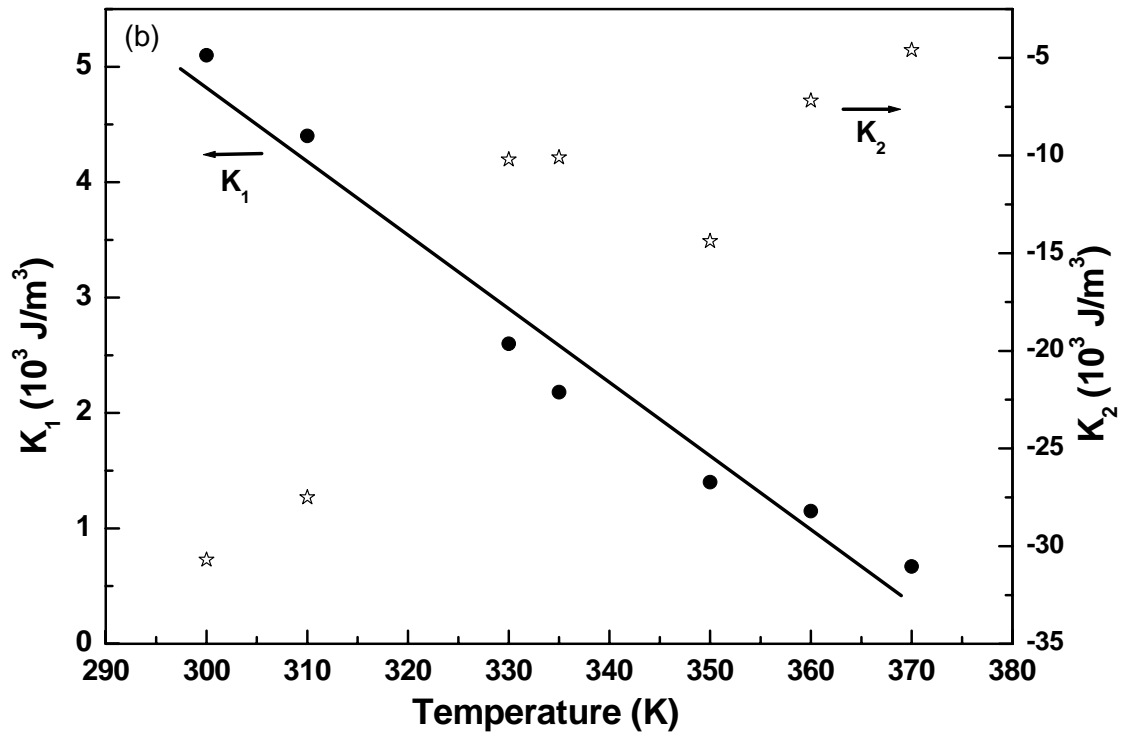


Fig. 4.14 Temperature dependence of magnetic anisotropy constant K_1 and K_2 is bcc solids of $\text{Ni}_{49.0}\text{Mn}_{23.5}\text{Ga}_{27.5}$.

references therein) indicated that random anisotropy does not cancel the coherent cubic anisotropy completely, giving rise to the small magnetic anisotropy, as measured in premartensite NiMnGa. It can thus be seen that NiMnGa premartensite has at least two sources of anisotropy, the first being the coherent anisotropy that arises from the transition element host lattice and the second being the local strong anisotropy due to the "built in" crystal-lattice defects of tweed. At sufficiently large defect concentrations the competition between the coherent and uniaxial anisotropy causes a marked decrease of the macroscopic magnetocrystalline anisotropy as was observed. A demo of the competition has been depicted in Fig. 4.15.

4.4 Conclusion

Neutron powder diffraction data identify the development of a premartensitic phase in $\text{Ni}_{49.0}\text{Mn}_{23.5}\text{Ga}_{27.5}$. Significant peak broadening indicates that a large microstrain is associated with the precursor phenomena. The elastic constants C_{44} and C' display linear behavior with distinct slope changes at the Curie and premartensitic transformation temperatures, supporting the concept of a magnon-phonon coupling enhanced premartensitic transformation. This transition is confirmed to be a weakly first order transition supported by a discontinuity of the elastic modulus C' . The formation of the modulated commensurate phase is confirmed by the stiffening of C_{44} below T_1 . A newly identified magnetically compensated premartensitic state manifests itself through a finite magnetic susceptibility and a vanishing magnetic anisotropy. This behavior is attributed to the competition of a local defect induced anisotropy and the exchange forces in the ferromagnetic NiMnGa system.

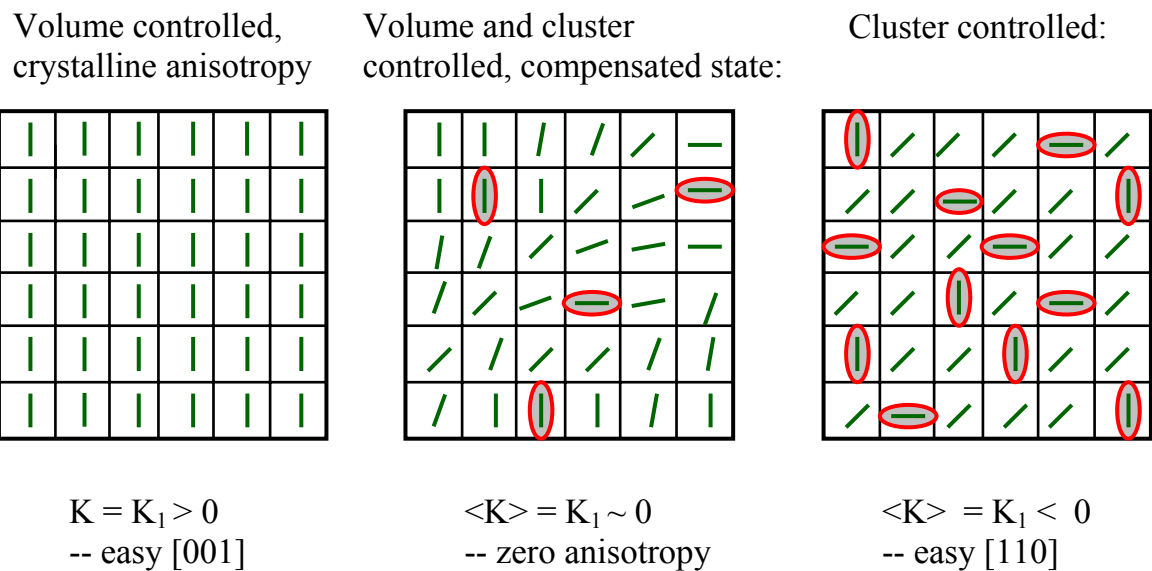


Fig. 4.15 Model of compensated zero magnetic anisotropy. Left: coherent anisotropy arising from the transition element host lattice; Right: the local strong anisotropy due to the "built in" crystal-lattice defects; Center: zero-anisotropy of compensated state due to the competition of the above two.

Chapter 5

Conclusions

This research constitutes an attempt to investigate the role of magnetism in structural transformations in NiMnGa FSMA. We have conducted such a study to investigate magnetoelastic coupling associated with both the MT and premartensitic phase transformation in a nonstoichiometric NiMnGa single crystal.

For the study of magnetic-field induced martensitic variants redistribution:

1. The profile of the magnetization curves is found to be temperature dependent. Close to T_M , the M-H curves display large hysteresis in the first quadrant, an indication of field-induced twin boundary motion giving rise to super magnetoelastic strain for potential application. On the other hand, M-H curves below 250 K show little hysteresis, but multiple slope changes, suggesting twin variant reorientation is inhibited.
2. The SPD technique has been demonstrated as an appropriate method to estimate the magnetic anisotropy in multi-variant NiMnGa martensite below RT. Magnetic anisotropy constant K_1 is found to be increasing on cooling below T_M , and follows a magnetization power law $K_1(T)/K_1(0)=(M_s(T)/M_s(0))^3$.
3. A very restricted temperature window for magnetic actuation has been detected for this alloy, due to the fact that the mobility of the twin boundary decreases much faster than the increase of the magnetic driving force upon cooling.

For the study of magnetoelastic coupling enhanced premartensitic phase transformation:

1. Neutron powder diffraction confirms the premartensitic phase transformation in the crystal. The calculated crystallite size corresponds to the coherent length of the tweed and a large microstrain has been identified prior to the MT.
2. An up-turn of C_{44} in absence of magnetic field at T_I demonstrates the existence of commensurate phase between T_M and T_I . The corresponding magnetoelastic strain has been isolated, and the magnetoelastic condensation undoubtedly states that the premartensitic phase transformation at T_I is a (weakly) first order transformation. Furthermore, the possible convergence of C_{44} at T_M in a magnetically saturated state and a demagnetized state is worth attention as the underlying physics of the magnetoelastic coupling at T_M has not been fully understood.
3. Linear softening of C' indicates the lattice instability of the cubic structure of NiMnGa on cooling to T_M . Slope change of C' at T_C was observed for the first time, providing strong evidence that the character of the premartensitic phase transformation has been altered by the magnetoelastic coupling in NiMnGa FSMAs. The hysteresis of both the slope change of C' and internal friction peaks at T_C suggests the transformation is not simply a magnetic transition, but an elastic transition as well. Hence, it is another weakly first order transition, marking the boundary between the incommensurate phase (tweed) and the commensurate premartensitic phase.

4. Magnetic anomaly of the coexistence of finite dc susceptibility and vanishing magnetic anisotropy prior to the MT was first reported. This newly discovered magnetically compensated premartensitic state is attributed to the competition between the exchange forces of the host lattice and the strong local crystal fields introduced by the tweed.
5. The austenitic phase of the ferromagnetic shape memory alloys, such as $\text{Ni}_{50.4}\text{Mn}_{25.8}\text{Ga}_{23.8}$ and Fe_3Pd , possesses unexpected low magnetocrystalline anisotropy, comparable to or smaller than that of Metglas. This work prompts both the experimental and theoretical study of a new class of magnetoelastic materials, such as FeGa, FeCo and FeAl, which show similar low magnetic anisotropies at certain compositions. These materials exhibit large magnetoelastic strain due to the formation of nano-clusters prior to the martensitic phase transformation.

Bibliography

- ¹ C. S. Smith, in *Martensite*, eds. G. B. Olson and W. S. Owen, (Materials Information Society, 1992) p.21.
- ² P. M. Kelly and L. R. F. Rose, *Progress in Materials Science*, **47** (2002) 463.
- ³ H. Tsubakino, M. Hamamoto and R. Nozato, *Journal of Materials Science Letters*, **8** (1989) 295.
- ⁴ E. Hornbogen, *Advanced Engineering Materials*, **8** (2006)101.
- ⁵ Y. Liu, K. Gall, M. L. Dunn and P. McCluskey, *Smart Materials and Structures*, **12** (2003) 947.
- ⁶ I. Dutta, B. S. Majumdar, D. Pan, W. S. Horton, W. Wright and Z. X. Wang, *Journal of Electronic Materials*, **33** (2004) 258.
- ⁷ M. Bendahan, K. Aguir, J. –L. Seguin and H. Carchano, *Sensors and Actuators A*, **74** (1999) 242.
- ⁸ B. Winzek, S. Schmitz, H. Rumpf, T. Sterzl, R. Hassdorf, S. Thienhaus, J. Feydt, M. Moske and E. Quandt, *Materials Science & Engineering A*, **378** (2004) 40.
- ⁹ M. R. Alam, A. Kumar, N. Shu, H. L. Chan and Q. You, *Applied Surface Science*, **109-110** (1997) 278.
- ¹⁰ D. A. Porter, and K. E. Easterling, *Phase Transformations in metals and alloys*, (Van Nostrand Reinhold Co. Ltd, New York, 1981).
- ¹¹ G. B. Olson, in *Martensite*, eds. G. B. Olson and W. S. Owen, (Materials Information Society, 1992) p.2.
- ¹² G. B. Olson, in *Martensite*, eds. G. B. Olson and W. S. Owen, (Materials Information Society, 1992) p.1.

-
- ¹³ M. Cohen, *Phase Transformations*, (Wiley, New York, 1951) p.588.
- ¹⁴ G. B. Olson and A. L. Roitburd, in *Martensite*, eds. G. B. Olson and W. S. Owen, (Materials Information Society, 1992) p.149.
- ¹⁵ D. P. Koistinen and R. E. Marburger, *Acta Metall.*, **7** (1959) 59.
- ¹⁶ L. Kaufman and M. Cohen, *Trans. AIME*, **206** (1956) 1393. *Prog. Metals Phys.*, **7** (1958) 165.
- ¹⁷ C. M. Wayman, *Physical Metallurgy*, eds. R. W. Cahn and P. Hassen, (North-Holland Physics Publishing, 1983).
- ¹⁸ E. C. Bain, *Trans. AIME*, **70**, (1924) 25.
- ¹⁹ B. A. Bilby and J. W. Christian, *Inst. F Metals Monograph*, **18** (1955) 121.
- ²⁰ W. C. Leslie, *The physical Metallurgy of Steels*, (McGraw-Hill, New York 1981), p. 71.
- ²¹ L. C. Chang and T. A. Read, *Trans. AIME*, **189** (1951) 47.
- ²² M. W. Buehler, J. W. Gilfrich and R. C. Wiley, *J. Appl. Phys.*, **34** (1963) 1475.
- ²³ C. M. Wayman and J. D. Harrison, *J. Metals*, (Sept., 1989) 26.
- ²⁴ K. Otsuka and C. M. Wayman, in *Shape Memory Materials*, eds. K. Otsuka and C. M. Wayman, (Cambridge University Press, 1998) p.36.
- ²⁵ Kurdjumov, G. V. & Khandros, L. G. *Dokl. Akad. Nauk. SSSR*, **66** (1949) 211.
- ²⁶ K. Otsuka, *Functional Metallic Materials*, eds M. Doyama and R. Yamamoto (University of Tokyo Press, 1985) p.56.
- ²⁷ T. Fukuda, T. Saburi, K. Doi and S. Nenno, *Mater. Trans. JIM*, **33** (1992) 271.
- ²⁸ J. Perkins (Ed.), *Shape Memory Effects in alloys*, (Plenum Press, 1978).

-
- ²⁹ L. S. Castleman, S. M. Motzkin, F. P. Alicandri and V. L. Bonawit, *J. Biomed. Mater. Res.*, **10** (1976) 695.
- ³⁰ H. C. Ling and R. Kaplow, *Metall. Trans.*, **11A** (1980) 77.
- ³¹ H. C. Ling and R. Kaplow, *Metall. Trans.*, **12A** (1981) 2101.
- ³² H. C. Ling and R. Kaplow, *Mater. Sci. Eng.*, **51** (1981) 193.
- ³³ S. Miyazaki and K. Otsuka, *Metall. Trans.*, **17A** (1986) 53.
- ³⁴ J. Van Humbeeck and R. Stalmans, in *Shape Memory Materials*, eds. K. Otsuka and C. M. Wayman, (Cambridge University Press, 1998) p.165.
- ³⁵ R. C. O'Handley, *Modern magnetic materials: Principles and applications*, (Wiley, New York, 2000), p. 218.
- ³⁶ R. D. James and M. Wuttig, *Philos. Mag. A*, **77** (1998) 1273.
- ³⁷ T. Maki, K. Kobayashi, M. Minato, and T. Tamura, *Scr. Mater.*, **18** (1984) 1105.
- ³⁸ T. Kakeshita and T. Fukuda, *Journal of Physics: Condensed Matter*, **16** (2004) S5616.
- ³⁹ Y. Furuya, N. W. Hagood, S. Tamoto, T. Kubota and T. Okazaki, *J. of the Japan Institute of Metals*, **66** (2002) 28.
- ⁴⁰ H. C. Lin and K. M. Lin, *Scripta Materialia*, **34** (1996) 1537.
- ⁴¹ H. Matsumoto, *Netsu Sokutei*, **28**, (2001) 2.
- ⁴² S. M. Shapiro, B. X. Yang, Y. Noda, L. E. Tanner, and D. Schryvers, *Phys. Rev. B*, **44** (1991) 9301.
- ⁴³ D. J. Gunton, and G. A. Sanders, *Solid State Commun.*, **14** (1974) 865.
- ⁴⁴ X. Ren, K. Taniwaki, K. Otsuka, T. Suzuki, K. Tanaka, Y. I. Chumlyakov and T. Ueki, *Philos. Mag. A*, **79** (1999) 31.

-
- ⁴⁵ G. Hausch, *J. Phys. Soc. Jpn.*, **37** (1974) 819; **37** (1974) 824.
- ⁴⁶ S. Muto, R. Oshima and F. E. Fujita, *Acta Metall. Mater.*, **38** (1990) 685.
- ⁴⁷ R. E. Peierls, *Quantum Theory of Solids*, (Oxford University Press, Oxford, 1995) p.1074.
- ⁴⁸ R. Comes, M. Lambert, H. Launois and H. R. Zeller, *Phys. Rev. B*, **8** (1973) 571.
- ⁴⁹ R. Comes, M Lambert and H. R. Zeller, *Phys. Stat. Sol. b*, **58** (1973) 587.
- ⁵⁰ S. K. Chan and V. Heine, *J. Phys.*, **F3** (1973) 795.
- ⁵¹ C. Kittel, *Introduction to Solid State Physics*, (Six ed., John Wiley & Sons, 1986) p.285.
- ⁵² G. R. Barsch, J. A. Krumhansl, L. E. Tanner and M. Wuttig, *Scripta Metall.*, **21** (1987) 1257.
- ⁵³ R. Cech and D. Turnbull, *Trans. AIME*, **206** (1956) 206.
- ⁵⁴ Y. Kachi, Y. Bando and S. Higuchi, *J. Appl. Phys.*, **1** (1962) 307.
- ⁵⁵ M. Cohen, E. S. Machlin and V. G. Paranjpe, *Trans. AIME*, **194** (1952) 489.
- ⁵⁶ C. Zener, *Elasticity and Anelasticity of Metals*, (University of Chicago Press, 1948) p37.
- ⁵⁷ E. Pytte, *Phys. Rev. Letters*, **25** (1970) 1176.
- ⁵⁸ B. N. N. Achar and G. R. Barsch, *Phys. Rev.*, **23** (1981) 5840.
- ⁵⁹ G. Guenin, D. Rios Jara, Y. Murakami, L. Delaey and P. F. Gobin, *Scripta Metall.*, **13** (1979) 289.
- ⁶⁰ S. M. Shapiro, B. X. Yaug, Y. Noda, L. E. Tanner, and D. Schryvers, *Phys. Rev. Letters*, **B44** (1991) 9301.
- ⁶¹ W. Cochran, *Adv. Phys.*, **9** (1960) 387.

-
- ⁶² P. W. Anderson, *Fizika Dielektrikov*, ed. G. I. Skanavi. (Acad. Nuak. SSR, Moscow, 1969) p290.
- ⁶³ M. Liu, T. R. Finlayson and T. F. Smith, *Phys. Rev. B*, **48** (1993) 3009.
- ⁶⁴ A. Migliori, W. Visscher, S. Wong, S. E. Brown, I. Tanaka, H. Kojima and P. B. Allen, *Phys. Rev. Lett.*, **64** (1990) 2458.
- ⁶⁵ T. R. Finlayson, *Met. Trans.*, **19A** (1988) 185.
- ⁶⁶ W-K. Lee, M. Lew and A. S. Nowick, *Phys. Rev. B*, **41** (1990) 149.
- ⁶⁷ M. Wuttig, C. Y. Lei, and T. Suzuki, *Met. Trans.*, **19A** (1988) 789.
- ⁶⁸ T. Koayashi, T. Fukase, N. Toyota and Y. Muto, in *Superconductivity in d- and f-Band Metals*, eds. W. Buckel and W. Weber, (Kernforschungszentrum Karlsruhe GmbH, Karlsruhe, 1982) p.59.
- ⁶⁹ C. M. Hwang, M. Meichle, M. B. Salamon and C. M. Wayman, *J. de Phys. Colloq.*, **43** (1982) 231.
- ⁷⁰ A. Nagasawa, T. Makita, N. Nakanishi, M. Iiumi and Y. Morii, *Met. Trans.*, **19A** (1988) 793.
- ⁷¹ K. Fuchizaki and Y. Yamada, *Phys. Rev. B*, **40** (1989) 4720. M. B. Salamon, M. E. Meichle and C. M. Wayman, *Phys. Rev. B*, **31** (1985) 7306.
- ⁷² H. Seto, Y. Noda and Y. Yamada, *J. Phys. Soc. Jap.*, **59**, (1990) 965.
- ⁷³ G. Shirane, *Rev. Mod. Phys.*, **46** (1974) 437.
- ⁷⁴ L. E. Tanner, S. M. Shapiro, D. Schryvers, and Y. Noda, *Mat. Res. Soc. Symp. Proc.*, **246** (1992) 265.
- ⁷⁵ A. Heiming, W. Petry, J. Trampenau, M. Alba, C. Herzig, H. R. Schober and G. Vogl, *Phys. Rev. B*, **43** (1991) 10933, 10948 and 10963.

-
- ⁷⁶ G. L. Zhao and B. N. Harmon, *Phys. Rev. B*, **45** (1992) 2818.
- ⁷⁷ L. E. Tanner, *Phil. Mag.*, **14** (1966) 111.
- ⁷⁸ D. Schryvers and L. E. Tanner, *Ultramicroscopy*, **32** (1990) 241.
- ⁷⁹ S. Muto, S. Takeda, and R. Oshima, *Jap. J. Appl. Phys.*, **29** (1990) 2066.
- ⁸⁰ G. van Tendeloo, M. Chandraselarama, and F. Lovey, *Met. Trans.*, **17A** (1986) 2153.
- ⁸¹ S. Semenovskaya and A. G. Khachatryan, *Phys. Rev. Lett.*, **67** (1991), 2223.
- ⁸² L. -Q. Chen, Y. Wang and A. G. Khachatryan, *Phil. Mag. Lett.*, **65** (1992) 15.
- ⁸³ S. Kartha, J. A. Krumhansl, J. P. Sethna and L. K. Wickham, *Phys. Rev. B*, **52** (1995) 803.
- ⁸⁴ A. G. Khachatryan, S. M. Shapiro, S. Semenovskaya, *Phys. Rev. B*, **43** (1991) 10832.
- ⁸⁵ P.J. Webster, *The magnetic and chemical structures of the Heusler alloys*, PhD thesis, (Sheffield University, 1968).
- ⁸⁶ P.J. Webster, K.R.A. Ziebeck, S.L. Town, and M.S. Peak, *Philos. Mag. B*, **49** (1984) 295.
- ⁸⁷ J. Soltys, *Acta Physica Polonica A*, **47** (1975) 521.
- ⁸⁸ V.V. Kokorin and V.A. Chernenko, *Phys. Met. Metall.*, **68** (1989) 111.
- ⁸⁹ I.K. Zaslavskiy, V.V. Kokorin, V.V. Martynov, A.V. Tkachenko, and V.A. Chernenko, *Phys. Met. Metall.*, **69** (1990) 104.
- ⁹⁰ A.N. Vasil'ev, V.V. Kokorin, Yu.I. Savchenko, and V.A. Chernenko, *Sov. Phys. JETP*, **71** (1991) 803.
- ⁹¹ K. Ullakko, J. K. Huang, C. Kantner, R. C. O'Handley and V. V. Kokorin, *Appl. Phys. Lett.*, **69** (1996) 1966.

-
- ⁹² K. Ullakko, J.K. Huang, V.V. Kokorin, R.C. O'Handley, *Scripta Materialia*, **36** (1997) 1133.
- ⁹³ S.J. Murray, M. Marioni, S.M. Allen, R.C O'Handley, and T.A. Lograsso, *Appl. Phys. Lett.*, **77** (2000) 886.
- ⁹⁴ A. Sozinov, A.A. Likhachev, N. Lanska and K. Ullakko, *Appl. Phys. Lett.*, **80** (2002) 1746.
- ⁹⁵ M. Wuttig, L. Liu, T. Koichi and R. D. James, *J. Appl. Phys.*, **87** (2000) 4707.
- ⁹⁶ A. DeSimone and R. D. James, *J. Mech. Phys. Solids*, **50** (2002) 283.
- ⁹⁷ R. C. O'Handley, *J. Appl. Phys.*, **81** (1998) 3263.
- ⁹⁸ V. A. L'vov E. V. Gomonaj and V. A. Chernenko, *J. Phys.: Condensed Matter.*, **10** (1998) 4587.
- ⁹⁹ V. V. Martynov, and V. V. Kokorin, *J. Phys. III*, **2** (1992) 739.
- ¹⁰⁰ V. V. Martynov, *J. de Physique IV*, **5** (1995) C8-91.
- ¹⁰¹ P. J. Brown, J. Crangle, T. Kanomata, M. Matsumoto, K –U Neumann, B. Ouladdiaf and K. R. A. Ziebeck, *J. Phys.: Condensed Matter.*, **14** (2002) 10159.
- ¹⁰² S. Morito and K. Otsuka, *Materials Science and Engineering A*, **208** (1996) 47.
- ¹⁰³ J. Pons, V. A. Chernenko, R. Santamarta and E. Cesari, *Acta Mater.*, **48** (2000) 3027.
- ¹⁰⁴ A. Sozinov, A. A. Likhachev, and K. Ullakko, *Proc. SPIE*, **4333** (2001) 189.
- ¹⁰⁵ C. Seguí, V. A. Chernenko, J. Pons, E. Cesari, *J. Magn. Magn. Mater.*, **290-291** (2005) 811.
- ¹⁰⁶ V.A. Chernenko, C. Seguí, J. Pons, and V. V. Kokorin, *Phys. Rev. B*, **57** (1998) 2659.

-
- ¹⁰⁷ P. Entel, V. D. Buchelnikov, V. V. Khovailo, A. T. Zayak, W. A. Adeagbo, M. E. Gruner, H. C. Herper and E. F. Wassermann, *J. of Phys. D: Appl. Phys.*, **39** (2006) 1.
- ¹⁰⁸ H. B. Callen and E. Callen, *J. Phys. Chem. Solids*, **66** (1966) 1271.
- ¹⁰⁹ L. Straka, O. Heczko and N Lanska, *IEEE Trans. Magn.*, **38** (2002) 2835.
- ¹¹⁰ L. Straka and O. Heczko, *J. Appl. Phys.*, **93** (2003) 8636.
- ¹¹¹ A. Sozinov, A. A. Likhachev, and K. Ullakko, *IEEE Trans. Magn.*, **38** (2002) 2814.
- ¹¹² A. Ayuela, J. Enkovaara, K. Ullakko and R. M. Nieminen, *J. Phys.: Condens. Matter*, **11** (1999) 2017.
- ¹¹³ J. Enkovaara, A. Ayeula, L. Nordström and R. M. Nieminen, *Phys. Rev. B*, **65** (2002) 134422.
- ¹¹⁴ P. A. Lindgård and O. G. Mouritsen, *Phys. Rev. Lett.*, **57** (1986) 2458.
- ¹¹⁵ J. A. Krumhansl, *Solid State Commun.*, **84** (1992) 251.
- ¹¹⁶ J. A. Krumhansi and R. J. Gooding, *Phys. Rev. B*, **39** (1989) 3047.
- ¹¹⁷ X. Jin, M. Marioni, D. Bono, S. M. Allen, R. C. O’Handley, and T. Y. Hsu, *J. Appl. Phys.*, **91** (2002) 8222.
- ¹¹⁸ N. Lanska, O. Söderberg, A. Sozinov, Y. Ge, K. Ullakko, and V. K. Lindroos, *J. Appl. Phys.*, **95** (2004) 8074.
- ¹¹⁹ L. Manosa, A. González-Comas, E. Obradó and A. Planes, *Materials Science and Engineering*, **A273-275** (1999) 329.
- ¹²⁰ A. González-Comas, E. Obradó, L. Manosa, A. Planes, V. A. Chernenko, B. J. Hattink and A. Labarta, *Phys. Rev. B*, **60** (1999) 7085.

-
- ¹²¹ V. A. Chernenko, J. Pons, C. Seguí and E. Cesari, *Acta Materialia*, **50** (2002) 53.
- ¹²² T. Castán, A. Planes and A. Saxena, *Phys. Rev. B*, **67** (2003) 134113.
- ¹²³ G. H. Lander, *J. Magn. Magn. Mater.*, **29** (1982) 271.
- ¹²⁴ S. M. Shapiro, B. X. Yang, G. Shirane, Y. Noda, and L. E. Tanner, *Phys. Rev. Lett.*, **62** (1989) 1298.
- ¹²⁵ S. M. Shapiro, J. Z. Larese, Y. Noda, S. C. Moss, and L. E. Tanner, *Phys. Rev. Lett.*, **57** (1986) 3199.
- ¹²⁶ S. Muto, S. Takeda, R. Oshima and F. E. Fujita, *Jpn. J. Appl. Phys.*, **27** (1988) L1387.
- ¹²⁷ S. Muto, R. Oshima and F. E. Fujita, *Metall. Trans. A*, **19** (1988) 2723.
- ¹²⁸ T. R. Finlayson, M. Mostoller, W. Reichardt and H. G. Smith, *Solid State Common.*, **53** (1985) 461.
- ¹²⁹ A. Planes and Ll. Mañosa, *Solid State Phys.*, **55** (2001) 159.
- ¹³⁰ A. Planes and Ll. Mañosa, *Mater. Sci. Forum*, **327-328** (2000) 421.
- ¹³¹ D. Schryvers and L. E. Tanner, *Ultramicroscopy*, **37** (1990) 241.
- ¹³² A. Zheludev, S. M. Shapiro, P. Wochner, A. Schwartz, M. Wall, and L. E. Tanner, *Phys. Rev. B*, **51** (1995) 11310.
- ¹³³ V. V. Kokorin, V. A. Chernenko, E. Cesari, J. Pons and C. Seguí, *J. Phys.: Condens. Matter.*, **8** (1996) 6457.
- ¹³⁴ V. V. Kokorin, V. A. Chernenko, J. Pons, C. Seguí and E. Cesari, *Solid State Comm.*, **101** (1997) 7.
- ¹³⁵ L. Mañosa, A. González-Comas, E. Obradó, A. Planes, V. A. Chernenko, V. V. Kokorin, and E. Cesari, *Phys. Rev. B*, **55** (1997) 11068.

-
- ¹³⁶ J. Worgull, E. Petti, and J. Trivisonno, *Phys. Rev. B*, **54** (1996) 15695.
- ¹³⁷ T. E. Stenger and J. Trivisonno, *Phys. Rev. B*, **57** (1998) 2735.
- ¹³⁸ E. Obradó, A. González-Comas, L. Mañosa, A. Planes, *J. Appl. Phys.*, **83** (1998) 7300.
- ¹³⁹ A. González-Comas, E. Obradó, L. Mañosa, A. Planes, V. A. Chernenko, B. Jan Hattink and A. Labarta, *Phys. Rev. B*, **60** (1999) 7085.
- ¹⁴⁰ A. González-Comas, E. Obradó, L. Mañosa, A. Planes, and A. Labarta, *J. Magn. Mater.*, **196-197** (1998) 637.
- ¹⁴¹ E. Obradó, A. González-Comas, L. Mañosa and A. Planes, *J. Appl. Phys.*, **83** (1998) 7300.
- ¹⁴² A. Zheludev, S. M. Shapiro, P. Wochner, and L. E. Tanner, *Phys. Rev. B*, **54** (1996) 15045.
- ¹⁴³ J. A. Reissland, *Physics Phonons*, (New York, London, 1973) p. 368.
- ¹⁴⁴ U. Stuhr, P. Vorderwisch, V. V. Kokorin, and P. -A. Lindgård, *Phys. Rev. B*, **56** (1997) 14360.
- ¹⁴⁵ L. Mañosa, A. Planes, J. Zarestky, T. Lograsso, D. L. Schlagel and C. Stassis, *Phys. Rev. B*, **64** (2001) 024305.
- ¹⁴⁶ E. Cesari, V. A. Chernenko, V. V. Kokorin, J. Pons and C Seguí, *Acta Mater.*, **45** (1997) 999.
- ¹⁴⁷ V. V. Khovilo, T. Takagi, A. D. Bozhko, M. Matsumoto, J. Tani and V. G. Shavrov, *J. Phys.: Condens. Matter.*, **13** (2001) 9655.
- ¹⁴⁸ A. Planes, E. Obradó, A. González-Comas, and L. Mañosa, *Phys. Rev. Lett.*, **79** (1997) 3926.

-
- ¹⁴⁹ T. Castán, E. Vives and P. Lindgård, *Phys. Rev. B*, **60** (1999) 7071.
- ¹⁵⁰ A. E. Clark, J. P. Teter and O. D. McMasters, *J. Appl. Phys.*, **63** (1988) 3910.
- ¹⁵¹ A. E. Clark, D. N. Crowder, *IEEE Trans. Magn.*, **21** (1985) 1945.
- ¹⁵² N. Lanska, O. Söderberg, A. Sozinov, Y. Ge, K. Ullakko, and V. K. Lindroos, *J. Appl. Phys.*, **95** (2004) 8074.
- ¹⁵³ R. Tickle and R. D. James, *J. Magn. Magn. Mater.*, **195** (1999) 627.
- ¹⁵⁴ G. Asti, R. Cabassi, F. Bolzoni, S. Wirth, D Eckert, P. A. P. Wendhausen, and K. H. Muller, *J. Appl. Phys.*, **76** (1994) 6268.
- ¹⁵⁵ C. H. Yu, W. H. Wang, J. L. Chen, G. H. Wu, F. M. Yang, N. Tang, S. R. Qi, W. S. Zhan, Z. Wang, Y. F. Zheng, and L. C. Zhao, *J. Appl. Phys.*, **87** (2000) 6292.
- ¹⁵⁶ M. De Graef, Y. Kishi, Y. Zhu and M. Wuttig, *J. Phy. IV*, **112** (2003) 993.
- ¹⁵⁷ A. A. Likhachev, A. Sozinov, and K. Ullakko, *Materials Science and Engineering A*, **378** (2004) 513.
- ¹⁵⁸ J. Enkovaara, A. Ayuela, L. Nordström and R. M. Nieminen, *J. Appl. Phys.*, **91** (2002) 7798.
- ¹⁵⁹ S. -Y. Chu, A. Cramb, M. De Graef, D. Laughlin, and M. E. Mchenry, *J. Appl. Phys.*, **87** (2000) 5777.
- ¹⁶⁰ H. Zijlstra, *Experimental Methods in Magnetism, Part II* (North-Holland, Amsterdam, 1967), pp.168.
- ¹⁶¹ Oleg Heczko and Ladislav Straka, *J. Appl. Phys.*, **94** (2003) 7139.
- ¹⁶² J. R. Neighbours and G. E. Schacher, *J. Appl. Phys.*, **38** (1967) 5366.
- ¹⁶³ L. Dai, J. Cullen and M. Wuttig, *J. Appl. Phys.*, **95** (2004) 6957.

-
- ¹⁶⁴ M. Wuttig and C. M. Su, *Proc. Symp. On Damping of Multiphase Inorganic Materials*, Ed. by R. B. Bhagat, (AMS, Metals Park, OH, 1993) pp.159.
- ¹⁶⁵ C. M. Su, Y. Wen, and M. Wuttig, *J. de Physique*, **6** (1996) 757.
- ¹⁶⁶ B. D. Cullity, *Elements of x-ray diffraction*, (Upper Saddle River, NJ: Prentice Hall, 2001).
- ¹⁶⁷ R. Jenkins and R. L. Snyder, *Introduction to X-ray powder diffractometry*, (New York: Wiley, 1996).
- ¹⁶⁸ R. Alben, J. J. Becker and M. C. Chi, *J. Appl. Phys.*, **49** (1978) 1653.
- ¹⁶⁹ H. Rumpf, M. Wuttig, and E. Quandt, personal communication.
- ¹⁷⁰ J. Cui, and R. D. James, *IEEE Trans. Magn.*, **37** (2001) 2675.
- ¹⁷¹ J. Cullen, P. Zhao, and M. Wuttig, submitted to *Phys. Rev. Lett.* 2006.
- ¹⁷² J. Worgull, E. Petti, and J. Trivisonno, *Phys. Rev. B*, **54** (1996) 15695.